

# Magnetic adatom structures on semiconductor surfaces in presence of strong electronic correlations

Dissertation zur Erlangung des Doktorgrades  
des Fachbereichs Physik  
der Universität Hamburg

vorgelegt von  
Sergej Schuwalow

Hamburg  
2012

Gutachter der Dissertation: JProf. Dr. F. Lechermann  
Prof. Dr. M. Potthoff

Gutachter der Disputation: JProf. Dr. F. Lechermann  
Prof. Dr. A. Lichtenstein

Datum der Disputation: 17.07.2012

Vorsitzender des Prüfungsausschusses: Dr. A. Chudnovskiy

Vorsitzender des Promotionsausschusses: Prof. Dr. P. Hauschildt

Dekan der Fakultät für Mathematik

Informatik und Naturwissenschaften: Prof. Dr. H. Graener

# Contents

<b>1</b>	<b>Introduction</b>	<b>5</b>
<b>2</b>	<b>Theoretical concepts and tools</b>	<b>7</b>
2.1	Density functional theory (DFT)	7
2.1.1	Exchange-correlation potentials	10
2.2	Interface: Wannier functions	11
2.3	Many-body techniques	13
2.3.1	Rotationally-invariant slave-boson (RISB)	14
2.3.1.1	Additional constraints	17
2.3.2	Dynamical mean-field theory (DMFT)	18
<b>3</b>	<b>Sn adatoms on Si(111) and Ge(111): <math>\alpha</math>-phase surfaces</b>	<b>23</b>
3.1	Introduction	23
3.2	Details of theoretical approach and methods.	26
3.3	Results of DFT calculations.	27
3.3.1	Setup and geometry	27
3.3.2	Single-site unit cells.	28
3.3.2.1	Wannier construction and effective Hamiltonian: single site	32
3.3.3	Three site unit cells	34
3.3.4	Magnetic order.	38
3.4	Electronic correlations: Explicit many-body results	41
3.4.1	LDA+DMFT	42
3.4.2	LDA+RISB	44
3.4.2.1	LDA+RISB: Magnetism	45
3.5	Conclusions and outlook	47
<b>4</b>	<b>Implications of strongly reduced symmetry: Dzyaloshinskii-Moriya interaction in strongly correlated itinerant systems.</b>	<b>53</b>
4.1	Introduction	53
4.2	Hamiltonians and theoretical treatment.	56
4.3	Hubbard bilayer model	59
4.3.1	Half-filled Hubbard bilayer	59
4.3.2	Hole-doped Hubbard bilayer	66
4.4	Two-impurity Anderson model.	68
4.5	Conclusions and outlook	72
<b>5</b>	<b>Adatoms on indium antimonide (110) surface</b>	<b>75</b>

---

5.1	Motivation . . . . .	75
5.2	Setup and geometry . . . . .	76
5.3	Adatom orbitals and bonding behaviour. . . . .	79
5.4	Magnetic anisotropies . . . . .	87
5.5	Vacuum density of states . . . . .	89
5.6	Conclusions and outlook . . . . .	90
<b>6</b>	<b>Summary and conclusions</b>	<b>93</b>
6.1	Deutsche Zusammenfassung . . . . .	95
	<b>Acknowledgements</b>	<b>104</b>

# Chapter 1

## Introduction

Electronic correlation effects in solid state physics are at the root of an incredibly large variety of different physical phenomena. From the conceptually fairly well understood correlation-driven Mott insulators, to the ever-elusive high temperature superconductivity, the most intriguing and nontrivial effects originate from the electron-electron interactions. Phonon-related effects aside, solid-state physics is predominantly electronic behaviour. As such, the effort to gain a proper understanding of the electronic many-body system in a solid has been a driving force of the solid state community for many decades.

As of today, our understanding of solid state physics is one of the major factors governing technological progress. On a large scale, material design guided by theoretical modeling allows fine-tuning of desired properties, creating custom metal alloys [1] and novel glasses [2]. On a smaller scale, understanding and clever use of microscopic material properties enable the further miniaturization of computing devices, with logical elements being built from a setup of a few atoms only [3].

While a large part of our knowledge concerning specific material physics comes from the experiment great progress in the field has been achieved through density functional theory [4, 5]. Pioneered in the middle of the last century, DFT provides a qualitatively accurate understanding of a vast number of different materials. While initially limited to simpler systems, the immense growth of computational power over the last decades allows the treatment of unit cells with thousands of atoms, effectively pushing the limit of structural complexity.

Another boundary not so easily overcome however is the the complexity in the nature of electronic correlations. The electronic behaviour in materials accessible via the DFT mean-field approach is, for the most part, reasonably itinerant and thus the effective correlation strength is not particularly high. To gain access to the more intricate behaviour of strongly correlated systems, explicit many-body methods which go beyond

DFT are required. This is an area intense academic effort has been put into, and much of the work presented here relies heavily on the methods and tools developed in recent years.

The motivation for this work comes from the interest in understanding the interplay between electronic correlations and magnetism in low-symmetry environment, with a particular focus on surface systems. Here, adatom structures on surfaces provide an excellent opportunity to study these intricate physics, with the additional benefit of being easily accessible with various experimental surface probe techniques. Low dimensionality strengthens correlation effects in these adatom structures, while certain geometries, in particular triangular lattice structures or setups with competing nearest neighbour and next-nearest neighbour interactions, invite frustration effects. It is from this complicated, intertwined interactions that the most interesting effects emerge.

The work presented here is subdivided into a rather brief theoretical introduction and three major chapters each dealing with a particular material system or model setup. Apart from gaining insight into their respective physics, which is worthwhile in itself, each contributes a certain aspect to the overarching goal of assessing the role of the individual interactions emerging in low-symmetry (surface) environments.

The first chapter deals with Sn adatom submonolayers on Si(111) and Ge(111) substrates. These systems, being similar in their constituents but different in their physical properties, allow us to learn more about the influence of the hybridization with the substrate, but also magnetic frustration effects and nontrivial orders emerging from them.

The second chapter deals with two model systems, each representing a general low-dimensional setup scenario, namely two-dimensional layered systems and coupled adatom impurities on a surface. The main focus lies on the Dzyaloshinskii-Moriya interaction, a noncollinear interaction between neighbouring spins originating from the spin-orbit coupling in low symmetry environment. Theoretically present in most low-symmetry setups, it is only recently that this topic has gained increased attention in the context of electronic correlations. We will learn that its influence can be far from negligible and responsible for novel and quite nontrivial noncollinear magnetic behaviour.

Lastly, the third chapter deals with magnetic adatoms on InSb(110) surface. In this realistic material system strong magnetic anisotropies due to spin-orbit coupling emerge. All these examples represent different instances of intricate behaviour emerging from a combination of different physical interactions, all within a common background of a surface (or, in case of the models, two-dimensional) geometry. As the our focus wanders towards systems of ever higher complexity, understanding of these and, in turn, their combinations, will become of major importance. It is the hope of the author to have made a contribution here.

## Chapter 2

# Theoretical concepts and tools

The main goal of this work is the theoretical investigation of the behaviour of magnetic adatom structures in low-dimensional systems in presence of strong electronic correlations. As such, a multitude of different important theoretical tools and concepts make an appearance over the course of the discussion. While references to original papers and/or review articles are provided in the text, it is the intention of this introductory chapter to give an overview of the most crucial techniques employed over the course of this work. As the focus of the work lies on realistic structure calculations rather than on the theoretical tools themselves the introduction will be kept on the brief side.

The chapter is structured as follows. The initial part deals with density functional theory (DFT), its basics, features and shortcomings, and establishes its role in our investigation of realistic materials. The second part introduces the interface concept needed for a follow-up explicit many body description of a realistic material system. Finally, the last part of this chapter deals with the two explicit many-body techniques utilized in this work, namely the dynamical mean-field theory (DMFT) and the rotationally-invariant slave boson formalism (RISB), in some more detail.

### 2.1 Density functional theory (DFT)

A realistic material system is governed by intricate interaction between the nuclei forming the lattice of the respective solid and the electrons included therein. Theoretically,

the Hamiltonian

$$\begin{aligned} \hat{H} = & \underbrace{-\frac{\hbar^2}{2m_e} \sum_i \nabla_i^2}_{\hat{T}_e} - \underbrace{\sum_{i,I} \frac{Z_I e^2}{|\mathbf{r}_i - \mathbf{R}_I|}}_{\hat{V}_{ext}} + \underbrace{\frac{1}{2} \sum_{i \neq j} \frac{e^2}{|\mathbf{r}_i - \mathbf{r}_j|}}_{\hat{V}_{int}} \\ & - \sum_I \frac{\hbar^2}{2M_I} \nabla_I^2 + \frac{1}{2} \sum_{I \neq J} \frac{Z_I Z_J e^2}{|\mathbf{R}_I - \mathbf{R}_J|} \end{aligned} \quad (2.1)$$

with electrons denoted by lower case subscripts and nuclei (with charges  $Z_I$  and masses  $M_I$ ) denoted by upper case ones, describes this complex behaviour, including, most importantly, the electron-electron Coulomb interaction. From a practical point of view however, Eq. (2.1) is unyielding to any direct approach for all but the simplest of systems. Even if one acknowledges the fact that due to the comparatively huge mass of the nuclei their response times are much longer than those of the electrons and thus their kinetic energy can be safely neglected if one is not directly interested in effects involving lattice movement, i.e. phonons, we are still left with a system of interacting electrons moving in an external potential provided by the stationary nuclei (which is the Born-Oppenheimer approximation). The problem, even reduced to

$$\hat{H} = \hat{T}_e + \hat{V}_{ext} + \hat{V}_{int} + E_{nuclei} \quad (2.2)$$

in which the positions of the nuclei enter as parameters and their Coulomb interaction gives a mere offset  $E_{nuclei}$ , is one of interacting particles, and thus its hypothetical solutions are many-body wavefunctions  $\Psi_i(\mathbf{r}_1, \mathbf{r}_2, \dots, \mathbf{r}_{N_e})$ . These generally depend on the  $3N_e$  variables, with  $N_e$  being the total number of electrons in the system, which makes the entire problem much too large ( $N_e \sim 10^{23}$  for macroscopic systems) and complicated to handle without introducing any kind of further simplification, which brings us to the topic of DFT.

Density functional theory, in its formulation due to Hohenberg and Kohn (1964) [4], is an exact theory of many-body systems. Its main statements can be summarized as follows:

- For any system of interacting particles in an external potential  $V_{ext}(\mathbf{r})$ , all properties of this system (including the complete many-body wavefunctions for both ground and excited states) are completely determined by the ground state density  $n_0(\mathbf{r})$ .
- There exists an universal functional  $E[n(\mathbf{r})]$  the global minimum of which, for any given  $V_{ext}(\mathbf{r})$ , gives the exact ground state energy of the system. The corresponding density  $n(\mathbf{r})$  is then the exact ground state density  $n_0(\mathbf{r})$  of the system at hand.

Thus, theoretically, the Hamiltonian is completely determined by the ground state density  $n_0(\mathbf{r})$ , which is a function of 3 variables only.

Though the Hohenberg-Kohn theorems by themselves do not provide a way to actually determine the density for a given system *or* the elusive functional  $E[n]$ , they become important in conjunction with the Kohn-Sham ansatz [5] (1965). As the ground state density determines all properties, the authors suggest adopting an auxiliary system of *non-interacting* particles with the same ground state density (which is assumed to exist). The auxiliary Hamiltonian is chosen to be of the form

$$\hat{H}_{aux} = -\frac{1}{2}\nabla^2 + V_{eff}^\sigma(\mathbf{r}), \quad (2.3)$$

with a local (generally spin dependent) potential  $V_{eff}^\sigma(\mathbf{r})$ , and all calculations may be now performed on the auxiliary independent-particle system.

As such, the density of the auxiliary system can be written in terms of single-particle wavefunctions as

$$n(\mathbf{r}) = \sum_{\sigma} \sum_{i=1}^{N^\sigma} f_i^\sigma |\psi_i^\sigma(\mathbf{r})|^2. \quad (2.4)$$

With the single-particle kinetic energy given by

$$T_s = -\frac{1}{2} \sum_{\sigma} \sum_{i=1}^{N^\sigma} \langle \psi_i^\sigma | \nabla^2 | \psi_i^\sigma \rangle \quad (2.5)$$

and the Hartree energy in terms of particle density

$$E_{Hartree}[n] = \frac{1}{2} \int d\mathbf{r} d\mathbf{r}' \frac{n(\mathbf{r})n(\mathbf{r}')}{|\mathbf{r} - \mathbf{r}'|} \quad (2.6)$$

the Hohenberg-Kohn functional for the ground state energy can be written as

$$E_{KS} = T_s[n] + \int d\mathbf{r} V_{ext}(\mathbf{r})n(\mathbf{r}) + E_{Hartree}[n] + E_{xc}[n] + E_{nuclei} \quad (2.7)$$

where all many-body exchange-correlation effects are grouped up into the (for now unknown) functional  $E_{xc}[n]$ .

In this expression, all quantities save for the kinetic energy  $T_s$  of the auxiliary system are now written in terms of the density  $n(\mathbf{r})$ . Varying  $E_{KS}$  with respect to the wavefunctions while enforcing orthonormalization  $\langle \psi_i^\sigma | \psi_j^{\sigma'} \rangle = \delta_{i,j} \delta_{\sigma,\sigma'}$  via Lagrange multipliers  $\varepsilon_i$  finally leads to the Kohn-Sham Schrödinger-like equations

$$(H_{KS}^\sigma - \varepsilon_i^\sigma) \psi_i^\sigma(\mathbf{r}) = 0 \quad (2.8)$$

with

$$H_{KS}^\sigma = -\frac{1}{2}\nabla^2 + V_{KS}^\sigma(\mathbf{r}) \quad (2.9)$$

and

$$\begin{aligned} V_{KS}^\sigma(\mathbf{r}) &= V_{ext}(\mathbf{r}) + \frac{\delta E_{Hartree}}{\delta n(\mathbf{r}, \sigma)} + \frac{\delta E_{xc}}{\delta n(\mathbf{r}, \sigma)} \\ &= V_{ext}(\mathbf{r}) + V_{Hartree}(\mathbf{r}) + V_{xc}(\mathbf{r}) \end{aligned} \quad (2.10)$$

The equations (2.8) have the form of single particle Schrödinger equations with a potential dependent on the resulting density, and can be solved self-consistently. The thus determined ground state density  $n_0(\mathbf{r})$  is then, by construction, the same as the ground state density of the system of interacting particles in an external potential  $V_{ext}(\mathbf{r})$ , with the same ground state energy  $E_0$ .

This is the gist of the density functional theory approach. All calculations are performed on the auxiliary system: with the transition from many-body to single particle wavefunctions the task becomes numerically feasible. In return, only the ground state energy and density are guaranteed to be correct in *exact* Kohn-Sham theory, the eigenvalues and eigenfunctions themselves (and thus all quantities derived from them explicitly) are not.

### 2.1.1 Exchange-correlation potentials

In addition to the issues of the Kohn-Sham approach *itself* mentioned in the previous section there remains the fact that the exchange correlation potential  $E_{xc}[n]$  is not known exactly. As the single-particle kinetic energy and the long-range Hartree terms are treated explicitly,  $E_{xc}[n]$  can be expected to be reasonably local in terms of the density. Thus, practical calculations are performed using educated approximations to  $E_{xc}[n]$ . Surprisingly, even relatively simple approaches lead to satisfying results here. Two most widely utilized approximations for  $E_{xc}[n]$  are the local (spin) density approximation (L(S)DA) and the generalized gradient approximation (GGA). In the LDA approach, the exchange-correlation energy of the system is assumed to be the same as in a homogeneous electron gas with the same density.

$$\begin{aligned} E_{xc}^{LSDA}[n^\uparrow, n^\downarrow] &= \int d\mathbf{r} n(\mathbf{r}) \epsilon_{xc}^{hom}(n^\uparrow(\mathbf{r}), n^\downarrow(\mathbf{r})) \\ &= \int d\mathbf{r} n(\mathbf{r}) [\epsilon_x^{hom}(n^\uparrow(\mathbf{r}), n^\downarrow(\mathbf{r})) + \epsilon_c^{hom}(n^\uparrow(\mathbf{r}), n^\downarrow(\mathbf{r}))] \end{aligned} \quad (2.11)$$

where the exchange energy  $\epsilon_x^{hom}(n(\mathbf{r}))$  has an analytical expression

$$\epsilon_x^\sigma = -\frac{3}{4} \left( \frac{6}{\pi} n^\sigma \right)^{\frac{1}{3}} \quad (2.12)$$

and an accurate parametrization of the correlation energy of the homogeneous electron gas is available thanks to Monte-Carlo calculations by Ceperley and Alder [6]. The GGA approach additionally involves the dependence of the local exchange-correlation energy density  $\epsilon_{xc}$  on the *gradient* of the electron density  $n_0(\mathbf{r})$ :

$$E_{xc}^{GGA}[n^\uparrow, n^\downarrow] = \int d\mathbf{r} n(\mathbf{r}) \epsilon_x^{hom}(n) F_{xc}(n^\uparrow(\mathbf{r}), n^\downarrow(\mathbf{r}), |\nabla n^\uparrow(\mathbf{r})|, |\nabla n^\downarrow(\mathbf{r})|) \quad (2.13)$$

where several different approximations for  $F_{xc}$  exist in literature. It provides an improvement upon LDA in systems with strong spatial variations in  $n_0$ . As such is the case in surface geometries, we will utilize the GGA functional with the parametrization due to Perdew, Burke and Enzerhof [7] (PBE) throughout this work.

Over the years density functional theory, in the above-mentioned approximations, has been found to provide a quantitatively correct description of a vast number of different solid state material systems. Essential problems, however, arise in cases of strong electron localization where the single-particle DFT description no longer suffices. In presence of strong interactions between individual electrons explicit many-body techniques are needed for an adequate treatment of the system. This becomes especially important in the case of materials with partially filled well-localized d- (and f-) shells, such as transition metal oxides (with the poster strongly correlated systems NiO or  $V_2O_3$ ).

## 2.2 Interface: Wannier functions

As such, correct theoretical description of these systems requires explicit treatment of strong electronic correlations. It will however become evident in the later part of this chapter that direct many-body approaches are numerically costly and, in their current form and with the available computational resources, limited to only a few correlated orbitals. Thus, an *ab-initio* description of a strongly correlated material is performed with a DFT calculation as a starting point [8]. From that, a *correlated subspace* involving only a few well-localized orbitals may be isolated and cast onto an effective model which is then subjected to the many-body treatment.

Within this work, this interface between the DFT and the many-body formalisms is performed via maximally-localized Wannier functions [9, 10]. As such a short description of the approach, mainly following the original publications, is presented here, with the practical results featuring prominently in chapter 3.

A Wannier function (WF)  $w_n(\mathbf{r} - \mathbf{R})$  of the (isolated)  $n$ -th band is related to the corresponding Bloch functions  $\psi_{n\mathbf{k}}(\mathbf{r})$  via

$$w_n(\mathbf{r} - \mathbf{R}) = \frac{V}{(2\pi)^3} \int d\mathbf{k} e^{-i\mathbf{k}\mathbf{R}} \psi_{n\mathbf{k}}(\mathbf{r}) \quad (2.14)$$

with the integral running over the first Brillouin zone and the Bloch function defined as  $\psi_{n\mathbf{k}}(\mathbf{r}) = u_{n\mathbf{k}}(\mathbf{r})e^{i\mathbf{k}\mathbf{R}}$  as usual. It provides a means for an adequate description of the electronic problem in terms of more or less well localized orbitals in real space. As there is a freedom of choice for the phase of the Bloch orbitals which does not change the physics of the system,

$$u_{n\mathbf{k}} \rightarrow e^{i\phi_n(\mathbf{k})} u_{n\mathbf{k}} \quad (2.15)$$

there exists a corresponding variety in the resulting Wannier functions.

It can be straightforwardly checked that the transformation Eq. (2.15) does not change (save for a lattice vector  $\mathbf{R}$ ) the center of mass of the respective Wannier function

$$\langle w|\mathbf{r}|w \rangle_n = \left( \frac{V}{(2\pi)^3} \right)^2 \int d\mathbf{r} \int d\mathbf{k} d\mathbf{k}' \psi_{n\mathbf{k}}^*(\mathbf{r}) \mathbf{r} \psi_{n\mathbf{k}'}(\mathbf{r}) \quad (2.16)$$

however, it changes the spread

$$\Omega = \sum_n [\langle r^2 \rangle_n - \langle \mathbf{r} \rangle_n^2], \text{ with} \quad (2.17)$$

$$\langle \mathbf{r} \rangle_n = \langle w|\mathbf{r}|w \rangle_n = i \frac{V}{(2\pi)^3} \int d\mathbf{k} \langle u_{n\mathbf{k}} | \nabla_{\mathbf{k}} u_{n\mathbf{k}} \rangle, \quad (2.18)$$

$$\langle r^2 \rangle_n = \frac{V}{(2\pi)^3} \int d\mathbf{k} |\nabla_{\mathbf{k}} u_{n\mathbf{k}}|^2 \quad (2.19)$$

A maximally localized Wannier function can be thus selected among all the possible ones by minimizing the functional (2.17) with respect to the transformation (2.15).

In the case of a composite set of bands the procedure is analogous. In this case Eq. (2.15) formally corresponds to

$$u_{n\mathbf{k}} \rightarrow \sum_m U_{mn}^{(\mathbf{k})} u_{m\mathbf{k}} \quad (2.20)$$

where  $U^{(\mathbf{k})}$  is a unitary transformation periodic in  $\mathbf{k}$  which acts on the band indices. Eq. (2.17) then has to be minimized with respect to the mixing matrices  $U_{mn}^{(\mathbf{k})}$ .

This technique allows to build an adequate representation of a subset of the original bandstructure in terms of well-defined localized orbitals, foregoing the  $\mathbf{k}$ -space description well suited for itinerant systems in favor of a real-space picture which lends itself to the treatment of localized phenomena. Additionally, the Wannier function construction may be used to disentangle a desired subset of bandstructure from the rest of the states

even in case of overlap, a more sophisticated procedure described in [10]. As such, this approach is especially well suited to tackle the strongly correlated systems mentioned in the previous section.

It must however be kept in mind that the correlated subspace subjected to the Wannier construction to enter the effective model must be carefully chosen as to actually capture the relevant physics of the material at hand and to offer a picture consistent with chemical bonding and symmetry considerations. A more thorough discussion of this is presented in chapter 3.

The brief explanations presented here mostly follow the original publications cited herein, the extremely comprehensive overview of electronic structure methods by Martin [11] and the lecture notes of the LDA+DMFT school in Jülich 2011 [12].

## 2.3 Many-body techniques

As described in the previous section, the explicit treatment of many-body effects happens within the confines of an effective model with a comparatively low number of orbitals. Consider an effective Hubbard-like Hamiltonian on a lattice

$$\begin{aligned} H &= H_{kin} + H_{loc} \\ &= - \sum_{ij\sigma} t_{ij} c_{i\sigma}^\dagger c_{j\sigma} + \frac{1}{2} \sum_{\alpha\beta\gamma\delta} U_{\alpha\beta\gamma\delta} c_{\alpha}^\dagger c_{\beta}^\dagger c_{\delta} c_{\gamma} \end{aligned} \quad (2.21)$$

The kinetic term features the hopping amplitudes  $t_{ij}$  between orbitals situated on sites  $i, j$  (taken as combined site/orbital indices here), and the model itself can be related to a realistic material by their connection to the corresponding single-particle dispersion  $\varepsilon(\mathbf{k})$  via

$$t_{ij} = \frac{1}{N_k} \sum_{\mathbf{k}} \varepsilon(\mathbf{k}) e^{i\mathbf{k}(\mathbf{R}_i - \mathbf{R}_j)} \quad (2.22)$$

In the case of the Wannier orbital construction described above the  $t_{ij}$  also correspond to hoppings between the individual localized orbitals.

The second term is the most general representation of the on-site electron-electron interaction  $U$ , with the combined spin/orbital indices  $(\alpha, \beta, \gamma, \delta)$ , where the diagonal terms would correspond to the common density-density interaction form  $U n_{\uparrow} n_{\downarrow}$ . The Hubbard  $U$  is active on the individual local orbitals, the actual effective interaction thus depending on the form and extent of the orbital in question, and hence on one's choice of effective model. As such, the details of the local orbital (Wannier) construction enter this part of the Hamiltonian as well and have to be kept in mind for proper evaluation of the results.

The kinetic part of the Hamiltonian can be chosen to be purely nonlocal and can be

easily diagonalized by itself by treating it in  $k$ -space. The local part of the Hamiltonian, on the other hand, can by itself be conveniently treated in onsite Fock basis

$$|n\rangle = (c_1^\dagger)^{n_1} \cdots (c_M^\dagger)^{n_M} |vac\rangle \quad (2.23)$$

where  $n_\alpha = 0, 1$  and  $\alpha = 1 \cdots M$  runs over spin and orbital degrees of freedom. The eigenstates of the local Hamiltonian

$$H_{loc}|\Gamma\rangle = E_\Gamma|\Gamma\rangle \quad (2.24)$$

are then readily expressed as atomic multiplets (compare Table 4.1 in chapter 4).

The treatment of the full problem however, taking both the itinerant nature of the lattice and the local particle-particle interactions into account, is a core question of many-body physics and a formidable task not easily tackled. Here we will briefly deal with two possible many-body approaches utilized over the course of this work, with emphasis on the rotationally-invariant slave-boson technique which is used heavily in chapter 3 and exclusively in chapter 4.

### 2.3.1 Rotationally-invariant slave-boson (RISB)

The rotationally invariant slave-boson formalism approaches the many-body problem by introducing a mechanism by which the local Fock states may be connected to the quasiparticle (QP) degrees of freedom living on the lattice. This is achieved by first artificially enlarging the original Hilbert space. Assume an arbitrary state  $|A\rangle$  of the local Hilbert space, here taken to be an eigenstate of the total particle number operator  $n$  and having the total particle number  $N_A$ , which can be written in terms of Fock states as

$$|A\rangle = \sum_n \langle n|A\rangle |n\rangle. \quad (2.25)$$

Next, one introduces auxiliary fermionic operators  $f_\alpha^{(\dagger)}$ , which correspond to quasiparticle degrees of freedom, and bosonic creation/annihilation operators  $\phi_{An}^{(\dagger)}$ , each associated with a pair  $(A, n)$  of atomic multiplet  $|A\rangle$  and QP Fock state

$$|n\rangle_f = (f_1^\dagger)^{n_1} \cdots (f_M^\dagger)^{n_M} |vac\rangle. \quad (2.26)$$

These bosonic operators are theoretically well defined for each possible pair of states  $(A, n)$ . Within our implementation, however, this pairing is restricted to states with the same total particle number  $N_A$ . Thus, for each original state  $|A\rangle$  we arrive at a new

state living in the enlarged Hilbert space, defined as

$$|\underline{A}\rangle = \frac{1}{\sqrt{D_A}} \sum_n \phi_{An}^\dagger |vac\rangle \otimes |n\rangle_f \quad (2.27)$$

where  $D_A = \binom{M}{N_A}$  is introduced for normalization and which thus consists of both fermionic QP and bosonic content. The states of the enlarged Hilbert space and operators defined thereon are denoted by an underline from here onwards.

Naturally, the enlarged Hilbert space contains a large amount of unphysical states. As such, a set of  $(M^2 + 1)$  constraints is applied:

$$\sum_{An} \phi_{An}^\dagger \phi_{An} = 1 \quad (2.28)$$

which ensures that we only take single-boson states into account, and

$$\sum_A \sum_{nn'} \phi_{An'}^\dagger \phi_{An} \langle n | f_\alpha^\dagger f_{\alpha'} | n' \rangle = f_\alpha^\dagger f_{\alpha'}, \forall \alpha \quad (2.29)$$

which makes the QP and bosonic contents match. These constraints are enough to filter out the unphysical states (for a proof see [13]), leaving us with a set of representatives (2.27) of the original physical states, now living in the enlarged Hilbert space.

Within this 'space of representatives' creation and annihilation operators are defined whose actions on the representative states

$$\underline{d}_\alpha^\dagger |\underline{B}\rangle = \sum_A \langle A | d_\alpha^\dagger | B \rangle |\underline{A}\rangle \quad (2.30)$$

mimic the corresponding original behaviour in the physical Hilbert space, namely

$$d_\alpha^\dagger |B\rangle = \sum_A \langle A | d_\alpha^\dagger | B \rangle |A\rangle \quad (2.31)$$

These are shown in [13] to be of the the form

$$\underline{d}_\alpha^\dagger = \sum_{AB} \sum_{nm} \sum_{\gamma\beta} C_{Bm}^{An}(\alpha, \gamma) \phi_{An}^\dagger \phi_{Bm} M_{\gamma\beta} f_\beta^\dagger \quad (2.32)$$

and

$$\underline{d}_\alpha = \sum_{AB} \sum_{nm} \sum_{\gamma\beta} C_{Bm}^{An}(\alpha, \gamma) \phi_{Bm}^\dagger \phi_{An} M_{\beta\gamma} f_\beta \quad (2.33)$$

with

$$C_{Bm}^{An}(\alpha, \beta) = \langle A | d_\alpha^\dagger | B \rangle \langle n | f_\beta^\dagger | m \rangle, \quad (2.34)$$

$$M_{\gamma,\beta} = \langle \gamma | \left[ \frac{1}{2} (\hat{\Delta}^{(p)} \hat{\Delta}^{(h)} + \hat{\Delta}^{(h)} \hat{\Delta}^{(p)})^{-\frac{1}{2}} \right] | \beta \rangle \quad (2.35)$$

and the quasiparticle and quasihole density matrices

$$\hat{\Delta}_{\alpha\beta}^{(p)} = \sum_{Anm} \phi_{An}^\dagger \phi_{Am}^\dagger \langle m | f_\alpha^\dagger f_\beta | n \rangle, \hat{\Delta}_{\alpha\beta}^{(h)} = \sum_{Anm} \phi_{An}^\dagger \phi_{Am}^\dagger \langle m | f_\beta f_\alpha^\dagger | n \rangle \quad (2.36)$$

With the relations (2.32, 2.33), the physical and QP operators are thus shown to be effectively related by a nondiagonal renormalization matrix

$$\underline{d}_\alpha = \hat{R}[\phi]_{\alpha\beta} f_\beta \quad (2.37)$$

With that, faithful representations of the original kinetic and local parts of the Hamilton operator on the representatives of the enlarged Hilbert space may be constructed.  $\underline{H}_{loc}$  can be shown to emerge as a purely bosonic operator

$$\underline{H}_{loc} = \sum_{AB} \langle A | H_{loc} | B \rangle \sum_n \phi_{An}^\dagger \phi_{Bn}, \quad (2.38)$$

while  $\underline{H}_{kin}$  yields

$$\underline{H}_{kin} = \sum_{\mathbf{k}} \sum_{\alpha\alpha'\beta\beta'} \hat{R}_{\alpha\alpha'}^\dagger \varepsilon_{\alpha'\beta'}(\mathbf{k}) R_{\beta'\beta} f_{\mathbf{k}\alpha}^\dagger f_{\mathbf{k}\beta}. \quad (2.39)$$

From this a mean-field theory may be constructed by condensing the bosonic operators into c-numbers  $\langle \phi_{An} \rangle = \varphi_{An}$ , thus omitting all fluctuations. The system is then described by the free-energy functional

$$\begin{aligned} \Omega[\{\varphi_{An}\}, \Lambda, \lambda_0] &= -\frac{1}{\beta} \sum_{\mathbf{k}} \text{tr} \ln[1 + e^{-\beta(\mathbf{R}^\dagger(\varphi)\varepsilon(\mathbf{k})\mathbf{R}(\varphi)+\Lambda)}] - \lambda_0 \\ &+ \sum_{ABnn'} \varphi_{An'}^* \{ \delta_{nn'} \delta_{AB} \lambda_0 + \delta_{nn'} \langle A | H_{loc} | B \rangle \\ &- \delta_{AB} \sum_{\alpha\beta} \Lambda_{\alpha\beta} \langle n | f_\alpha^\dagger f_\beta | n' \rangle \} \varphi_{Bn}, \end{aligned} \quad (2.40)$$

the extremum of which must be found with respect to the condensed bosons  $\varphi_{An}$  and the Lagrange multipliers  $\lambda_0$  (enforcing the constraint (2.28)) and  $\Lambda_{\alpha\beta}$  (enforcing the  $M^2$  constraints (2.29)).

Using the values thus obtained for the bosons and Lagrange multipliers, accessible output quantities are, among others, the expectation values of all and any operators written in second-quantization formalism (evaluated via (2.32), (2.33)), the physical electrons' Greens function

$$\mathbf{G}_d^{-1}(\mathbf{k}, \omega) = \omega(\mathbf{R}\mathbf{R}^\dagger)^{-1} - [\mathbf{R}^\dagger]^{-1} \mathbf{\Lambda} \mathbf{R}^{-1} - \varepsilon(\mathbf{k}) \quad (2.41)$$

the linear part of the self-energy

$$\Sigma_d(\omega) = \omega(1 - [\mathbf{R}\mathbf{R}^\dagger]^{-1}) + [\mathbf{R}^\dagger]^{-1} \mathbf{\Lambda} \mathbf{R}^{-1} - \varepsilon^0 \quad (2.42)$$

and the quasiparticle weights

$$\mathbf{Z} = \mathbf{R}\mathbf{R}^\dagger. \quad (2.43)$$

Phenomenologically, the theory provides a renormalization  $\mathbf{R}[\phi]$  of the original lattice dispersion  $\varepsilon(\mathbf{k})$  via the onsite electron-electron interaction. The contribution of the individual local multiplet states can be assessed via  $\rho_\Gamma = \sum_{\Gamma'} |\phi_{\Gamma\Gamma'}|^2$ , which corresponds to the occupation probability of these states in the correlated regime. Save for the multiplet weights, only the quasiparticle content of the system is accessible directly within the RISB approach, incoherent atomic-like excitations (Hubbard bands) are not included. For this same reason, the RISB technique in its current form may only treat metallic systems.

### 2.3.1.1 Additional constraints

In addition to the constraints (2.28, 2.29) that are essential to the RISB approach, additional constraints may be imposed in the same manner, enforced by additional Lagrange multipliers to enter the free-energy functional (2.40). These may be used to stabilize competing solutions, improve convergence or investigate the behaviour of the system under (physically motivated) restrictions to the values of certain observables. In chapter 4, for example, such an additional constraint is used to fix the occupation of the dispersive band of the impurity model, according to its role as a 'bath' orbital at half-filling in that context.

A general operator comprised of a creator and an annihilator in the space of representatives has the form

$$\underline{d}_\alpha^\dagger \underline{d}_\beta = \sum_{AB} \langle A | d_\alpha^\dagger d_\beta | B \rangle \sum_n \phi_{An}^\dagger \phi_{Bn}. \quad (2.44)$$

Accordingly, the particle number operator of the orbital  $\alpha$  may be written as  $\underline{n}_\alpha = \underline{d}_\alpha^\dagger \underline{d}_\alpha$ . Assume that due to some physically motivated circumstances we are interested in solutions with a definite occupation  $N_\alpha$ . The appropriate constraint enters Eq. (2.40) in addition to the others

$$\Omega[\{\varphi_{An}\}, \Lambda, \lambda_0, \lambda_n] = \dots + \lambda_n \left( \sum_{AB} \langle A | d_\alpha^\dagger d_\alpha | B \rangle \sum_n \phi_{An}^\dagger \phi_{Bn} - N_\alpha \right) + \dots, \quad (2.45)$$

and additional terms emerge in the derivatives with respect to the Lagrange multipliers and slave-bosons which are required for the extremalization of (2.40):

$$\frac{\partial \Omega}{\partial \lambda_n} = \sum_{AB} \langle A | d_\alpha^\dagger d_\alpha | B \rangle \sum_n \phi_{An}^\dagger \phi_{Bn} - N_\alpha \quad (2.46)$$

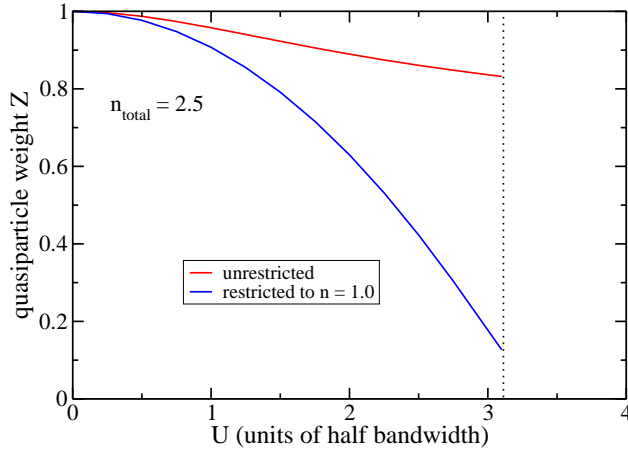


FIGURE 2.1: Hubbard bilayer model at total filling  $n_{total} = 2.5$ , with one of the orbitals restricted to half filling via a constraint in the free-energy functional Eq. (2.40). The model undergoes a Mott transition in that layer at approximately  $U \sim 3.1$  (compare with results in chapter 4).

$$\frac{\partial \Omega}{\partial \phi_{Cm}} = \lambda_n \sum_A \langle A | d_\alpha^\dagger d_\alpha | C \rangle \phi_{Am}^\dagger \quad (2.47)$$

$$\frac{\partial \Omega}{\partial \phi_{Cm}^\dagger} = \lambda_n \sum_B \langle C | d_\alpha^\dagger d_\alpha | B \rangle \phi_{Bm} \quad (2.48)$$

A (somewhat artificial) example of the particle number restriction at work is shown in Fig. 2.1. The subject of the calculation is the Hubbard bilayer model from the first part of chapter 4 (see there for detail), here shown with an interlayer hopping  $t_\perp = 0.1$  and at total filling  $n = 2.5$ , i.e. normally this setup should not be susceptible to a Mott transition. As an additional constraint now enforces a filling of exactly one electron per site on one of the layers, such a transition does indeed take place there with the corresponding quasiparticle weight rapidly decreasing with increasing  $U$ , while the other layer remains perfectly conducting. Of course an introduction of such an external constraint requires a comprehensive physical justification, like for example the interpretation of one of the orbitals as actually belonging to a larger bath with a constant filling (as it is done during the treatment of the two-impurity Anderson model in the latter part of chapter 4), or maybe being part of the surface layer of some substrate in case of the bilayer setup. Careless introduction of ill-justified constraints here will naturally yield unphysical results.

### 2.3.2 Dynamical mean-field theory (DMFT)

While the RISB formalism deals with renormalized quasiparticle degrees of freedom, the DMFT approach attempts to solve the problem of interacting particles on a lattice by

singling out an individual lattice site (or a small cluster), then treating it as embedded into a frequency-dependent bath representing the influence of the surrounding lattice. Eventually, original lattice quantities may be obtained by making the (self-consistent) connection back to the original lattice model. The frequency dependence of the bath allows to include local quantum fluctuations, elevating DMFT beyond a plain mean-field approach (thus *dynamical*). Spatial fluctuations, however, are not included. The connection between the original lattice problem and the *impurity model* is established via the requirement that the local Green's function of the lattice

$$G_{ii}^\sigma(\tau - \tau') = -\langle T c_{i\sigma}(\tau) c_{i\sigma}^\dagger(\tau') \rangle \quad (2.49)$$

has to be equal to the impurity Green's function  $G_{imp}$

$$G_{imp}^\sigma(\tau - \tau') = -\langle T c_\sigma(\tau) c_\sigma^\dagger(\tau') \rangle_{S_{eff}}. \quad (2.50)$$

The corresponding Anderson impurity model has the form

$$\begin{aligned} H_{AIM} = & \underbrace{\sum_{i\sigma} \varepsilon_i a_{i\sigma}^\dagger a_{i\sigma}}_{bath} \\ & + (\varepsilon_0 - \mu) \underbrace{\sum_{\sigma} c_{imp,\sigma}^\dagger c_{imp,\sigma} + U n_\uparrow n_\downarrow}_{impurity} \\ & + \underbrace{\sum_{i\sigma} V_i (a_{i\sigma}^\dagger c_{imp,\sigma} + c_{imp,\sigma}^\dagger a_{i\sigma})}_{coupling} \end{aligned} \quad (2.51)$$

Both the form of the bath and the couplings (i.e. the values of  $\varepsilon_i$  and  $V_i$ ) enter the actual calculations through the hybridization function, which can be written as

$$\Delta(i\omega_n) = \sum_{\alpha} \frac{|V_{\alpha}|^2}{i\omega_n - \varepsilon_{\alpha}} \quad (2.52)$$

which is then inserted into the 'Weiss function'

$$\mathcal{G}_0 = \frac{1}{i\omega_n + \mu - \varepsilon_0 - \Delta(i\omega_n)}. \quad (2.53)$$

With this, the effective action for the impurity may be constructed via

$$\begin{aligned}
S_{eff} = & - \int_0^\beta d\tau \int_0^\beta d\tau' \sum_\sigma c_\sigma^\dagger(\tau) \mathcal{G}_0^{-1}(\tau - \tau') c_\sigma(\tau') \\
& + U \int_0^\beta d\tau n_\uparrow n_\downarrow,
\end{aligned} \tag{2.54}$$

where the Weiss function  $\mathcal{G}_0$  formally plays the role of a bare Green's function now (when in comparison to a standard expression for the action), but effectively includes the dynamical mean-field influence of the environment. The thus constructed effective action incorporates all the dynamics of the local site. It may be used to construct the interacting Green's function of the impurity Eq. (2.50). To connect the impurity quantities with the lattice, the local self energy is extracted from the impurity Green's function and the Weiss function

$$\Sigma_{imp}(i\omega_n) = \mathcal{G}_0^{-1}(i\omega_n) - G_{imp}^{-1}(i\omega_n). \tag{2.55}$$

Stemming from the treatment of the impurity model,  $\Sigma_{imp}(i\omega_n)$  carries the full frequency dependence but is obviously  $\mathbf{k}$ -independent. In contrast to this, the full Green's function of the lattice

$$G(\mathbf{k}, i\omega_n) = \frac{1}{i\omega_n + \mu - \varepsilon_0 - \varepsilon(\mathbf{k}) - \Sigma(\mathbf{k}, i\omega_n)} \tag{2.56}$$

would generally include nonlocal self-energy terms. These are neglected in DMFT, i.e. just the local self-energy calculated from the impurity model is introduced into the lattice (on every lattice site), thus creating the above-mentioned connection.

The actual calculations are performed iteratively. Starting from an initial guess of  $\Sigma(i\omega_n)$  (which may be as simple as a constant), a local Green's function of the lattice model is constructed by summation of Eq.(2.56) over  $\mathbf{k}$ . With  $\Sigma$  and  $G_{loc}$ , the Weiss function may be obtained by using Eq.(2.55). With that, the local effective action (2.54) may be now used to solve the impurity problem, thus obtaining a new  $G_{imp}$  and  $\Sigma(i\omega_n)$  and restarting the cycle until self-consistency is achieved.

The approximation of local self-energy has been shown by Metzner and Vollhardt [14] to become exact in the limit of infinite coordination number/infinite dimensions. Apart from this approximation, the DMFT equations are exact.

In practice, the numerically intensive part of the calculation is the solution of Eq. (2.50) to obtain the impurity Green's function and the impurity self-energy. To this end, a number of highly involved numerical techniques with the sole purpose of evaluating the likes of Eq. (2.50) exist, commonly designated *impurity solvers*. Over the course of this work, the Hirsch-Fye [15] impurity solver was used in all calculations. It should be emphasized that the solvers themselves commonly introduce additional approximations which have to be kept in mind (the HF solver used here introduces an additional time

discretization of the integral (2.50)), with the notable exception of the continuous-time quantum Monte-Carlo approach [16, 17, 18, 19] which is numerically exact (i.e. can be driven to any desired accuracy) and is a recently emergent state-of-the-art technique. Main output quantities are the interacting Green's function  $G$  and the corresponding (local) self-energy  $\Sigma$ , with their values known on a discrete set of Matsubara frequencies  $i\omega$ . Theoretically, one would be most interested in acquiring the one-particle spectral function  $\rho(\omega)$  which is related to the above-mentioned Green's function as

$$\rho(\omega) = -\frac{1}{\pi} \text{Im} G(\omega + i0^+) \quad (2.57)$$

In practice however, the discrete set of values and the statistical error of the data (in case of a QMC solver) makes this transformation an ill-posed mathematical problem. An approximation to  $\rho(\omega)$  may be obtained using the maximum entropy method [20, 21]. The DMFT formalism is used to some extent in the last part of chapter 3. Most of the brief introduction given here is based on the review [22], the AIP conference proceedings [23] and the lecture notes of the LDA+DMFT school in Jülich 2011 [12].

This concludes the brief theory review. As each of the topics presented here is an expansive field of research in itself, this section can only hope to present the most general concepts and convey the main advantages and shortcomings of the individual techniques. More in-depth discussions of the individual subjects can be found in the provided citations.



## Chapter 3

# Sn adatoms on Si(111) and Ge(111): $\alpha$ -phase surfaces

### 3.1 Introduction

Density functional theory [4, 5] is an extremely successful technique which can provide *ab-initio* insight into the electronic structure of the vast majority of solid state systems. It is rather astounding that a mean-field approach which introduces electronic exchange and correlation effects by using a parametrization [6] of the interacting homogeneous electron gas yields, in many cases, results in quantitative agreement with the experiment. It tells us that, for most materials, it is essentially appropriate to view the valence electrons as rather itinerant particles, each one moving in a background potential generated by the entirety of the others.

Thus, if one is interested in explicit effects of electronic correlations one has to specifically look for materials which exhibit strong electron localization. Such circumstances are normally given in systems with partially filled d- and f-orbitals where they may give rise to a plethora of most intriguing physical phenomena, both by themselves (NiO) and especially in combination with additional effects like reduced dimensionality (as, for example, cuprates) or low symmetry environments (see chapter 4).

Adsorbate systems on semiconductor substrates provide an interesting opportunity for the study of correlated physics in (quasi-) twodimensional systems. Normally, a semiconductor surface without termination would undergo reconstruction to minimize energy from the dangling bonds, which by itself can produce quite complicated structures (the Si(111) surface mentioned below, for example, forms a huge surface unit cell with 49 atoms [24]). A (sub)monolayer of adsorbate will prevent such reconstruction and its hybridization with the surface may, depending on both substrate and adsorbate, stabilize

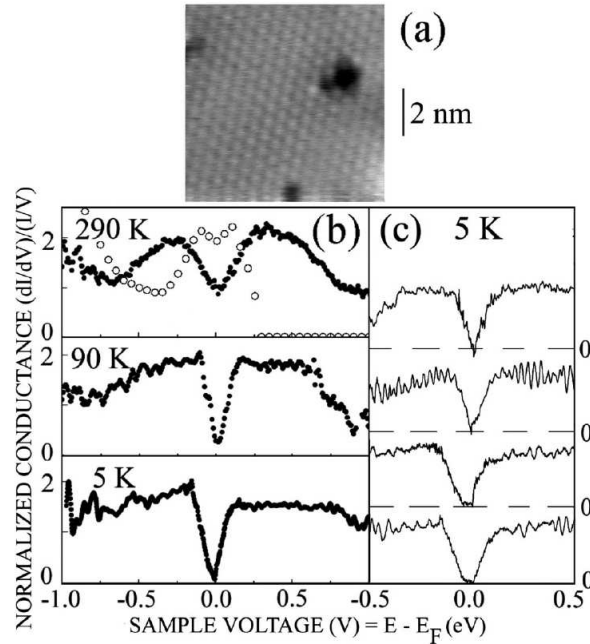


FIGURE 3.1: (a) STM image of Sn/Si(111)- $\sqrt{3} \times \sqrt{3}R30^\circ$  surface at 5 K, (b) average tunneling spectra of the same surface, at different temperatures, (c) single conductance spectra measured at 5 K. Picture taken from Ref. [27].

narrow-band quasi-twodimensional surface states. These surface systems also bring with them the additional benefit of being readily accessible with experimental surface probe techniques, such as STM or electron diffraction methods.

We will now turn to a specific subset of such surface systems, the so called  $\alpha$ -phase surfaces [25]. The general setup consists of a  $1/3$ -monolayer of adsorbate atoms, arranged in a  $\sqrt{3} \times \sqrt{3}R30^\circ$  triangular array on top of a (111) semiconductor surface. Considering the lattice constants of the substrate, the distance between the adsorbate atoms turns out to be fairly large ( $\approx 7\text{\AA}$ ). This configuration thus produces a rather narrow, half-filled surface band which may be, depending on the choice of the system constituents, susceptible to various correlation-driven phenomena. The K/Si(111) setup, for example, is believed to exhibit a Mott-insulating phase at low temperatures [26], whereas in Pb/Ge(111) a transition into a charge-density-wave takes place [25].

Throughout this chapter, we will focus on two special representatives of the  $\alpha$ -surface family which are of particular interest because they exhibit vastly different behaviour despite being structurally and electronically very similar, namely the Sn/Si(111) and Sn/Ge(111) systems. Our aim is to investigate the role of electronic correlations within these two systems, to assess the influence of the different substrates and to determine what part these factors play in the emergence of the various observed phenomena, which will be briefly described in the following.

Both systems have already been subject to considerable attention in the past, both

experimentally and theoretically. The question of a possible appearance of a Mott insulating state in Sn/Si(111) has been investigated experimentally by Modesti *et al* [27]. The system was found to exhibit a metal-insulator transition below 60K, (see Fig. 3.1) a result also corroborated by theory [28]. Additionally, low temperature photoemission experiments [27, 29] suggested an emergent  $3 \times 3$  periodicity due to observed band foldings and two prominent Sn-4d core level photoemission components. However, an investigation of this matter performed by Morikawa *et al* [30] using low temperature STM and reflection high-energy electron diffraction (RHEED) revealed no deviation from the original  $\sqrt{3} \times \sqrt{3}R30^\circ$  structure save from local  $3 \times 3$ -like modulations originating from structural defects. This, in turn, raised the question of magnetic ordering within the insulating regime, i.e. whether the above-mentioned discrepancies might stem from an antiferromagnetic (AFM) Mott-insulating low-temperature state with a magnetic unit cell which is different from the structural one.

Concerning the theoretical results, already standard density functional theory [31, 32] for Sn/Si(111) produces a narrow-band, half-filled surface state with a width of  $\sim 0.3$  eV. Interestingly enough, the band is found to originate primarily from the hybridization of the Sn( $5p_z$ ) states with the Si surface, leading to an effective problem of Coulomb correlations in a 5p system, which in itself is an intriguing deviation from the more common d- and f-orbital based correlated setups. Flores *et al* [31] have derived a minimal Hubbard model for the surface band only from constrained LDA calculations, suggesting an effective value of  $U \sim 1.15$  eV for the system. Their model, however, has not been numerically treated explicitly. Correlation effects at the level of LDA+U have first been included into the description by Profeta and Tosatti [28]. Although the authors obtain a Mott-insulating state already at  $U \sim 2$  eV, they deem the rather large value of 4 eV more realistic since it leads to the expected gap of around 0.3 eV. This choice of U also gives rise to local moments of  $\sim 1\mu_B$  per adatom. The issue of magnetism will reappear during our own treatment of the system later in this chapter.

The Sn/Ge(111) system proves to be equally intriguing. While the overall structural setup seems to be similar to that of Sn/Si(111) at room temperature, the  $\sqrt{3} \times \sqrt{3}R30^\circ$  phase vanishes below 200K in favor of a  $3 \times 3$  configuration [33]. The unit cell now contains 3 non-equivalent Sn adatoms which no longer reside in a single plane. Instead, a vertical distortion of about  $0.3 \text{ \AA}$  in the position of the adatoms produces two different possible ground states for the system. The so-called 1U-2D configuration, with two adatoms moving closer to the surface and one moving further away from it, is energetically slightly favorable (6 meV/adatom) when compared to the competing 2U-1D setup [34]. It has been argued [33] that above 200K the system rapidly fluctuates between these two possible states, giving rise to the observed 'effective'  $\sqrt{3} \times \sqrt{3}R30^\circ$  periodicity. In this case, it would be entirely different from the 'true' periodicity exhibited by Sn/Si(111).

The question of whether or not a Mott-insulating regime for Sn/Ge(111) exists at low temperature has still not been conclusively answered. Cortes *et al* [35] reported the finding of such an insulating regime using STM and low-energy electron diffraction (LEED). This, however, has not been confirmed in experiments done by other groups [36, 37]. Similarly to the Sn/Si(111) case, the surface bands of Sn/Ge(111) are readily reproduced in DFT. A lot of theoretical work has been done concerning the low-temperature  $3 \times 3$  reconstruction [33, 34, 38, 39], an effort which allowed to establish the 1U-2D configuration as the more stable one, as most experimental surface-probe techniques are unable to differentiate between the two possible states. The importance of correlation effects, however, has once again only been investigated at the LDA+U level [28], with overall results similar to those for Sn/Si(111).

### 3.2 Details of theoretical approach and methods.

As we aim to investigate the importance of strong electronic correlations within the systems at hand, our tool of choice is a combination of standard density-functional theory with explicit many-body techniques. The role of DFT is to provide the *ab-initio* components to our approach, the relaxed crystal geometries and band structure data that can then be used as a foothold for the more in-depth investigation of correlated physics. There are two main avenues to achieve this. First is the combination of standard DFT with the dynamical mean-field theory (LDA+DMFT) (see introduction and [40, 41], for the review of DMFT itself see Ref. [22]). This allows us to include explicit many-body effects into the calculation rather than to rely on the single-particle mean-field description provided by DFT. DMFT includes all onsite quantum fluctuations, and is therefore able to describe both quasiparticle and atomic excitations of the system. The DMFT implementation utilized over the course of this work uses a Hirsch-Fye quantum Monte-Carlo impurity solver [15].

The second approach is a combination of DFT with the mean-field slave-boson approach [42, 43, 44] in saddle-point approximation (RISB) [13, 45] (also see introduction). In this, in a way simpler, method, the main emphasis lies on the quasiparticle content of the system (with infinite QP lifetimes). The atomic multiplets are included statically [46, 13, 47]. While the LDA+DMFT approach offers a higher quality of approximation, LDA+RISB is significantly faster (for systems of this size) and provides a means for extended scans of system behaviour with varying parameters.

The main drawback in the use of the various many-body techniques for investigation of realistic materials is that they scale heavily with the size of the problem. All the

above-mentioned combinations with DFT first require construction of an effective problem with a strongly reduced number of orbitals to be feasible. Such an effective model is the final goal of the DFT calculations presented in the following.

To satisfy the requirements of this task, ultimately three different implementations of the DFT approach have been utilized over the course of this work. The first one, and the main source of DFT data presented below, is the highly accurate mixed-basis pseudopotential code (MBPP) [48, 49]. It utilizes norm-conserving pseudopotentials [50] and a highly efficient basis set consisting of both plane waves and atomic-like localized orbitals. This code was used for structure relaxation, band structure calculations and, most importantly, for generating the maximally localized Wannier orbital sets employed in the in-depth many-body calculations. The other two codes are implementations of the projector-augmented-wave method (PAW) [51], namely the CP-PAW and the VASP [52] code. These were mostly used for the investigation of non-collinear magnetism, the results of which are presented on the last part of this chapter, as well as for double-checking the more sensitive DFT results.

The interfacing of DFT with both many-body techniques has been performed using the maximally-localized Wannier function (MLWF) procedure which also has already been briefly described (see theory part). As mentioned in the introduction, this requires a careful choice of the correlated subspace from which to construct the effective model, as well as a proper understanding of the orbital structure of the material at hand. We want to describe the problem in terms of a small number of *localized* electronic orbitals. Naturally, these will, in general, no longer resemble atomic-like orbitals but will rather provide a more 'chemical' point of view, accommodating the effects of the atom in question bonding with its environment. While different choices for the model are theoretically possible, it is still important to choose a perspective which allows for an interpretation rooted in physical and chemical reality of the system. More on this will be explained in the following section.

### 3.3 Results of DFT calculations.

#### 3.3.1 Setup and geometry

The unit cells used to model the two  $\alpha$ -surface systems within DFT are shown in Fig. 3.2. The (111) substrate surface can be best considered as consisting of bilayers stacked on top of each other, as can be clearly seen in the right part of Fig. 3.2, while the geometry of a single bilayer (and surface adatoms) is shown on the left. The surface bilayer theoretically provides for three distinct adsorption sites, namely directly above

the uppermost layer adatoms (top), above the second layer atoms ( $T_4$ ) and above the empty sites ( $H_3$ )(corresponding to a position directly above the fourth layer substrate atom which is not shown). It has been shown by various studies that the Sn adsorbate prefers the  $T_4$  adsorption site, the  $1/3$  monolayer coverage leading to this surface configuration.

Since the DFT implementation requires a periodic geometry, we use a supercell approach, substituting the original system surface for a slab consisting of 3 substrate bilayers, with the z direction in real space being perpendicular to the surface. The cell is chosen to be large enough so that the different slabs are well separated by vacuum regions. As the bottom layer of the slab is, technically, another *unreconstructed* (111) surface, its dangling-bond derived states have to be removed by passivating with hydrogen.

The slab is initially set up with the lattice constant corresponding to the bulk lattice constant of the respective substrate material (5.43 Å for Si, 5.66 Å for Ge). To correctly capture the influence of the surface geometry we then performed structural relaxation with fixed bulk-like positions of the lowest atomic layer, while allowing atomic position shifts throughout the rest of the structure. This results in relaxed Sn-Sn nearest neighbour distances of 6.65 Å and 6.93 Å for the Sn/Si(111) and Sn/Ge(111), respectively.

The unit cell designated with a red border on the left side of Fig. 3.2 is the minimal realistic unit cell that can be constructed in such a way. It incorporates 1 surface Sn adatom, 18 substrate atoms and 3 H atoms used for saturation and corresponds to the  $\sqrt{3} \times \sqrt{3}R30^\circ$  periodicity. The unit cell marked with a green border contains three times as many atoms and is used during the later stages of this work to account for possible inequivalent Sn adatoms.

Throughout this work, k-point meshes with a minimum of 6x6x1 k-points has been used. This corresponds to six irreducible k-points in the Brillouin zone, which has been thoroughly checked to be sufficient for Sn/Si(111). In case of Sn/Ge(111), and for magnetic calculations on both systems, the k-point density had to be considerably increased up to a 25x25x1 setup. In the context of the mixed-basis approach we utilized localized functions for Si (3s, 3p), Ge(3d, 4s, 4p) and Sn (4d, 5s, 5p) orbitals together with a plane wave contribution with an energy cutoff of 16 Ryd. We use the GGA-PBE exchange-correlation functional for all calculations.

### 3.3.2 Single-site unit cells.

We first turn to the calculations performed on the single adatom unit cells for both systems. The density of states data is shown in Fig. 3.3-3.5. Fig. 3.3 shows the local density of states (LDOS) of the Sn adatom as compared to the total density of states of

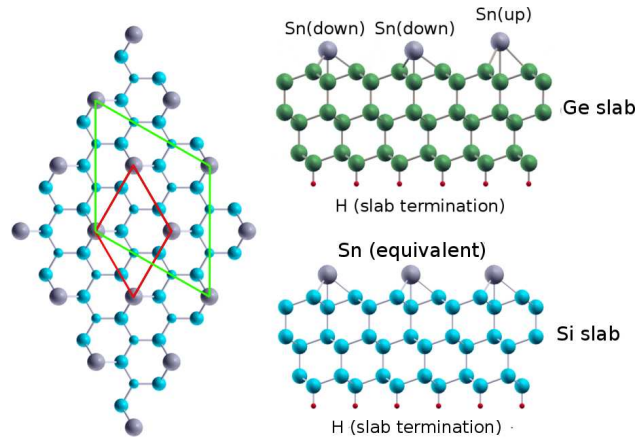


FIGURE 3.2: Left: Top view onto a  $\alpha$ -phase surface. Surface adatoms are shown in grey, first- and second-layer substrate atoms as large and small blue orbs, respectively. Both the  $\sqrt{3} \times \sqrt{3} R30^\circ$  unit cell (red) and the  $3 \times 3$  unit cell (green) are shown. Right: Side view on the slab geometries used in the calculations. The bottom of the slab is passivated by pseudohydrogen to remove the dangling-bond states. The adatoms on the Ge slab show the 1U-2D distortion.

the whole unit cell. The structure around the Fermi level belongs to the surface state originating from the Sn submonolayer, the significant hybridization with the substrate evident from the size of the respective contributions. The width of the surface band is about 0.4 eV, and its overall shape is clearly reminiscent of the simple triangular lattice DOS, dictated by the geometry of the adatom layer. Two subpeaks are clearly visible in both pictures, one extremely close to the Fermi level (more so for the Sn/Si(111) system) and one at the upper edge of the surface state. We can expect the narrow peak near the Fermi level to be of major importance to the magnetic properties of the system, as in accordance to the Stoner criterion, and so the aforementioned need for *very* careful convergence with respect to the number of k-points becomes evident, as already tiny imprecisions in this energy region might have a major influence. Another peculiarity of the Sn/Si(111) system is that the density of states exhibits a clear gap at around -0.3 eV, the surface state-originated DOS feature being disconnected from the lower energy states. This is not so for the Sn/Ge(111), which is a factor to keep in mind for the discussion of structural distortions later in this chapter.

Fig. 3.4 again shows the same density of states, now resolved into contributions from the different atoms within the unit cell. The numbers correspond to the labeling in Fig. 3.8, with factors accounting for multiplicity. The single largest contribution to the surface state stems, as expected, from the Sn adatom, followed by the atoms labeled as (5), (1) and (3), respectively. While atom(s) (1) are next neighbours of the Sn adatom in the first substrate layer and atom (3) is the single next neighbour in the second, the large contribution of (5) is not trivial. Overall, in terms of a localized orbital picture, the Sn-centered surface state extends as far as the next nearest neighbour in the lateral

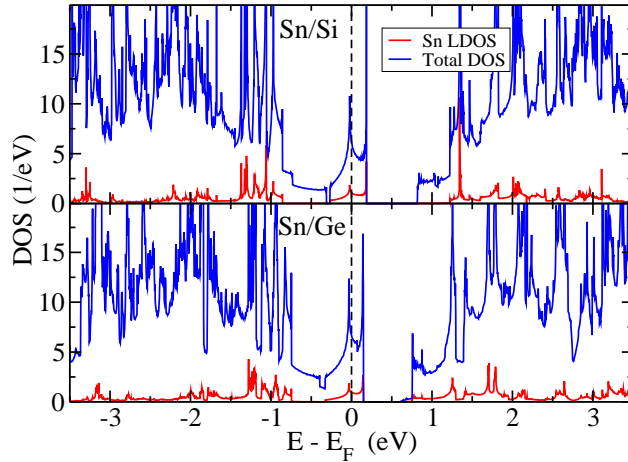


FIGURE 3.3: Total DOS plot and local Sn DOS for the Sn/Si(111) and Sn/Ge(111) systems.

plane and reaches down to the second bilayer into the surface. Contributions from unit cell atoms outside of this reach are negligible.

At last, Fig. 3.5 shows the angular-momentum resolved local Sn DOS for both systems. As can be clearly seen, nearly all of the Sn-related contribution to the states at the Fermi level stems from the the Sn- $5p_z$  local orbital, with a small addition of s-like orbital character. Additionally, there are  $5p_z$ - related unoccupied states at approx. 1.5 eV above the Fermi level for both systems. The other relevant contributions stem from the  $5p_x/5p_y$  orbitals. These produce occupied states at  $\sim -1$  eV as well as unoccupied ones in the region of 1 to 2 eV with respect to the Fermi level, whereby both curves in Fig. 3.5 lie on top of each other by symmetry. There is no contribution from these two states at the Fermi level. As already mentioned, this p-orbital setup is quite unusual and not present in most strongly correlated systems.

The band structure plots for both systems are displayed in Figs. 3.6 and 3.7. In both plots, the top panel shows fatband plots for the Sn- $5p$  orbitals, with contributions of the respective angular momenta to the overall band structure indicated by the width of the underlying colored fatbands. The surface band structure of the system is shown in black, with the half-filled surface state clearly visible at the Fermi level. While in the case of Sn/Si(111) the band is well separated from the rest of the band structure, this is, as could already be seen from the density of states, not strictly the case for Sn/Ge(111) where the band is connected to the states below around the  $\Gamma$  point. In both systems, the dominance of the Sn- $5p_z$  orbital (shown in red) at the Fermi level is evident. The aforementioned contributions of the p-orbitals at both higher and lower energies (with blue denoting  $p_x/p_y$ ) can be seen to form fairly well-defined effective bands, which is important for the construction of the effective models that will be discussed momentarily.

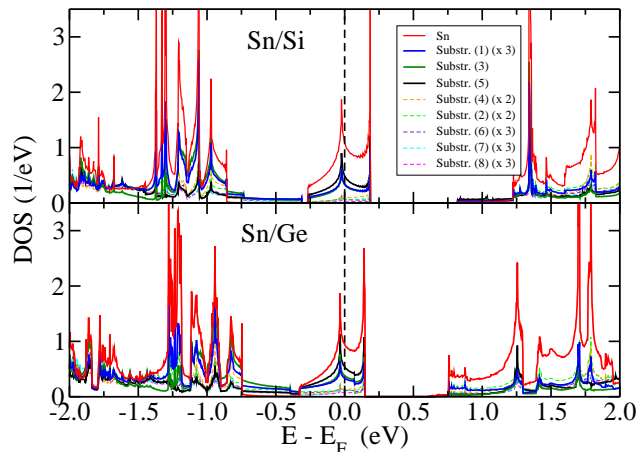


FIGURE 3.4: Local DOS contributions from the different atoms within the unit cell. The dominant contributions around the Fermi level stem from the Sn adatom and substrate atoms (5), (1) and (3). The numbers refer to Fig. 3.8

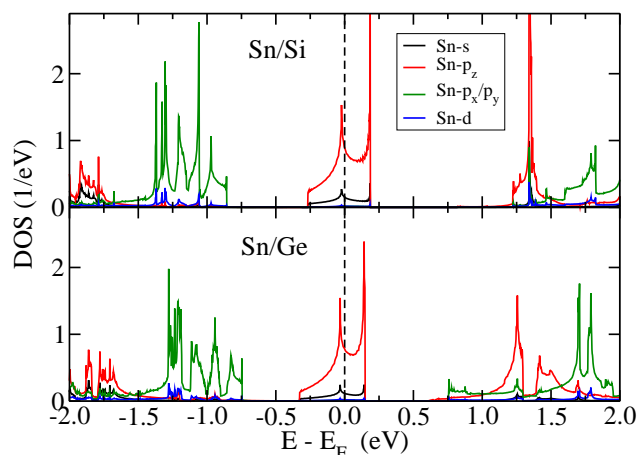


FIGURE 3.5: Angular-momentum resolved contributions to the local Sn DOS. The  $5p_z$ -orbital dominates in the narrow band region around the Fermi level, the  $5p_x$  and  $5p_y$  orbitals mainly contribute at energies around  $-1$  eV and  $1.5$  eV. The two latter curves lay on top of each other.

Additionally, the light brown lines in the background of the top panel show the 3D bulk bandstructures of Si and Ge substrates, respectively. These, by construction, cover all of the *bulk* Brillouin zone and, as such, can be used to identify regions in  $k$ -space which are not accessible in the original solid. It can be clearly seen that the half-filled band in both Sn/Si(111) and Sn/Ge(111) lies within such a region. Thus, this state is energetically separated from the bulk-like states of the substrate which clearly marks it as a product of the surface geometry.

At this point, however, it should be kept in mind that bulk Ge band structure, and particularly the band gap, is a problematic topic in DFT [53, 54]. As can be seen in Fig. 3.7 the Ge 3D band gap becomes extremely small at the  $\Gamma$ -point, a shortcoming of the

approach. As such, additional care has to be exhibited with the interpretation of the system behaviour in this region. However, as long as the surface states are well reproduced, this should not become a hindrance with regard to the construction of effective model Hamiltonians.

### 3.3.2.1 Wannier construction and effective Hamiltonian: single site

Now that some understanding of the systems at hand has been established on the DFT level we would like to assess the effects strong electronic correlations have on the results when taken into account explicitly. As already mentioned in the introduction, an investigation of the full realistic problem is unfeasible with the current many-body methods. Depending on the setup of the system, this may also not at all be required. Since we expect explicit many-body effects to be strong only in regions with high electron localization, it is well justifiable to reserve the many-body treatment to these regions only, while letting the DFT approach deal with the rest of the band structure. Thus, we require an effective Hamiltonian for the description of the *correlated subspace*.

This we construct by the means of maximally localized Wannier functions (MLWF), a method described in the introduction. The effective Wannier bands for both Sn/Si(111) and Sn/Ge(111) are shown in the middle and bottom panels of Figs. 3.6 and 3.7, respectively. The middle panel shows a straightforward approach, with the correlated subspace of the system chosen to be represented by the half-filled surface band only, which corresponds to an effective model with one orbital per site. This is a minimal model, of course, it is however well supported by the physical understanding of the systems we have gained so far, with nearly all of the states at the Fermi level being tied to the reasonably well localized Sn  $5p_z$  orbital.

The localized Wannier function corresponding to the one-band effective construction for the Sn/Si(111) system is shown in Fig. 3.8, with the Sn/Ge(111) function having nearly the same overall appearance. It can be clearly seen that although the dominant contribution to the surface band has been determined to stem from the Sn- $5p_z$  orbital the Wannier function does not have a close resemblance to it. This is the direct consequence of the surface state being not atomic-like in nature, but rather a product of the hybridization with the surface. The three-fold lateral symmetry of the substrate lattice is clearly expressed, with the lobes of the Wannier function reaching towards the direct next in-plane neighbours and the vertical component extending as far down into the substrate as the second bilayer. This results in a spread of  $14.2 \text{ \AA}^2$ . The overall form is clearly consistent with our estimates of the overall extension of the surface state during the investigation of the LDOS contributions in the previous section.

As already mentioned, a single orbital description of the surface state represents a minimal model. Both the angular-momentum resolved local DOS and the band structure plots suggest that, while the  $5p_z$  orbital is clearly dominant, a natural extended choice of the correlated subspace would also take the Sn- $s$ ,  $p_x$  and  $p_y$  into account. The Wannier bands of such an extended 4-band effective model for both systems are shown in the bottom panel of Figs. 3.6 and 3.7. When compared to their respective top panels, it becomes clear that this choice of the Wannier construction setup introduces three additional bands, two below and one above the Fermi energy, which effectively interpolate between the additional band structure contributions shown in the fatband projection. The now four resulting Wannier orbitals are shown in Fig. 3.9. This construction still clearly has the overall three-fold symmetry induced by the substrate structure. Each of the former in-plane lobes, however, is now represented by a separate orbital, with the fourth now more obviously adopting the vertically extended  $p_z$ -like appearance. The three lobes each have a spread of  $13.6 \text{ \AA}^2$ , with a value of  $20.8 \text{ \AA}^2$  for the remaining fourth localized function. The overall appearance of the three separate in-plane orbitals is reminiscent of the chemical  $sp^2$  hybridized orbital picture.

This  $sp^2+p_z$  orbital setup, although appealing from the more intuitive chemical point of view, also has its own disadvantages when compared to the simple one-band model. The filling in this local orbital set amounts to five electrons in four bands, which is one more than the half filled  $sp$ -valence of the carbon group. On one hand, this seems not imminently justifiable, as the constituents of the system (Si, Ge, Sn) do not differ much in their electronegativity. On the other hand however, the orbitals in Fig. 3.9 are not particularly strongly localized on the adatom, showing a non negligible reach into the surface and thus being reasonably able to accommodate additional charge stemming from hybridization with the substrate. Overall, the 4-band model seems very reasonable when handled with care and we have extracted the corresponding hoppings to be used in a future study. As it is a significantly more heavy model, the first single site many-body results in the latter part of this chapter all stem from the one-orbital Wannier Hamiltonian.

Another setup worth considering would be the simpler three-band effective model only consisting of the p-like orbitals. This model has also been investigated and discarded due to its deficiencies. It not only shows an even more unbalanced filling of five electrons in three effective bands, which collides even with the more lenient attempts to interpret the orbitals in semi-local terms, but in addition does not provide the geometry consistent with the facts of the chemical bonding picture.

The hopping integrals for both the 1-band and the 4-band model are listed in Tables 3.1 and 3.2, respectively. In the one-band model, the nearest neighbour hopping amounts to  $|t_{1\text{-band}}| \sim 45 \text{ meV}$  for the Si substrate. In comparison, the hopping amplitude in the Sn/Ge(111) system is somewhat smaller for the nearest neighbours, with a tendency to

larger values for the more distant hoppings.

Figure 3.10 provides a schematic aid for the better understanding of Table 3.2, with the three lobes of the 4-orbital setup marked as numbers 1-3, the  $p_z$ -like orbital given the number 4 and the lattice vectors labeled accordingly (compare with the actual supercell in Fig. 3.2). The numbers correspond to the column/row order in the hopping matrices of Table 3.2. The onsite energies of the four-band model, shown in the (000) entry, display a crystal-field splitting between the three  $sp^2$ - and the  $p_z$ -like orbital, which is on the order of 1.6 eV for the Sn/Si system, with a lower value of  $\sim 0.9$  eV for Sn/Ge. This underlines the stronger adatom-surface hybridization of the Sn/Ge(111) surface already observed during the discussion of the respective bandstructure plots (though the already mentioned difficulties of DFT concerning Ge should still be kept in mind).

This concludes the discussion of single-site DFT results.

### 3.3.3 Three site unit cells

With the discussion of the one-site DFT calculations and the corresponding Wannier models now complete, we go on to treat the 3-site cluster setup. As already mentioned, the triangular cluster configuration is expected to be important for the physics of both systems. The already mentioned 2D-1U structural reconstruction of the adatom monolayer in Sn/Ge(111) cannot be taken into account in a one-site calculation, and also the treatment of magnetic order demands a larger supercell to be able to describe more complicated setups than the most basic ferromagnetic alignment. Thus we turn to the enlarged  $3 \times 3$  supercell construction already briefly shown in Fig. 3.2, marked with a green outline. This cell incorporates a total of 66 atoms, of which 54 are Si (or Ge) substrate atoms, 3 Sn adatoms arranged in a triangular fashion and 9 H atoms for slab termination. For the Sn/Ge(111) system, there is a difference of  $\Delta = 0.32$  Å between the up-down Sn positions [38] which is introduced into the fully structurally relaxed PBE-GGA planar  $3 \times 3$  supercell. For comparison, a planar Sn/Ge(111) and a planar Sn/Si(111) setup have also been constructed.

The Wannier function construction utilized for these larger supercells consists of only one ( $p_z$ ) orbital per adatom. As such, it corresponds to the previously discussed one-band Wannier model, now extended to a three-adatom triangular cluster, and again results in local orbitals similar to the one shown in Fig. 3.8. The bandstructure of the three supercell setups is shown in Fig. 3.11, with the Wannier bands marked in light blue. Again, the Sn/Si(111) surface states (top panel), now represented by the three half-filled bands at the Fermi level, are well separated from the rest of the bandstructure and perfectly reproduced by the Wannier construction, while the planar Sn/Ge(111) (middle

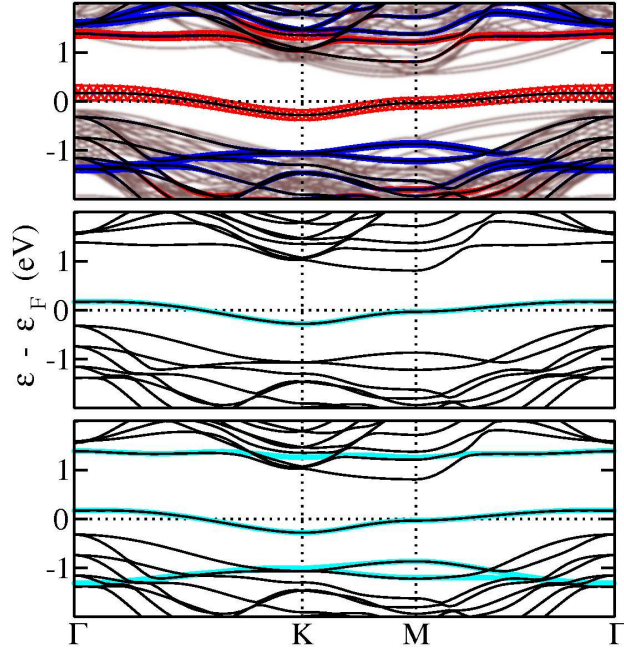


FIGURE 3.6: Band structure plots for the Sn/Si(111)  $\sqrt{3} \times \sqrt{3}R30^\circ$  system. Top: Fatband plot of the Sn- $p_x/p_y$  (blue) and Sn- $p_z$  (red) orbital contributions to the band structure. The 3D bulk Si bandstructure is shown as brown lines in the background for comparison. Middle: Wannier construction for the 1-band model. Bottom: Same for the 4-band model.

direction	100	110	200	210
Sn/Si(111)	44.6 meV	-18.4 meV	6.7 meV	-0.8 meV
Sn/Ge(111)	43.2 meV	-23.7 meV	7.3 meV	-1.8 meV

TABLE 3.1: Hopping integrals up to the fourth-nearest neighbours for the 1-band  $p_z$  model.

panel) effective Wannier bands again display a shift towards lower lying states at the  $\Gamma$  point, which is due to the stronger band hybridization already mentioned during the discussion of the single site unit cell.

While the three-adatom bandstructure of the flat unit cell can be related to that of the single site unit cell via downfolding, the 2D-1U reconstruction in Sn/Ge(111) (shown in the bottom panel) introduces a splitting of the low energy bands, particularly visible in the occupied part of the states. This effect is mirrored by a change in local orbital occupation, shifting from one electron/Wannier orbital to a filling of 1.378 in the (U) orbital and 0.819/0.802 in the two (D) orbitals, respectively. Note that the distortion also makes the two (D) orbitals slightly non-equivalent, an effect which will be more thoroughly elaborated on during the discussion of many-body effects in section 3.4.

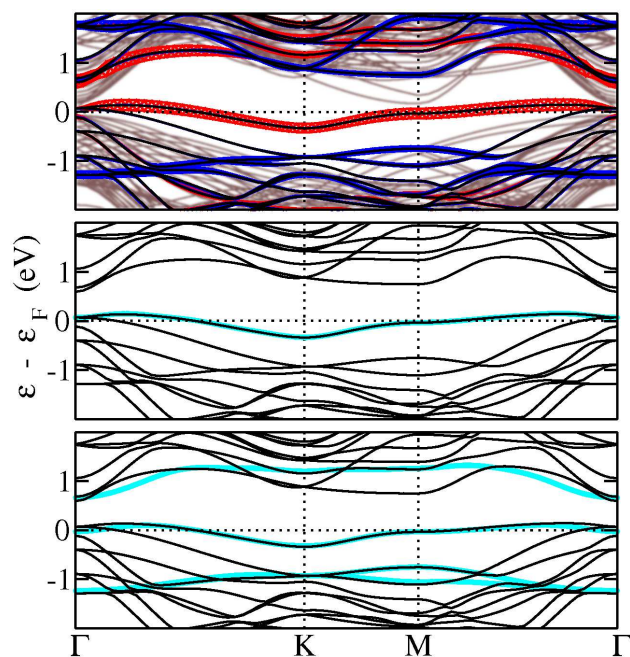


FIGURE 3.7: Same as Fig. 3.6, now for the Sn/Ge(111) system.

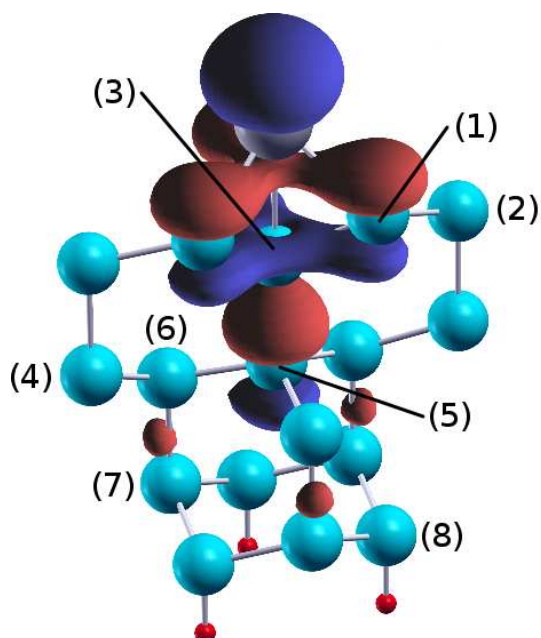


FIGURE 3.8: Wannier orbital of the 1-band model for the Sn/Si(111) system. The numbers refer to the DOS plot shown in Fig. 3.4

Direction	Sn/Si hoppings [meV]				Sn/Ge hoppings [meV]			
	$sp^2(1)$	$sp^2(2)$	$sp^2(3)$	$p_z(4)$	$sp^2(1)$	$sp^2(2)$	$sp^2(3)$	$p_z(4)$
000	-643.8	452.0	452.0	-318.6	-433.1	546.4	546.4	-358.3
	452.0	-643.8	452.0	-318.6	546.4	-433.1	546.4	-358.3
	452.0	452.0	-634.8	-318.6	546.4	546.4	-433.1	-358.3
	-318.6	-318.6	-318.6	990.3	-358.3	-358.3	-358.3	463.2
100	-42.6	-29.9	29.4	-26.7	-61.5	-37.8	3.6	-20.6
	-29.9	-42.6	29.4	-26.7	-37.8	-61.5	3.6	-20.6
	74.2	74.2	50.8	-33.1	33.8	33.8	2.9	70.9
	85.0	85.0	-49.1	16.7	54.9	54.9	1.6	29.2
110	-0.7	-5.9	-8.4	1.5	-15.2	-19.0	-22.8	1.3
	12.1	-9.5	-5.9	11.3	2.9	-22.8	-19.0	14.3
	3.8	12.1	-0.7	-24.5	-10.9	2.9	-15.2	-4.6
	-24.5	11.3	1.5	-9.4	-4.6	14.3	1.3	-10.3
200	-1.2	-1.4	4.2	-1.2	3.6	-4.2	2.8	3.6
	-1.4	-1.2	4.2	-1.2	-4.2	3.6	2.8	3.6
	-1.6	-1.6	8.0	1.9	-2.5	-2.5	0.6	7.3
	5.3	5.3	-2.8	-1.1	12.6	12.6	6.4	-10.5
210	0.7	0.3	0.9	-3.3	-4.3	-0.8	-2.5	0.8
	2.2	0.9	1.3	-0.5	-1.9	0.2	-2.7	-1.1
	-0.4	-2.9	0.0	-2.6	-2.4	-3.7	-0.9	-0.7
	0.0	-3.4	1.4	3.3	1.8	-3.0	1.5	2.9

TABLE 3.2: Hopping integrals up to the fourth-nearest neighbours for the 4-band ( $sp^2+p_z$ ) model. The entries of each given  $4 \times 4$  matrix are associated with the three  $sp^2$  orbitals and the  $p_z$ -like orbital, respectively, and correspond to the numbering shown in Fig. 3.10.

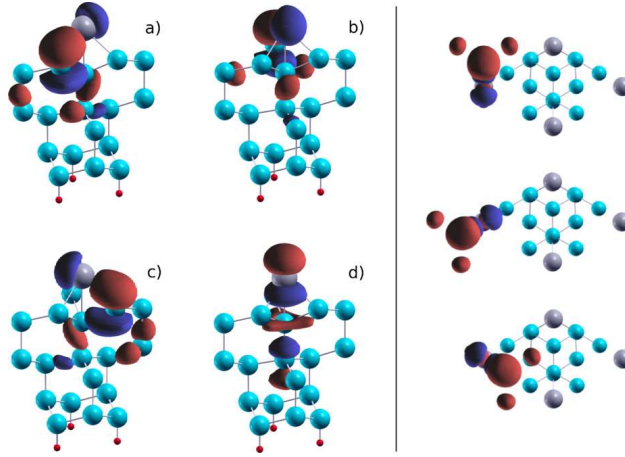


FIGURE 3.9: Left: Wannier orbitals of the 4-band model. The  $sp^2$ -like orbitals are denoted (a)-(c) and point towards the three in-plane next-neighbour substrate atoms of the Sn site. (d) depicts the  $p_z$ -like orbital. Right: The three  $sp^2$ -like orbitals and their orientation relative to the  $\sqrt{3} \times \sqrt{3}R30^\circ$  unit cell geometry, view along the  $z$  axis.

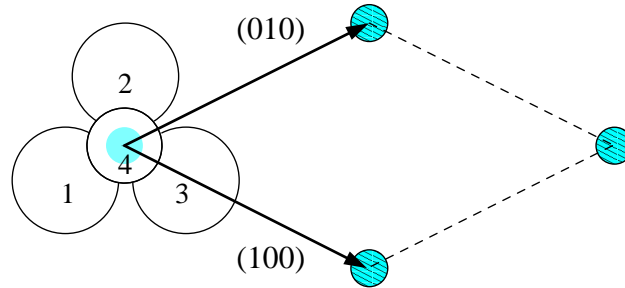


FIGURE 3.10: Schematic diagram of the orbital setup and hopping directions for better understanding of Tab. 3.2. The sketched orbitals 1-3 denote the respective  $sp^2$ -like Wannier functions shown in Fig. 3.9 (compare right side), with number 4 belonging to the remaining  $p_z$ -like function. The numbering corresponds to the row/column numbering of Tab.3.2.

### 3.3.4 Magnetic order.

The question of magnetic order in the adatom layer, the importance of which has already been mentioned in the introduction, goes hand in hand with the geometric and bandstructure setup of the two systems. From the discussion of the localized orbital construction, it is made evident that in particular the well isolated single orbital construction of the Sn/Si(111) system places it very close to a true model setup of the quasi-2D triangular lattice with a single orbital per site. As such, we expect the physics of the system to exhibit traits normally discussed in the context of 2D triangular lattice quantum magnetism. It is known that the Hubbard model at half filling tends towards antiferromagnetic ordering in the large  $U$  limit, which however can not be readily realised in a triangular setup as collinear antiferromagnetic ordering produces a frustrated configuration. It is thus strongly suggested that the same model on a triangular lattice

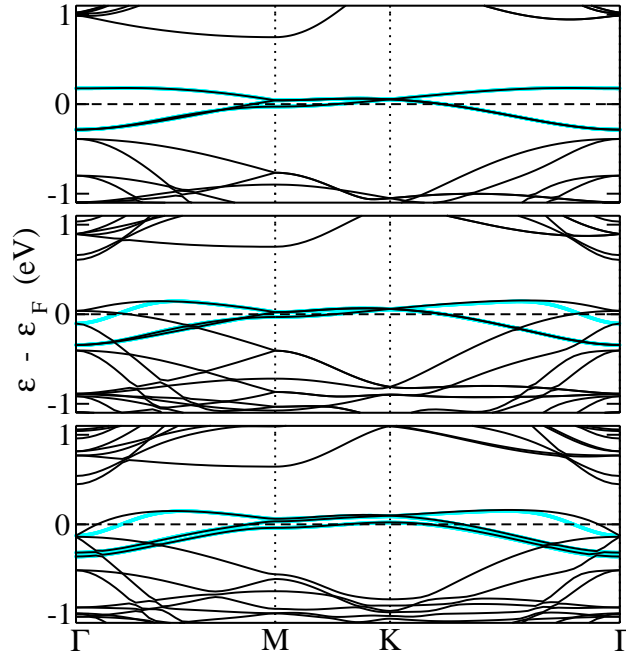


FIGURE 3.11: PBE-GGA bandstructure of the  $3 \times 3$  supercells with the Wannier bands shown in cyan. Top: Sn/Si(111) Middle: *planar* Sn/Ge(111). Bottom: 2D-1U reconstructed unit cell of Sn/Ge(111).

exhibits a  $120^\circ$  noncollinear spin ordering [55]. If our system at hand exhibits AFM nearest neighbour exchange the  $120^\circ$  spin configuration would make a good candidate for an ordered phase, maybe even in the metallic regime.

In our investigation of magnetic behaviour, we mainly focus on the Sn/Si(111) system, as involved low-temperature magnetic ordering is heavily discussed within this context (see introduction and [56, 28]). It should be kept in mind that from the overall system setup, we would expect any magnetic ordering (if at all present) to be very delicate. The constituents of the system (Sn, Si and Ge) do not exhibit tendencies towards high magnetic susceptibility by themselves, and also the orbital setup of  $sp$ -bonding with large principal quantum numbers, with filled  $d$  states, does not readily contribute to formation of large local magnetic moments. Even then, long range magnetic order requires a solid exchange path, which in this case has to be provided via the substrate as the Sn-Sn nearest neighbour distance is rather large ( $\approx 6.7\text{\AA}$ ). On the other hand, the low-dimensional 2D nature of the system may contribute to the emergence of magnetic behaviour, and also the high DOS at the Fermi level of the system (as already mentioned in section 3.3.2) hints at the possibility of flat-band ferromagnetism [57, 58].

The results of our PBE-GGA investigation of magnetic ordering on the Sn/Si(111)  $3 \times 3$  unit cell are shown in Table 3.3. All energies are given with respect to the paramagnetic solution. The ferromagnetic collinear setup (FM), resembling the one described in the work by Profeta and Tosatti [28] can be stabilized for Sn/Si(111), it however turns out

to be the least favorable of the configurations considered. This state is extremely delicate, and its treatment requires *very* strict convergence checks, especially with regard to the k-point mesh. The energy landscape around the local minimum corresponding to the FM configuration is rather flat, such that already small disturbances will cause the DFT self-consistency cycle to proceed towards the nonmagnetic (NM) solution, however slowly. Insufficient k-point-wise convergence may cause this state to be reproduced with significantly different (larger) local moments, which, however, is an artifact which seems to originate in the difficult treatment of the prominent sharp DOS feature already shown and discussed in Figs. 3.3-3.5 and does not influence the fact that this state is still energetically unfavorable. The FM state yields a local magnetic moment of  $0.031 \mu_B$  per adatom, with a total cell magnetic moment of  $0.80 \mu_B$  (with three adatoms in the unit cell), clearly showing that the moments are far from being well localized on the adatom sites. Instead, the total cell moment betrays a large contribution of additional spin polarisation from the remaining substrate sites.

As already mentioned at the beginning of this section, a collinear antiferromagnetic solution on an undistorted triangular lattice is made impossible by frustration. In lieu of this option, we consider two other possible setups, a ferrimagnetic collinear configuration (i.e. two spins up / one down or vice versa on the triangular adatom cluster) and the  $120^\circ$  in-plane noncollinear one. Both configurations are found to be preferable to the nonmagnetic state, with an energy gain of 1.6 meV for the ferrimagnetic collinear and a gain of 3.6 meV for the  $120^\circ$  noncollinear setup. The ferrimagnetic configuration yields a local Sn magnetic moment of  $0.055 \mu_B$  per adatom with a net cell magnetic moment of  $0.44 \mu_B$ . The  $120^\circ$  setup produces slightly larger local moments of  $0.058 \mu_B$  per adatom, and the total cell magnetic moment sums up to zero due to the geometry of the configuration.

Overall, these findings stress that a local magnetic moment picture is not appropriate for the Sn/Si(111) system. Much of the overall magnetic moment contribution stems

Magnetic ordering	E [meV]	M [ $\mu_B$ ]	$M_{Sn}$ [ $\mu_B$ ]
Ferromagnetic	1.5	0.80	0.031
Collinear ferrimagnetic	-1.6	0.44	0.055
$120^\circ$ noncollinear	-3.6	0.00	0.058

TABLE 3.3: Comparison of the different magnetic configurations within the  $3 \times 3$  unit cell of the Sn/Si(111) system. The cell consists of 54 Si, 3 Sn and 9 H atoms. The energies are given with respect to the paramagnetic PBE-GGA solution.  $M_{Sn}$  denotes the magnitude of the magnetic moment localized on the Sn adatom,  $M$  denotes the total moment within the unit cell.

from the spin polarized substrate interstitial regions, at least on the weakly correlated DFT level. Even though the individual local moments are exceedingly small, all three bandstructure codes (MBPP, CP-PAW and VASP) confirmed their nonzero values in the DFT ground state. The state is furthermore stable versus small geometric distortions, in particular the Sn-substrate distance does not significantly influence the qualitative result. The overall calculation result indicates the existence of an antiferromagnetic noncollinear  $120^\circ$  ground state with small, not strictly localized magnetic moments in the Sn/Si(111) system.

We performed similar PBE-GGA calculations for a *planar* Sn/Ge(111)  $3 \times 3$  unit cell, with the goal to assess the influence of the substrate and to directly compare the magnetic behaviour of the two systems. We were, however, unable to stabilize any of the aforementioned magnetically ordered configurations, thus finding the nonmagnetic solution to be the ground state of planar Sn/Ge(111). It appears reasonable to assume this a consequence of the stronger hybridization of the Sn-originated orbitals with the substrate, as discussed in the context of Fig. 3.4 and the bandstructure plots Fig. 3.7 and Fig. 3.11, which should generally weaken the magnetic tendencies on the Ge substrate when compared to silicon. We did not investigate the magnetic behaviour of the Sn/Ge(111) 2D-1U distorted cluster, which is left for possible further studies.

This concludes the investigation of magnetic behaviour on the DFT level. We will briefly return to this topic in the many-body section of this chapter, as the RISB formalism gives us access to the spin-spin correlation functions of the three-adatom triangular cluster and allows to investigate their dependence on the local Coulomb  $U$ .

### 3.4 Electronic correlations: Explicit many-body results

Now that a set of effective Wannier Hamiltonians has been constructed from the DFT results obtained during the previous section and all necessary discussions on the DFT level have been concluded, we may proceed to improve upon our previous calculations by introducing explicit many-body effects. In the following, we will elaborate on the realistic one-band single site and triangular cluster models previously constructed for both the Sn/Si(111) and the Sn/Ge(111) systems and the influence of explicit electronic correlations.

All calculations shown within this section were performed in the paramagnetic regime, i.e. we do not treat the long-range ordered states discussed in the previous section. As the results of section 3.3.4 show magnetic order to be a delicate affair with a rather small energy scale, explicit analysis of such states within a many-body approach is left

for possible future studies. We will however still be able to make certain conclusions on magnetic behaviour, which will be elaborated upon in section 3.4.2.

### 3.4.1 LDA+DMFT

With the Wannier Hamiltonians available, the main obstacle to the successful application of many-body techniques, namely the high number of orbitals involved into the physics of the system, has been effectively removed at the cost of substituting the full problem for an effective low-energy description of the material. However, with the separated surface bands discussed in the previous section and their accurate representation in terms of the MLWFs, we can expect the effective model to well reproduce the low-energy physics. In the following, we will treat the effective Hamiltonian within the DMFT framework, using a Hirsch-Fye QMC impurity solver.

Before we go on to directly discuss the DMFT results, a short analysis of the physics involved seems in order. As the width of the partially filled band(s) in question,  $W \sim 0.4$  eV is rather small, already small values of  $U$  (comparable with band width) may introduce strong correlation effects into the system, which is also quite fortunate since one generally would not expect particularly large values of the Hubbard  $U$  for a Sn5s/5p-based orbital setup. Above a certain critical  $U$  value, we expect the system to undergo a metal-to-insulator transition. It is this transition region and its dependence on geometry and substrate choice which has our attention.

With this said, it should be kept in mind that in general, the explicit value of the Hubbard  $U$  will still depend on the choice of the local basis. In a small onsite basis, the effective Wannier orbitals will generally turn out to be less localized than in a large multi-orbital basis. In addition to that, the strength of screening effects will differ depending on the material in question, i.e. screening in metals is far more effective than on a semiconductor surface, in particular for the direction perpendicular to the surface plane. Since all these aspects will influence the effective  $U$  value of the system, a proper evaluation of the Coulomb interaction strength always requires the context of the effective model within which the calculations have been performed.

We begin our discussion with the paramagnetic single-site DMFT(QMC) calculations for the realistic one band models introduced and constructed in section 3.3.2. The spectral functions obtained for different values of Hubbard  $U$  are shown in Fig. 3.12. These were obtained from the output DMFT Greens functions by means of the maximum entropy method. As such, they display a certain measure of effective smearing of the individual features, a signature of the approach. Due to the relatively simple nature of the one-band modeling, the general behaviour follows the usual expectations: with an increasing

U, the low energy quasiparticle peak becomes more pronounced and narrow, with little variation in spectral weight directly at the Fermi level (a feature of the half-filled one band model). At the same time, a distinguished lower and upper Hubbard band (corresponding to incoherent atomic-like excitations) emerges at higher U, with spectral weight being increasingly shifted away from the Fermi level.

The calculations shown in Fig. 3.12 were performed at  $\beta = 200 \text{ eV}^{-1}$ , which corresponds to  $T \sim 58 \text{ K}$  ( $\beta = 1/k_B T$ ). The Sn/Si(111) system, shown in the top panel, reaches a Mott-insulating state at  $U_c \sim 0.6 \text{ eV}$ , with a slightly higher  $U_c$  for Sn/Ge(111). (In fact, the transition is of weak first-order character in both calculations, and thus this energy region is actually governed by two critical interaction values  $U_{c1}$  and  $U_{c2}$ . The corresponding hysteresis loop, however, is tiny and hard to resolve. Due to this, and the relative simplicity of our model, we did not map out the two branches explicitly.) Within the insulating Mott state at  $U \sim 0.7 \text{ eV}$ , the energy gap between the upper and the lower Hubbard band is on the order of  $\sim 0.2 \text{ eV}$ , with the Hubbard bands themselves situated at approximately  $0.3 \text{ eV}$  above and below the Fermi level. This result compares nicely with the findings in [27, 59], where a region of increased spectral weight transfer was identified by photoemission experiments at roughly  $0.2$  to  $0.45 \text{ eV}$  below Fermi. Thus we conclude that within the single site one-orbital model already a small Hubbard U, only slightly larger than the band width, drives both systems into the insulating Mott state.

While a single site model allows for a first glimpse of the many-body physics, the planar Sn/Ge(111) geometry it corresponds to has already been discussed to not represent the true ground state of the system. To take into account the structural distortion, we now move on to treat the one-orbital triangular cluster models within (cluster) DMFT [60, 61, 62]. This numerically more demanding calculation also offers the additional benefit of taking into account the inter-site self-energy effects within the basic Sn three-site cluster. As we have constructed triangular cluster models for both distorted Sn/Ge(111) and Sn/Si(111), we are now able to assess the influence of the different substrates/geometries by direct comparison.

The spectral functions for the triangular cluster models are shown in Fig. 3.13. The calculations were performed at  $\beta = 70 \text{ eV}^{-1}$ , which corresponds to  $T \approx 166 \text{ K}$ , the reason for the somewhat higher temperature in comparison to the one-orbital calculations being the significantly increased computational demands of the cluster setup. The spectral function of the Sn/Si(111) cluster is shown in the top panel. The critical  $U_c \sim 0.55 \text{ eV}$  is now slightly lower than for the one-band model, with a somewhat reduced energy gap, a result which was checked to not stem from the increased computation temperature. Also, a stronger asymmetry between the upper and lower Hubbard band can be observed, with a stronger reduction in spectral weight below  $E_F$ .

The results for the  $3 \times 3$  2D-1U distorted Sn/Ge(111) cluster are shown in the bottom

panel, with the numbers corresponding to local site occupations. It is important to remark that the two downwards-shifted Sn adatoms are in fact not equivalent due to the different orientation of the local orbitals with respect to the upwards-shifted Sn. (Each orbital has a 'lobe' pointing towards *one* of its neighbours within the local triangular cluster, not both.)

The (d)-adatoms initially each have a lower occupation compared to (u)-Sn, (0.819/0.802 electrons per (d)-site vs. 1.378 for (u) at  $U = 0$  eV) with a small difference introduced by the aforementioned inequivalence. While noticeable in the local occupation numbers, the differences in the spectral functions of the (d)-adatoms are very small, which is why an average over the two is shown in Fig. 3.13. The difference between the (u) and (d) spectral functions, on the other hand, is clearly visible, with the obviously higher initial spectral weight below the Fermi level for the upwards-shifted adatom. With an increasing onsite  $U$  value, the filling imbalance is evened out among the sites as the system strives to minimize energy costs due to double occupation, eventually again undergoing a Mott transition at a slightly lower value of  $U_c \sim 0.55$  eV, at which point the individual occupations approach the expected 1 electron per site. Again, a stronger reduction of the spectral weight can be observed in the unoccupied part below the Fermi level, which is now even more pronounced than on the Sn/Si(111) cluster.

While the spectral functions offer a lot of information, this section also highlights the difficulty to achieve a good resolution of the qualitative differences in the values of critical  $U$ . So, after having discussed the DMFT results we will now move on to a complementary RISB analysis of the systems at hand.

### 3.4.2 LDA+RISB

As opposed to the DMFT calculations, the RISB approach allows for a time-efficient fine-scale scans of system behaviour due to the relative ease of the numerics. In addition to that, some of the observables, like the quasiparticle weight  $Z$  or the intersite spin correlations are not as readily available within other computational schemes. It should however be kept in mind that the RISB saddle-point approximation neglects quantum fluctuations, in particular when directly comparing with DMFT results.

Fig. 3.15 shows the RISB quasiparticle weights  $Z$  for both the single-site and the cluster setups. The one-band calculations are shown in the top panel. The quasiparticle weight decreases steadily with increasing  $U$ , showing a first-order transition from paramagnetic metal to paramagnetic insulator for both Sn/Si(111)- and Sn/Ge(111)- $\sqrt{3} \times \sqrt{3}R30^\circ$ , with respective critical  $U$  values of  $U_c \sim 0.75$  eV for the Si and  $U_c \sim 0.78$  eV for the Ge substrate system. The somewhat higher value for Sn/Ge(111) follows the trend already

displayed by the DMFT calculations, while the overall higher critical  $U$  values can be attributed to the aforementioned neglect of quantum fluctuations by the RISB formalism.

The cluster calculations are shown in the bottom panel. A clear overall reduction in the critical  $U$  values needed to drive the systems into the insulating state is obvious (again retracing the DMFT results), which is due to the nearest-neighbour self-energies now being explicitly included in the calculations. Furthermore, the first-order character of the transitions is strengthened in the cluster modeling.

The Sn/Si(111) can now be clearly seen to possess a significantly lower  $U_C$  than the Ge substrate setups. The difference between (artificial) flat Sn/Ge(111) and the realistic 2D-1U distorted configuration is more subtle, but the result is nevertheless both well-checked and very reasonable from the physical point of view. The local Coulomb interaction has to force additional charge transfer to compensate for the initial asymmetrical charge distribution in the 2D-1U system before the onset of the Mott insulating state can follow, thus leading to an increased critical  $U$  value for this system. While the difference in  $U_C$  may seem small in absolute terms, one should keep in mind that the values are enhanced by the context of the exceedingly small overall bandwidth of  $\sim 0.3$  eV.

The evolution of the individual site occupations for the 2D-1U Sn/Ge system is shown in Fig. 3.14, with the inset showing the geometry of the triangular setup. As already briefly discussed in the DMFT section, the (u) site, shown in green, initially has a higher occupation of around 1.4 electrons per site, which then can be seen to steadily drop towards  $n = 1$  as the value of  $U$  increases (changing the slope of the decrease at  $U = 0.25\text{eV}$ ), with a sharp jump at the MIT transition value. At the same time the initially slightly different occupations of both downwards-shifted adatoms increase from their initial values of  $n \approx 0.8$ , mirroring the behaviour of the (u)-site. This is also in line with the previously discussed DMFT results.

### 3.4.2.1 LDA+RISB: Magnetism

Finally, the RISB formalism enables us to shed some additional light on the matter of magnetic behaviour, a topic already discussed in the DFT section of this chapter. Fig. 3.16 displays the development of the spin-spin correlation functions  $\langle \mathbf{S}_i \mathbf{S}_j \rangle$  between the Sn sites of the triangular clusters (remember that we stay in the paramagnetic regime). It can be clearly seen that the spin-spin correlations remain negative in all cases, thus displaying overall AFM character, a behaviour readily explained by the superexchange

mechanism introduced via the onsite  $U$ . We thus expect the magnetic traits of the respective systems to become more pronounced with increasing interaction strength.

The top panel of Fig. 3.16 shows the spin-spin correlation functions for the flat cluster setups. The calculations reveal the AFM tendencies of Sn/Si(111) to be stronger than in Sn/Ge(111), thus lending support to our PBE-GGA investigation of magnetic order presented in section 3.3.4. This trend becomes more pronounced with increasing  $U$ , even though the Sn/Ge system reaches a somewhat higher absolute value right below its MI transition point. As all three sites are equivalent by symmetry in these setups, only one plot per system is shown.

The results for the 2D-1U distorted Sn/Ge(111) are shown in the bottom panel. As all three adatoms are different in this setup, three distinct values for  $\langle \mathbf{S}_i \mathbf{S}_j \rangle$  are readily expected (for the numbering of the individual sites, please again refer to the inset of Fig. 3.14). Surprisingly however, these correlation functions scale rather differently with increasing  $U$ , a feature that can be traced back to the different values of the hopping amplitude  $t$  between the three distinct orbitals. The upwards-shifted Sn(3) site possesses a laterally slightly more extended Wannier orbital, and as such the orbital lobe pointing towards Sn(2) achieves a wider range, increasing the hopping amplitude between these two sites. On the other hand there is no orbital lobe pointing from Sn(3) to Sn(1) (but rather the other way around), which results in a comparatively lower hopping.

The spin-spin correlation functions between the individual sites behave accordingly to these observations. The Sn(2)-Sn(3) spin correlations have the overall largest negative value, displaying a further decrease with increasing  $U$  and clearly diverging AFM-like behaviour in the close proximity of the Mott transition. At the same time, the Sn(1)-Sn(3) spin-spin correlations show opposite tendencies, revealing a behaviour which could hint at eventual FM coupling (with the values still remaining negative in the  $U < U_c$  region, though). The remaining Sn(1)-Sn(2) pair displays featureless, slowly decreasing behaviour up to the Mott transition, with values in between the other two functions. While one should remember that we are still in the paramagnetic regime here, these results provide important hints at the magnetic tendencies within the system regardless of whether or not these correlations may be prominent enough to stabilize long range order. In particular, intriguing physics may arise in combination with the assumed ability of the Sn/Ge(111) to fluctuate between the 2D-1U and 1D-2U states at higher temperatures (see introduction).

Finally, we would like to make a further connection to the magnetic behaviour of the Sn/Si(111) system, as already discussed in the DFT part. Fig. 3.17 shows the behaviour of the effective onsite spin quantum number  $S$  and the average angle  $\alpha$  between the effective spins on the triangular cluster. With the local values of  $\mathbf{S}_i^2$  and the correlation functions  $\langle \mathbf{S}_i \mathbf{S}_j \rangle$  available from the RISB formalism, the value of  $S$  can be deduced from  $|\mathbf{S}_i| = \sqrt{\mathbf{S}_i^2} = \sqrt{S(S+1)}$  and the average angle  $\alpha$  results from  $\langle \mathbf{S}_i \mathbf{S}_j \rangle = \langle |\mathbf{S}_i| |\mathbf{S}_j| \cos \alpha \rangle$ .

As expected, for small  $U$  the itinerancy of the electrons leads to a spin quantum number  $S$  well below the value of  $1/2$ , which would correspond to maximum localization. With increasing  $U$ , the value of  $S$  increases accordingly, however falling short of fully saturating at the onset of the insulating regime. This is understandable considering the significant first-order character of the transition. Furthermore, the low initial localization is well in line with our DFT results.

The average  $\alpha$ , shown in the lower panel, demands a more involved discussion. As we are in the paramagnetic state here, the local moments have no preferred spatial direction by themselves, i.e.  $\langle \mathbf{S}_i \rangle = 0$  holds on every individual site. Already at  $U = 0$  however, the average angle  $\alpha$  between any two spins amounts to a value slightly larger than  $90^\circ$ , corresponding to a weak preference towards antiferromagnetic alignment and in line with the previous results. This tendency can be seen to increase with  $U$  until it finally reaches a value of  $\alpha \approx 100^\circ$  right below the Mott transition.

This is relevant in the context of the possible limiting cases for the  $\alpha$  value. A trivial collinear FM order would result in  $\alpha = 0$ , a case which can be clearly dismissed here. Real in-plane triangular lattice antiferromagnetism provides a limiting value of  $\alpha = 120^\circ$ , which is however the same as in the hypothetical case of a frustrated collinear antiferromagnetic local configuration, with two FM-coupled spins both coupling antiferromagnetically to the remaining one. As much as these two cases are fundamentally different, the value of  $\alpha$  does not provide enough information to clearly distinguish between them.

Still, we are able to corroborate our PBE-GGA result of overall antiferromagnetic tendencies for Sn/Si(111), further strengthened by increasing  $U$ . Onset of a true long range magnetic order already in the metallic regime is strongly suggested by the DFT results, even though model studies (e.g [55]) generally predict its appearance in the insulating state close to the Heisenberg limit. As such, a direct many-body investigation of the ordered magnetic phase should be a future goal.

### 3.5 Conclusions and outlook

With this, we conclude our study of the Sn/Si(111) and Sn/Ge(111)  $\alpha$ -surface systems, with the results presented here published in [63]. We have constructed both single site and triangular cluster effective low-energy models for the two systems and analyzed the influence of electronic correlations on the quasi-2D surface state. The Mott transition is found to take place at already moderate  $U$  values of  $0.5 - 0.6$  eV for both systems, a result consistent with the low surface band width. Nevertheless, the locality in these systems is not particularly strong. Our many-body studies further reveal an intriguing

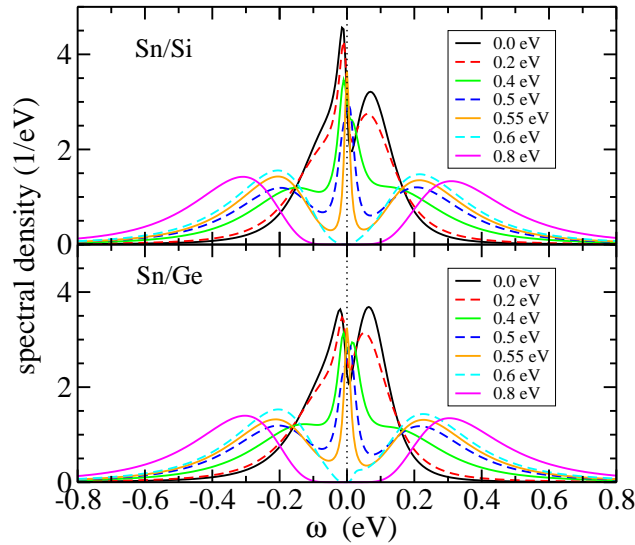


FIGURE 3.12: Single site DMFT(QMC) spectral functions for the two one-band models for different values of onsite  $U$ . Top:Sn/Si(111). Bottom:Sn/Ge(111). Calculations were performed at  $\beta = 200 \text{ eV}^{-1}$ , corresponding to  $T \sim 58\text{K}$

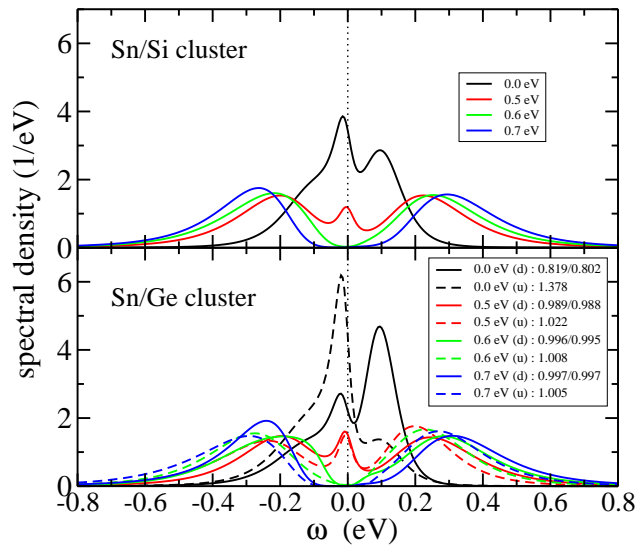


FIGURE 3.13: Cluster DMFT(QMC) results for planar Sn/Si(111) (top) and 2D-1U distorted Sn/Ge(111) (bottom) for different values of  $U$ . The numbers denote the local occupations for the individual sites, with two different numbers given for the (d) sites as they are slightly different by symmetry. This difference is not readily noticeable in the spectral functions, and as such only the averaged spectral function for the two downwards-shifted sites is shown for the sake of clarity. Calculations were performed at  $\beta = 70 \text{ eV}^{-1}$  ( $T \sim 166\text{K}$ ).

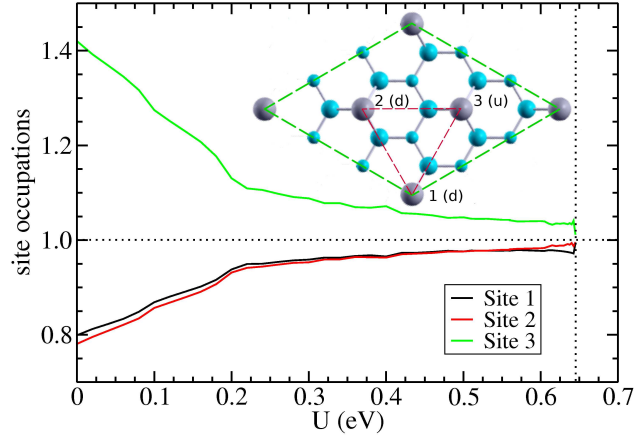


FIGURE 3.14: Orbital occupation of the three inequivalent Sn sites of the 2D-1U distorted Sn/Ge(111)  $3 \times 3$  supercell, from a RISB cellular cluster calculation. The inset shows a top view of the  $3 \times 3$  unit cell with the corresponding adatom designations. The triangular cluster utilized for the model is marked in red.

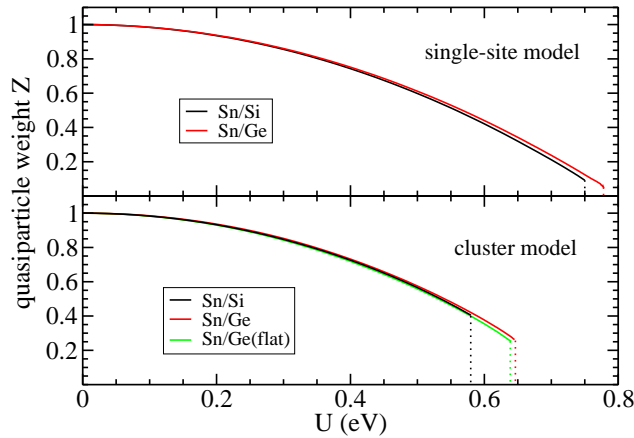


FIGURE 3.15: RISB quasiparticle weight  $Z$  for the single-site (top) and triangular cluster models (bottom). The dashed vertical lines marking the individual critical  $U$  values are guides for the eye.

interplay of the electronic correlations with the 2D-1U geometrical distortion present in the Sn/Ge(111) system. Another central point, confirmed by both PBE-GGA and many-body studies, is the tendency towards antiferromagnetic correlations present in both systems, a result anticipated previously in model(-like) treatments [64, 31]. While our DFT results hint at the existence of true noncollinear antiferromagnetic long-range order in Sn/Si(111), distorted Sn/Ge(111) exhibits nontrivial spin correlation functions strongly coupled to the details of the surface reconstruction. The latter results in particular call for a more thorough investigation of the ordered phases with the help of many-body techniques, also taking the influence of the substrate into account. Further possible research avenues include the question whether solely local Coulomb interactions are truly sufficient to actually capture the physics of these systems, a thought fueled

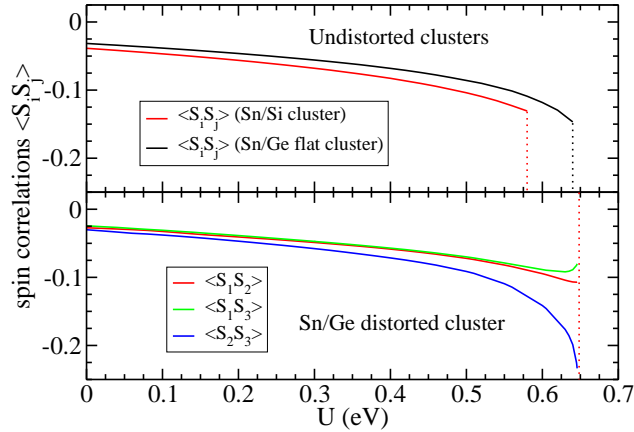


FIGURE 3.16: RISB spin-spin correlation functions for the triangular cluster models. Top: Sn/Si(111) and *planar* Sn/Ge(111) triangular clusters. Bottom: Distorted 2D-1U Sn/Ge(111). The subscripts in the bottom panel correspond to the adatom designation shown in the inset of Fig. 3.14. Vertical lines mark critical  $U$  values and are guides for the eye.

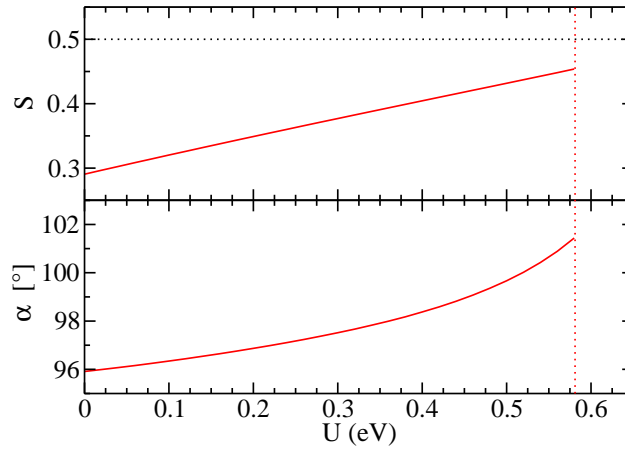


FIGURE 3.17: Top: Dependence of the spin quantum number  $S$  on the interaction strength  $U$  for the Sn/Si(111) triangular cluster. Bottom: Average angle  $\alpha$  between the individual spins for the same setup.

by the rather moderate locality of both the orbitals and the magnetic moments. Also, Sn/Ge(111) poses the question of interplay between the electronic correlations and the geometrical reconstruction, seeing as both are tied via the local occupation numbers of the inequivalent adatom sites and also connected to the individual Sn-Sn spin correlation functions. Ultimately, it would be interesting to investigate this system while allowing for the effects of electronic correlation to couple back to the geometry of the surface, e.g. via a charge self-consistent implementation of LDA+DMFT [8].

Lastly, after the conclusion of this work, some further light has been shed on the nature of the magnetic ordering in Sn/Si(111)- $\sqrt{3} \times \sqrt{3}R30^\circ$  by the study of Li *et al* [65]. Their dual-fermion approach to this system, which is able to take nonlocal correlations into

account, reveals the spin susceptibilities of the system to have important contributions at both  $\mathbf{K}$  and  $\mathbf{M}$  points of the Brillouin zone, corresponding to an intriguing combination of both  $120^\circ$ -AFM and row-wise AFM order tendencies, which is consistent with our own results presented here. Also, the authors advise future researchers on this system to include the next-nearest-neighbour hopping into their models. As such, the exact nature of the surface state magnetism in this system still asks for further investigations.



## Chapter 4

# Implications of strongly reduced symmetry: Dzyaloshinskii-Moriya interaction in strongly correlated itinerant systems.

### 4.1 Introduction

Understanding the magnetic behaviour of adatoms in surface/layered low-dimensional setups ties in with the general interest in the effects low symmetry environments have on magnetic systems. There exists a multitude of different materials where the reduced dimensionality is believed to be of central importance to the intrinsic physics. The anisotropy of the magnetic exchange induced by such geometry in bulk systems has been recently studied, among others, in multiferroic materials [66, 67] such as for example bismuth ferrite  $\text{BiFeO}_3$  where the canting of the ferromagnetic sublattices results in a weak net ferromagnetic moment and is deemed important for the coupling between the magnetic and electronic degrees of freedom. Another case of low-dimensional environment occurs naturally on surfaces, with a recent prominent example being manganese on a tungsten (110) substrate [68], where Bode *et al.* could demonstrate the spin-spiral behaviour of the surface to be a direct consequence of the reduced symmetry, and the work of Zhu *et al.* [69] concerning surface effects on topological insulators. However, interplay between spin degrees of freedom and peculiarities of the crystal environment, as are at work in all these cases, obviously require a mechanism with which local spin moments may couple to the lattice geometry.

The ready candidate is the spin-orbit coupling, and work central for the understanding

of its function in such systems has been done over fifty years ago by Dzyaloshinskii [70] and Moriya [71], who derived an effective spin-spin interaction term from the spin-orbit coupling in low-symmetry environments, the so-called Dzyaloshinskii-Moriya (DM) interaction. This is a central concept for the work presented in this chapter, and as such we will discuss it briefly, mainly following the original publications.

The original work of Dzyaloshinskii, published in 1957, deals with the phenomenon of extremely weak ferromagnetic response measured in certain antiferromagnetic crystals (e.g.  $\alpha$ -Fe<sub>2</sub>O<sub>3</sub>, MnCO<sub>3</sub> and CoCO<sub>3</sub>). The corresponding magnetic moments contributing to the ferromagnetism were estimated to be on the order of 1 percent (or even less) of the nominal local moment value, which was taken as an indication of some new mechanism being responsible for these effects, as standard ferromagnetism would be expected to produce far larger local ferromagnetic contributions. In his effort to shed some light on these new physics, Dzyaloshinskii went on to discuss and compare two particular materials, namely the  $\alpha$ -Fe<sub>2</sub>O<sub>3</sub>, where the aforementioned behaviour has been measured in 1952 [72] and the structurally isomorphous Cr<sub>2</sub>O<sub>3</sub>, where this effect is absent.

The unit cells and magnetic setup of both systems is shown in Fig. 4.1. Both exhibit the same rhombohedral geometry of the crystal structure while being different with regards to magnetic symmetry. Dzyaloshinskii's approach now was to consider whether or not a given symmetry is general enough to allow for a net magnetic moment within the cell, for example by allowing the individual moments to *rotate towards each other*, resulting in a small ferromagnetic contribution. This turns out to be impossible in Cr<sub>2</sub>O<sub>3</sub> without violating the symmetry, but possible in  $\alpha$ -Fe<sub>2</sub>O<sub>3</sub> where the free energy written in terms of local spin variables then includes expressions of the form

$$\mathbf{D} \cdot (\mathbf{S}_1 \times \mathbf{S}_2)$$

with  $\mathbf{S}_{1,2}$  denoting spins on neighbouring lattice sites and the vector quantity  $\mathbf{D}$  dictated by the system symmetry.

As such, low enough magnetic symmetry *allows* such configurations. It was in the work by Moriya [71] three years later that the anisotropic spin interaction thus suggested by Dzyaloshinskii has been shown to actually stem from the combined effects of spin-orbit coupling and Anderson's superexchange [73]. Moriya went on to derive rules for the emergence of this interaction in realistic geometries, explicitly demonstrating how a low-symmetry environment is required for a nonzero value of  $\mathbf{D}$ .

Thus, anisotropic magnetic exchange emerges naturally in many of the more complex material setups, and as such has already been subject to intense study in the past, for example on triangular lattices [74] or in dimer chains [75]. However, theoretical studies have up to now nearly exclusively dealt with pure spin models, while neglecting to consider effects of itinerancy *or* to take into account explicit many body-effects. Only

recently has there been a rising interest in combining the Hubbard model with spin-orbit terms.

Recent developments suggest that interactions of the Dzyaloshinskii-Moriya type play a major role in many strongly correlated materials, with a particular interest in doped cuprate systems [76, 77, 78]. The innate two-dimensional nature of these materials, in conjunction with the tilting and rotations of the  $\text{CuO}_6$  octahedra which occurs depending on the doping level, creates a low symmetry environment in which the DM interaction is believed to make a non-negligible contribution to the rich magnetic behaviour observed in these systems. Other intriguing materials include layered manganite systems [79, 80], where noncollinear magnetic behaviour emerges at certain doping levels, but also some mono-oxides (e.g. CoO) [81]. Naturally, strongly correlated surface systems also fall into this category (due to the innate low symmetry), such as the quasi-two-dimensional organic  $\kappa$ -(BEDT-TTF) $_2$ X materials [82], which, depending on the anion X, may exhibit anisotropic magnetism close to the metal-insulator transition.

As such, within the scope of this work we are interested in a minimal modeling of the DM interaction in the strongly correlated metallic regime. As standard direct and indirect exchange mechanisms favor collinear spin alignment, we expect the competition between these and the tendency towards perpendicular spin orientations brought about by Dzyaloshinskii-Moriya to give rise to interesting physics and nontrivial spin arrangements. According to the examples given above, our primary focus will lie on two distinct model setups, allowing for a somewhat canonical approach to the different material types.

The first (and main) part of this chapter deals with the properties of the Hubbard bilayer model in presence of Dzyaloshinskii-Moriya interaction. The setup consists of two coupled single-band Hubbard planes [83, 84, 85, 86, 13, 87, 88, 55], with the DM coupling acting between them, and we will mostly concentrate on the study of the competition between the collinear antiferromagnetic state and the canted configurations of DM-kind in the high  $U$  metallic regime. This particular model has been chosen to serve as an archetype for quasi-2D layered systems, akin to the aforementioned cuprates, and it is our intent to uncover the basic phenomenology of physics emerging in such geometries. The latter part of this chapter is devoted to the investigation of the so-called two-impurity Anderson model (TIAM) [89, 90, 91, 92, 93, 94, 95]. This model consists of two local magnetic impurities coupled to the same bath and serves as a generalisation of the magnetic-adatoms-on-surface type of system. As an additional feature, this model also includes both the so-called Ruderman-Kittel-Kasuya-Yosida (RKKY) interaction between the impurities (mediated via the common bath), which has been shown to contribute strongly to the magnetic behaviour of certain adatom configurations [96], and the single-impurity Kondo physics. As such, we expect interplay between direct exchange, RKKY, DM and the Kondo mechanism within this model (albeit no long range order,

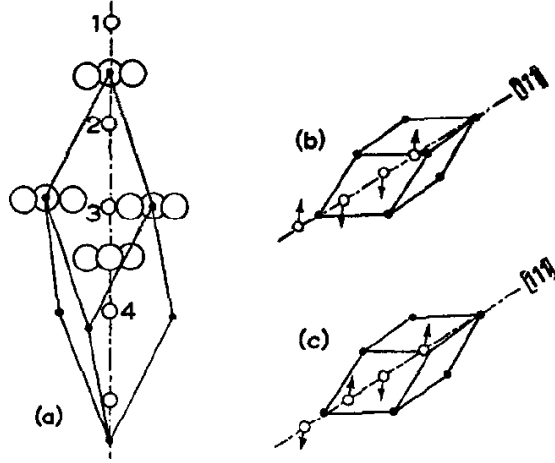


FIGURE 4.1: Picture taken from original work of Dzyaloshinskii [70]. (a) - Unit cell of  $\alpha - Fe_2O_3$  and  $Cr_2O_3$ . Large circles: oxygen ions. Small circles: Ferric ions. (b) - Antiferromagnetic spin ordering in  $\alpha - Fe_2O_3$ . (c) - Same for  $Cr_2O_3$ .

due to finite size).

Of course, the aforementioned models are too generic to accurately capture the physics of the specific materials in every detail. Rather, we intend to discuss the general phenomenology emerging through the addition of the Dzyaloshinskii-Moriya interaction to a strongly correlated, itinerant system. As will become clear over the course of this chapter, the effects are highly non-trivial and serve as a strong motivation for more detailed, specifically material-tailored studies in the future.

## 4.2 Hamiltonians and theoretical treatment.

The geometry of the Hubbard bilayer model is shown in Fig. 4.2. The two two-dimensional infinite square lattice planes, with one orbital per site, each have a simple identical intra-layer dispersion governed by a nearest-neighbour hopping  $t$  and an on-site Coulomb repulsion  $U$  associated with each individual site. The planes are coupled to each other via a perpendicular inter-layer hopping  $t_{\perp}$  and the Dzyaloshinskii-Moriya interaction, specified via the vector integral  $\vec{D}$ . The corresponding model Hamiltonian reads

$$\begin{aligned}
 H_{BL} = & -t \sum_{\substack{\alpha\sigma \\ \langle i,j \rangle}} (c_{\alpha i\sigma}^{\dagger} c_{\alpha j\sigma} + \text{H.c.}) + t_{\perp} \sum_{i\sigma} (c_{1i\sigma}^{\dagger} c_{2i\sigma} + \text{H.c.}) \\
 & + U \sum_{\alpha i} n_{\alpha i\uparrow} n_{\alpha i\downarrow} + \sum_i \mathbf{D} \cdot (\mathbf{S}_{1i} \times \mathbf{S}_{2i})
 \end{aligned} \tag{4.1}$$

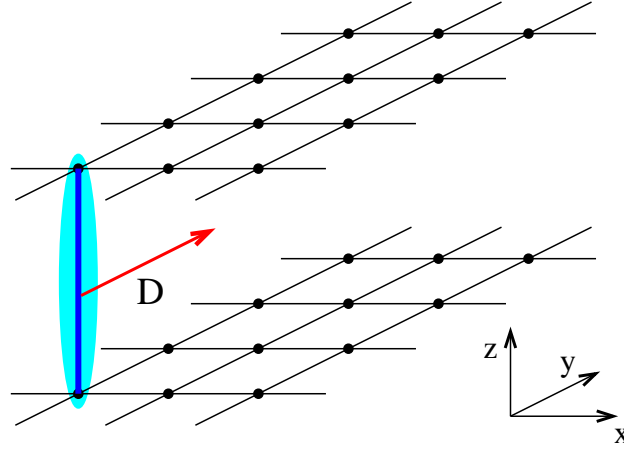


FIGURE 4.2: Hubbard bilayer model with interlayer DM interaction. The two-site cluster which acts as the periodic unit is marked in cyan, with perpendicular hopping  $t_{\perp}$  symbolized by a blue line. The Dzyaloshinskii-Moriya vector  $\mathbf{D}$  is denoted with a red arrow and is generally chosen to point in the  $y$  direction.

where  $c_{\alpha i \sigma}^{(\dagger)}$  creates (or annihilates) an electron of spin  $\sigma = \uparrow, \downarrow$  in layer  $\alpha = 1, 2$  at the lattice site  $i$ , and the individual components of the spin operator  $S_{\alpha i}^{(\nu)}$ , with  $\nu = x, y, z$ , are defined via  $S_{\alpha i}^{(\nu)} = 1/2 c_{\alpha i \sigma}^{\dagger} \tau_{\sigma \sigma'}^{(\nu)} c_{\alpha i \sigma'}$ .

In general, most geometries which are able to produce the DM interaction in the first place result in  $\mathbf{D}$  being perpendicular to the bond between the involved lattice sites. Within our general model, the value and direction of  $\mathbf{D}$  is a matter of choice, but would become a material-specific parameter in a more accurate setup, conveying information about e.g. positioning of additional atoms not directly involved in the 2D layer structure. In the context of cuprates that could, for example, include oxygen atoms contributing to the interlayer coupling, or basically any additional constituent occupying a low-symmetry position in the unit cell (seeing as broken inversion symmetry is required for  $\mathbf{D} \neq 0$  at all). As such we choose  $\mathbf{D}$  to point in the  $y$  direction,  $\mathbf{D} = D \vec{e}_y$ . Both layers exhibit a simple two-dimensional square lattice dispersion relation with the bandwidth  $W = 8t$ .

The two-impurity Anderson model (TIAM) will be discussed in the second part of this chapter. We write this model as

$$\begin{aligned}
 H_{\text{TIAM}} = & \sum_{\mathbf{k}\sigma} \varepsilon_{\mathbf{k}} c_{\mathbf{k}\sigma}^{\dagger} c_{\mathbf{k}\sigma} + \varepsilon_d \sum_{i\sigma} n_{i\sigma} \\
 & + V \sum_{\mathbf{k}i\sigma} (c_{\mathbf{k}\sigma}^{\dagger} d_{i\sigma} + \text{H.c.}) + t_{12} \sum_{\sigma} (d_{1\sigma}^{\dagger} d_{2\sigma} + \text{H.c.}) \\
 & + U \sum_i n_{i\uparrow} n_{i\downarrow} + \mathbf{D} \cdot (\mathbf{S}_1 \times \mathbf{S}_2)
 \end{aligned} \tag{4.2}$$

The impurity electron operators are denoted  $d_{i\sigma}^{(\dagger)}$  ( $i = 1, 2$ ) with the impurity level energy

$\varepsilon_d$  and the inter-impurity hopping  $t_{12}$ . The common bath enters explicitly via its dispersion  $\varepsilon_{\mathbf{k}}$  and the corresponding creation/annihilation operators  $c_{i\sigma}^{(\dagger)}$ , and the coupling between impurities and bath is denoted by  $V$ . The Coulomb interaction  $U$  is introduced on the impurities only, with  $n_{i\sigma} = d_{i\sigma}^\dagger d_{i\sigma}$ . The dispersion of the bath is chosen to be that of a simple cubic lattice with bandwidth  $W = 12t$ , and the  $\mathbf{D}$  vector is again chosen to point in the  $y$  direction. Although both impurities are coupled to a common bath in this model, we still assume  $V$  to not depend on  $k$ , formally corresponding to vanishing distance between the impurities. As such, only the local part of the RKKY interaction is included in our model. The treatment of nonlocal RKKY (as well as a *correlated* common bath, for that matter) is a possible future research avenue.

All calculations within this chapter were performed using the rotationally invariant slave-boson approach (RISB), which was already introduced in the theory part, and, to a lesser extent, during the discussion of the  $\alpha$ -surfaces in chapter 3. The main point which makes this formalism most suitable for this task is the ability to account for full orbital and spin rotational invariance, a necessity when dealing with local noncollinear configurations in a many-body framework. Furthermore, it gives us access to the low-energy behaviour including the linear part of the self-energy, quasiparticle weights, atomic multiplet weights on the cluster, and all local operator expectation values. Note, however, that in return Hubbard bands can not be taken into account within this approach and the full spectral function is not available.

The Hubbard bilayer model is treated by using a two-site cluster which connects the two nearest-neighbour (NN) lattice sites between the layers. As such, it can account for spin-spin correlations involving the two cluster sites and the cluster self-energy  $\Sigma_{12}(\omega)$  (the linear part), including the off-diagonal terms. The direct exchange term, proportional to  $t^2/U$ , is properly included beyond single site in our models, while the DM term  $\mathbf{D}(\mathbf{S}_1 \times \mathbf{S}_2)$  is treated explicitly within the local cluster. Theoretically, it should be possible to reproduce the DM anisotropic exchange from a general spin-orbit term treated within RISB (along the lines of [97]) in a future effort.

Within the two-impurity Anderson model (TIAM), the bath enters explicitly via its band dispersion, resulting in an effective three-orbital setup. Thus, the bath degrees of freedom are not integrated out, but are handled explicitly instead. All of the calculations presented here deal with an uncorrelated bath scenario,  $U_{bath} = 0$ . However, it will become evident during the discussion of the results that weak correlation effects are still introduced into the bath due to the coupling to the correlated impurities.

Additionally, a few important details have to be kept in mind. Although all calculations are formally performed at  $T = 0$ , a minor temperature scale is introduced into the calculations through the use of a small Gaussian smearing for the  $k$ -point integration. For this reason, all energetics are discussed in terms of the free energy  $F$ . In the case of the TIAM, introducing electronic correlations in the impurity orbitals only expectedly leads

to a charge transfer from the local orbitals into the bath, which is not desired here. As we are solely interested in the half-filled case of the two-impurity Anderson model within this work (to remain somewhat close to the canonical setup), we fix the occupation of the bath in all calculations, either by setting  $\epsilon_d = -U/2$ , or by introducing an additional Lagrange multiplier. Both approaches were checked to lead to the same results.

### 4.3 Hubbard bilayer model

The Hubbard bilayer is a canonical model which has, bar the influence of the DM interaction, already been studied in a multitude of works [83, 84, 85, 86, 13, 87, 88, 55]. While most studies focus on the influence of the ratio  $t/t_\perp$  on the electronic phase diagram, our goal will be to investigate the interplay of the electronic correlations with the Dzyaloshinskii-Moriya interaction. We will restrict our discussion to cases where  $t/t_\perp < 1$ , i.e. the coupling between the sites within a plane is stronger than the inter-plane hopping. Each layer has standard square-lattice dispersion with a bandwidth  $W = 8t$  and we will handle all energies throughout this section in units of the half bandwidth  $4t$ .

As our unit of repetition is the two site cluster with each site belonging to one of the two layers (Fig. 4.2) it should be made clear that only long-range ordered states originating from such a unit cell are accessible within our study. Our setup is not able to account for long-wavelength behaviour, e.g. spin spirals, which is something that might be addressed in a future study. Here, we will rather focus on the interplay of the fundamental short-range processes eventually driving the long-range ordered state in the strongly correlated metallic regime.

#### 4.3.1 Half-filled Hubbard bilayer

At half filling, the system contains one electron per layer site and is therefore susceptible to a Mott transition. Within this section, we will concentrate on the influence of the DM interaction on its onset and the behaviour in presence of strong correlations. To account for the inter-layer hopping  $t_\perp$  we will deal with two cases, one with weakly coupled layers ( $t_\perp = 0.025$ ) and one corresponding to somewhat stronger coupling ( $t_\perp = 0.1$ ).

Figure 4.3 summarizes the general behaviour of the Hubbard bilayer with increasing Hubbard  $U$ . Generally, we are able to stabilize two distinct metallic phases, the paramagnetic phase in the lower  $U$  region (PM) and the antiferromagnetic (AFM) phase closer to the Mott transition. Note that in concurrence with the previous discussion of the eventual emerging long-range order within our modeling the antiferromagnetism

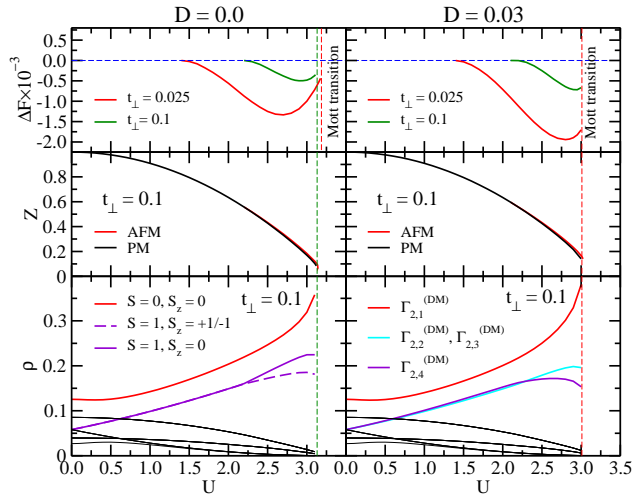


FIGURE 4.3: Free energy, quasiparticle weight and multiplet weight behaviour with increasing  $U$  for the half-filled Hubbard bilayer, shown for two different values of  $t_{\perp}$  and  $D$ , respectively. The top panel shows the free energy *differences* with respect to the PM phase. The states shown in color in the bottom panel belong to the two-particle sector, with others shown in black in the background.

here is of A-type character, i.e. it corresponds to two *ferromagnetic* layers coupled antiferromagnetically to each other. Some additional discussion of eventual intra-layer antiferromagnetic behaviour will be given at the end of this chapter.

The results for  $D = 0$ , i.e. the standard Hubbard bilayer without Dzyaloshinskii-Moriya interaction, are shown on the left. The top panel holds the free energy differences with respect to the paramagnetic phase. It can be clearly seen that the AFM phase wins over the paramagnetic phase in the high- $U$  region, with the onset of antiferromagnetic order hastened by a lower  $t_{\perp}$ , and hence a lower bonding-antibonding splitting. This is in line with previous results obtained with dynamical mean-field theory employing quantum Monte Carlo solvers for the impurity problem [86, 88]. Furthermore, there is a somewhat smaller difference in the critical values  $U_c$  needed to enter the insulating regime. The middle panel on the left-hand side holds the quasiparticle weights  $Z = (1 - \partial\Sigma/\partial\omega)^{-1}|_{\omega=0}$  for the  $t_{\perp} = 0.1$  case. The onset of the AFM state does not significantly influence the values here, with the AFM QP weights being only marginally larger right before the Mott insulator onset.

The respective panels on the right side hold the corresponding data in presence of the DM interaction with  $D = 0.03$ . The energetics plot in the top panel reveals no significant change in the  $U$  values responsible for the onset of the AFM phase, although the energy gain in the AFM state is larger and the difference between the two critical  $U_c$  for the two different values of  $t_{\perp}$  vanishes with  $D$ . The quasiparticle weights also do not exhibit strong changes with the introduced Dzyaloshinskii-Moriya interaction.

Our access to the local multiplet behaviour allows us to gain some insight into the

State Nr.	$S$	$S_z$	State composition	Energy
1	1	-1	$ 0 \downarrow, 0 \downarrow\rangle$	0
2	1	0	$ 0 \downarrow, \uparrow 0\rangle +  \uparrow 0, 0 \downarrow\rangle$	0
3	1	1	$ \uparrow 0, \uparrow 0\rangle$	0
4	0	0	$ 00, \uparrow \downarrow\rangle -  \uparrow \downarrow, 00\rangle$	U
5	0	0	$ \uparrow \downarrow, 00\rangle + \frac{U + \sqrt{U^2 + 16V^2}}{4V}  0 \downarrow, \uparrow 0\rangle -$ $- \frac{U + \sqrt{U^2 + 16V^2}}{4V}  \uparrow 0, 0 \downarrow\rangle +  00, \uparrow \downarrow\rangle$	$\frac{1}{2} [U - \sqrt{U^2 + 16V^2}]$
6	0	0	$ \uparrow \downarrow, 00\rangle + \frac{U - \sqrt{U^2 + 16V^2}}{4V}  0 \downarrow, \uparrow 0\rangle -$ $- \frac{U - \sqrt{U^2 + 16V^2}}{4V}  \uparrow 0, 0 \downarrow\rangle +  00, \uparrow \downarrow\rangle$	$\frac{1}{2} [U + \sqrt{U^2 + 16V^2}]$

TABLE 4.1: Two-particle eigenstates of the local dimer with corresponding  $S$  and  $S_z$  quantum numbers and energies. The state 5 is the ground state of the system. The states are not normalized, for clarity of appearance.

changes introduced by the anisotropic exchange by considering the respective weights of the various multiplets  $\Gamma_p$  in the particle sector  $p$ , where we here focus on the two-particle states as the most important for the half-filled system. The two-particle eigenstates of the local dimer are shown in Tab. 4.1, also compare Ref. [95]. In absence of DM interaction they can be classified according to the  $SU(2)$  symmetry and form triplet and singlet states in the two-particle sector. The weight (occupation probability)  $\rho_{\Gamma_p}$  of these multiplets in the strongly correlated itinerant system is accessible via  $\rho_{\Gamma_p} = \sum_{\Gamma'_p} |\phi_{\Gamma_p \Gamma'_p}|^2$ . Here  $\phi_{\Gamma_p \Gamma'_p}$  denotes the slave-boson amplitude connecting  $\Gamma_p$  and  $\Gamma'_p$  in the associated local multiplet basis, obtained from a rotation of the original  $\{\phi_{A_n}\}$ .

The multiplet weights are shown in the bottom panel of Fig. 4.3, with the, evidently most important, two-particle states highlighted in color. On the left hand side, in absence of the DM interaction, the individual multiplets are denoted according to their spin operator eigenvalues. The highest overall weight belongs, unsurprisingly, to the  $S = 0, S_z = 0$  singlet and shows a sharp increase with increasing U, followed by the triplet states. The degeneracy of the triplet is lifted at the onset of the AFM regime, lending more weight to the  $S_z = 0$  state. The contributions from the other particle sectors, shown in the background, are significantly lower in value to begin with and display a steady decrease towards the onset of the Mott transition.

For  $D \neq 0$ , the bilayer Hamiltonian Eq. (4.1) no longer commutes with  $\{S^2, S_z\}$ , and thus the corresponding states can no longer be classified according to these respective quantum numbers. This can be understood from the DM interaction favoring perpendicular alignment, thus disrupting the collinear setup and the notion of a defined spin quantization axis. The respective multiplet weights are shown in the right hand bottom

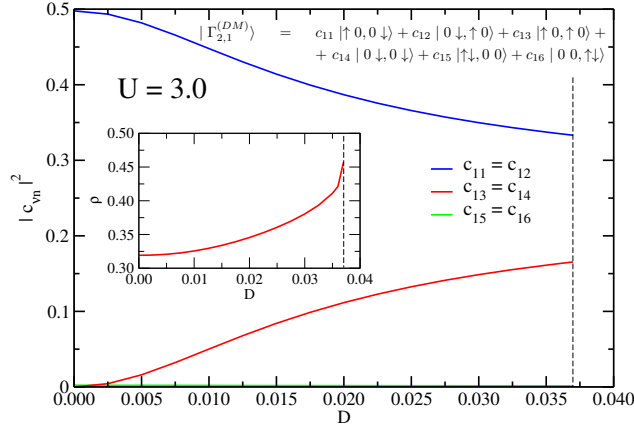


FIGURE 4.4: Hubbard bilayer: Fock state contributions to the state with the highest multiplet weight (see Fig. 4.3) as functions of  $D$ , calculated for  $U = 3$ . For  $D \neq 0$  this multiplet is no longer an eigenstate of the  $S^2$  or the  $S_z$  operator. The inset shows the evolution of the multiplet weight itself, with the data of Fig. 4.3 corresponding to  $D = 0.03$ .

panel. The overall picture still formally looks very familiar, with the clearly dominating highest multiplet and three somewhat lower entries. Note however that in presence of the DM interaction the three former triplet states are nondegenerate from the beginning, with  $(\Gamma_{2,4}^{DM})$  sporting a weight slightly different from the other two. This difference is enhanced at the onset of the AFM regime, where the doubly degenerate  $\Gamma_{2,2}^{DM}/\Gamma_{2,3}^{DM}$  state acquires a higher overall weight. This is manifestly different from the  $D = 0$  case where the doubly degenerate state holds the lowest value.

As it is clear that the  $S = 0, S_z = 0$  multiplet plays a dominant role in the local picture it is worth investigating its nature in some more detail. The new eigenstates of the system under influence of the Dzyaloshinskii-Moriya interaction,  $|\Gamma_{p,\nu}^{(DM)}\rangle$ , are still given by a general expansion into Fock states  $|n_p\rangle$  through  $|\Gamma_{p,\nu}^{(DM)}\rangle = \sum_n c_{\nu n}^{(p)} |n_p\rangle$ . The development of the six individual coefficients  $c_{1n}^{(2)}$  for the highest-weight state of the two particle sector with increasing  $D$  is shown in Fig. 4.4. At  $D = 0$ , the state is a  $S = 0, S_z = 0$  singlet, where the  $c_{11}, c_{12}$  coefficients (corresponding to antiferromagnetic  $|\uparrow 0, 0 \downarrow\rangle, |0 \downarrow, \uparrow 0\rangle$  Fock states) carry nearly all of the state, with a negligibly small contribution of  $c_{15}, c_{16}$ , while both  $c_{13}$  and  $c_{14}$  are exactly zero. As soon as a finite Dzyaloshinskii-Moriya interaction is turned on all coefficients  $c_{1n}^{(2)}$  become finite, with an ever increasing admixture of the ferromagnetic  $|\uparrow 0, \uparrow 0\rangle, |0 \downarrow, 0 \downarrow\rangle$  Fock states into the eigenstate.

Now that we have a general grip on the energetics and the local multiplet setup within the bilayer system we will go on to discuss the magnetic properties of the AFM state and its evolution in presence of a nonzero  $D$ . It is, after all, in the magnetically ordered states where we would expect anisotropic exchange contributions to have the most profound impact. Figure 4.5 shows the behaviour of the local spin moments within the AFM state with increasing  $U$ . The results for  $D = 0$  are shown in the left panel. The

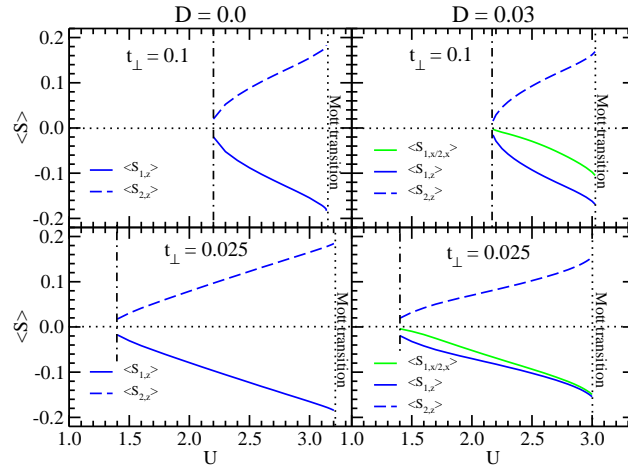


FIGURE 4.5: Spin expectation values in the AFM state. Finite DM coupling introduces a nonzero  $S_x$  component (the direction is due to our choice of the  $D$  vector). Vertical dot lines mark the Mott transitions, vertical dot-dashed lines mark the onset of AFM order.

onset of the AFM phase introduces a nonzero value of the  $\langle S_z \rangle$  spin component which then continues to grow with increasing  $U$ . The AFM order stabilizes at higher  $U$  values for larger  $t_\perp$ , which is then compensated by a steeper increase in local moment value. The right panel shows results for  $D = 0.03$ . Immediately at the onset of the AFM phase, a finite  $\langle S_x \rangle$  component appears, corresponding to a local spin configuration with both local moments slightly canted towards the x direction, thus introducing weak ferromagnetism into the previously purely antiferromagnetic system. The additional  $\langle S_x \rangle$  spin component continues to grow with increasing  $U$ , tilting both spins further towards each other as correlation strength increases. For  $t_\perp = 0.1$   $\langle S_x \rangle$  amounts to approximately half of the value of  $\langle S_z \rangle$  at the onset of the Mott transition. This effect is even more pronounced in the case of  $t_\perp = 0.025$  where the value of  $\langle S_x \rangle$  equals that of  $\langle S_z \rangle$  at  $U = U_c$ , corresponding to a canting angle of  $\gamma \sim 90^\circ$ .

The DM interaction does not only modify the antiferromagnetic ordered state but has an influence on the magnetic behaviour of the paramagnetic state as well. Figure 4.6 shows the spin-spin correlation functions between the two layers, both within the AFM and the PM states (the paramagnetic state can still be stabilized within the AFM region for comparison purposes, although it is no longer the ground state of the system). Results for  $D = 0$  are again shown in the left panel. For the paramagnetic state, the spin-spin correlation functions are naturally isotropic, corresponding to the full rotational invariance of the problem. The correlation function values stay in the negative throughout the whole range of  $U$ , demonstrating the overall tendency of the model towards antiferromagnetism and gaining in strength as the system approaches the Mott transition. At the onset of the AFM phase, the correlations along the magnetization direction become significantly enhanced in comparison to their PM state value, while the

other two spatial components suffer a reduction in strength. The overall phenomenology is similar for both  $t_{\perp} = 0.1$  and  $t_{\perp} = 0.025$ , with earlier onset but lower correlation strength for the weakly coupled bilayer and vice versa, which agrees with our results regarding long range magnetic order discussed above.

A finite DM interaction naturally introduces a strong spin-spin correlation anisotropy. Results for  $D = 0.03$  are shown in the right panel of Fig. 4.6. The full rotational symmetry of the PM state is replaced by rotational symmetry in the xz-plane only in presence of a nonzero  $\mathbf{D} = D\mathbf{e}_y$ . With this the  $\langle S_{1,y}S_{2,y} \rangle$  becomes enhanced, resulting in a stronger antiferromagnetic response along this direction. This effect, although weak, sets in already well before the AFM parameter range is reached, and becomes strongly enhanced in the AFM regime, even when the system is considered in the paramagnetic state. As the AFM state itself introduces a net magnetisation in the z direction (with a DM-originated canting towards x), all the individual spin-spin correlation function components become different in value, with a particularly strong antiferromagnetic response along the z axis and a significantly weakened antiferromagnetism along y. A lower value of  $t_{\perp}$ , as shown in the bottom panel, once again seems to strengthen the noncollinear tendencies, to the point where the  $\langle S_{1,x}S_{2,x} \rangle$  correlation function becomes particularly disconnected from the other components, even adopting a significant *ferromagnetic* response at higher U values.

So far, it has become evident that the anisotropic effects of the Dzyaloshinskii-Moriya interaction become significantly enhanced when strong electronic correlations are present within the system. To complete our investigation of the half-filled Hubbard bilayer we would like to more accurately assess how exactly the different phenomena discussed so far evolve from the collinear case. To this end, we will consider a strongly correlated Hubbard bilayer in the antiferromagnetic state, only slightly below the Mott transition, into which Dzyaloshinskii-Moriya interactions are gradually introduced. The results of this calculation are shown in Fig. 4.7.

The top panel displays the dependence of the quasiparticle weight  $Z$  on the value of  $D$ , calculated for two fixed correlation strengths  $U$ . As can be clearly seen, introducing the DM interaction into the system reduces the quasiparticle weight, to the point where the system can be forced to undergo a Dzyaloshinskii-Moriya driven metal-to-insulator transition at sufficiently high values. Note that this effect can be understood from the form of the DM operator in second quantization, in which it consists of a total of four creation/annihilation operators (two for each spin operator involved) and thus can be considered to represent a special form of particle-particle correlator. As such, it enhances the correlations within the system.

The lower panel contains information about the spin moments and spin-spin correlation functions as a function of  $D$ . As expected, DM interaction again forces the individual

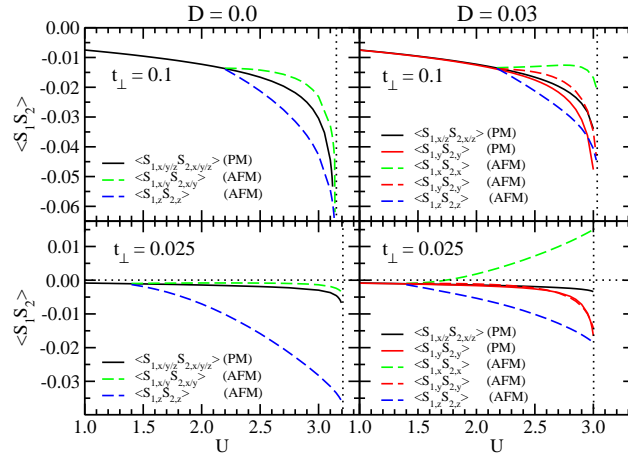


FIGURE 4.6: Spin-spin correlation functions between the layers. Solid lines correspond to PM phase, dashed lines to AFM phase.

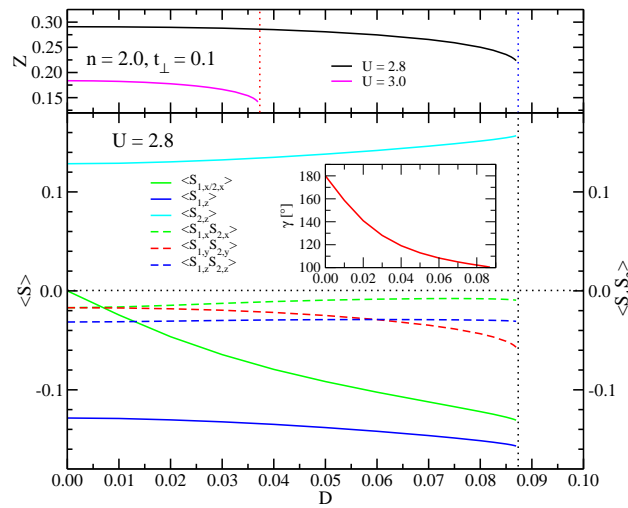


FIGURE 4.7: Evolution of the QP weights, local spin moments and spin-spin correlation functions with  $D$  for the AFM half-filled bilayer model for  $t_{\perp} = 0.1$ . Inset: Angle between the spin moments of the two layers as a function of  $D$ .

spin moments to tilt towards each other, with the value of the ferromagnetic contribution  $S_x$  depending strongly on  $D$ . The evolution of the angle between the spins is shown explicitly in the inset for clarity, where the value  $\gamma \sim 100^\circ$  is adopted close to the Mott transition, which is close to the DM ideal of  $90^\circ$ . Furthermore, spin-spin correlation functions along the  $y$  direction are shown to increase in strength with increasing  $D$ , while the antiferromagnetic response along the  $x$  axis is weakened. This is consistent with our earlier findings.

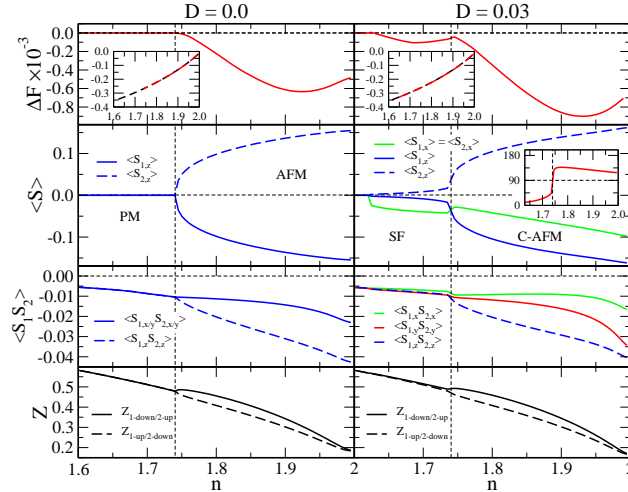


FIGURE 4.8: Effects of hole doping in the Hubbard bilayer model with  $t_{\perp} = 0.1$  and  $U = 3$ , with and without DM interaction. The insets in the top panel show the whole free energy curve, with the regions where long range magnetic order is stable marked in red. The top panel itself shows the difference with respect to the PM free energy. The right middle inset shows the evolution of the angle  $\gamma$  between the spins. Abbreviations: Canted anti-ferromagnetic phase (C-AFM), spin-flop phase (SF).

### 4.3.2 Hole-doped Hubbard bilayer

Now that we have gained some insight into the behaviour of the half-filled Hubbard bilayer with DM interaction we would like to assess the influence of hole-doping our model away from half filling, also to make a connection with the doped cuprate systems briefly discussed in the introduction. To this end, we start from the half-filled bilayer setup with  $U = 3$  and  $t_{\perp} = 0.1$ . As can be seen from Fig. 4.3, this set of parameters puts the system into the strongly correlated regime, just below the Mott transition and with a quasiparticle weight of only  $Z \sim 0.2$ .

The results of hole doping the system in the range  $1.6 < n < 2.0$  are summarized in Fig. 4.8. We will first briefly discuss the  $D = 0$  case, shown on the left. The top panel again displays the free energy difference with respect to the PM state, with the inset showing the whole free energy curve. Antiferromagnetic long range order can be seen to exist down to  $n = 1.74$ , with the corresponding local spin moments shown in the second panel. The order parameter of the AFM phase,  $\langle S_z \rangle$ , decreases steadily when moving away from  $n = 2$ . At the same time, antiferromagnetic spin-spin correlations become weaker and the quasiparticle weight increases significantly, readily displaying the half filled case as both the most strongly correlated and exhibiting the strongest antiferromagnetic tendencies.

As much as such a result can be expected from the doped bilayer model on general grounds, the situation becomes much more intriguing with the introduction of the Dzyaloshinskii-Moriya interaction. The former antiferromagnetic phase is now canted

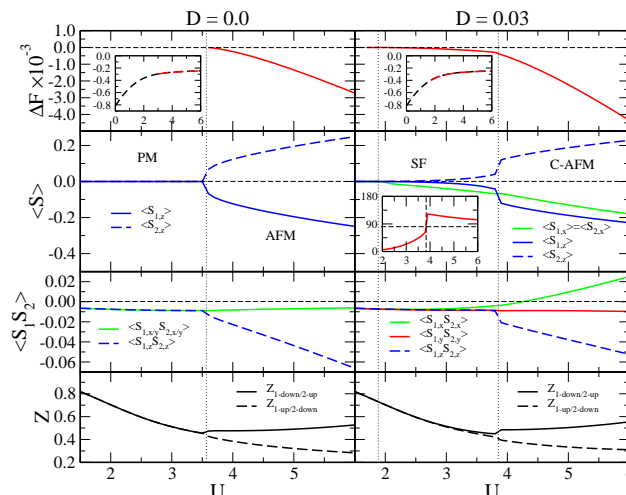


FIGURE 4.9: Interaction dependence of the hole doped Hubbard bilayer model at  $n = 1.7$ . Insets show free energy curves (top panel) and the spin-spin angle  $\gamma$ .

in the  $x$  direction (and hence designated C-AFM from here on) at half-filling, as can be expected from our previous discussion. The spin angle amounts to only slightly more than  $90^\circ$  showing the strong influence of the DM interaction in this regime. As the local moments become reduced away from half-filling the canting also lessens, until at  $n = 1.76$  the system suddenly undergoes a first order transition towards a novel metallic spin-flop (SF) phase. This transition is characterized by a discontinuous jump into a local configuration with the  $\langle S_x \rangle$  expectation value being actually *larger* than  $\langle S_z \rangle$ . This corresponds to an angle  $\gamma$  between the local spins being lower than  $90^\circ$ , which can be seen in the inset of the second right panel along with the sharp discontinuous jump at the transition point. The SF phase thus effectively exhibits dominant *ferromagnetic* behaviour with a weak antiferromagnetic canting, which is highly nontrivial. Note that neither the spin-spin correlation functions nor the quasiparticle weight show any kind of strong signature, and that the energy gain with respect to the paramagnetic phase is comparatively small. The SF phase vanishes below  $n \sim 1.62$  where the usual PM phase sets in.

In addition to the doping scan, a  $U$  scan of the doped Hubbard bilayer at  $n = 1.7$  and  $t_\perp = 0.1$  is shown in Fig. 4.9. The left hand side again displays the model behaviour sans the DM interaction. At  $n = 1.7$  the onset of antiferromagnetic order is delayed until  $U > 3.58$ , which is significantly higher than the critical interaction strength needed for the metal-insulator transition at half filling (see Fig. 4.3), while the usual PM phase is stable at lower  $U$  values.

In presence of the Dzyaloshinskii-Moriya interaction ( $D = 0.03$ ) the aforementioned SF phase is again stabilized for  $1.9 < U < 3.85$  with the jump in the spin-spin angle  $\gamma$  shown in the right middle inset. In addition to that the transition is accompanied by a

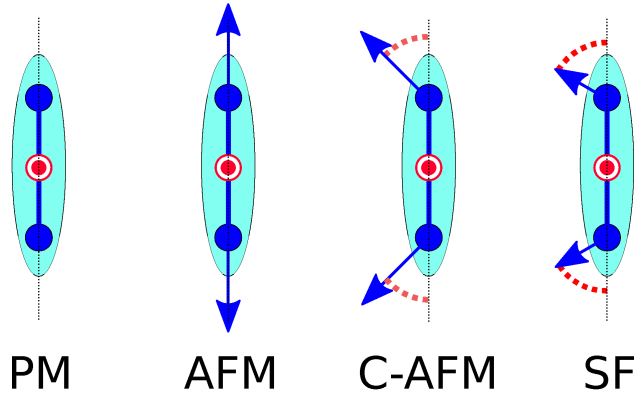


FIGURE 4.10: Illustration of the four different local spin configurations found to exist within the Hubbard bilayer model in the parameter space discussed within this work. (a) PM configuration without ordered local moments. (b) AFM configuration, corresponding to spin angle  $\gamma = 180^\circ$ . (c) C-AFM configuration,  $90^\circ < \gamma < 180^\circ$ . (d) SF configuration,  $\gamma < 90^\circ$

small discontinuity in the  $\langle S_{1,z} S_{2,z} \rangle$  correlation function, an effect not readily visible in the previous figure. Note that the presence of the spin-flop phase shifts the onset of the (C-)AFM phase towards somewhat higher  $U$  values. In contrast, there is no DM-related shift in the onset of the C-AFM phase with respect to doping, as can be seen from the previous discussion.

As such, our discussion of the doped Hubbard bilayer model reveals the existence of a novel spin-flop phase at the boundary between the usual AFM and PM phases, stabilized by a finite Dzyaloshinskii-Moriya interaction. As such, the model is found to exhibit four different local spin configurations over the discussed parameter range, summarized in Fig. 4.10. Note that the SF phase extends into the previously paramagnetic region of the phase diagram, and thus effectively increases the parameter range in which the system is susceptible to long range magnetic order.

#### 4.4 Two-impurity Anderson model.

The two-impurity Anderson model (TIAM) [89, 90, 91, 92, 93, 94, 95] is one of the canonical models in the field of strong electronic correlations. The coupling of the impurities to the common bath allows the model to encompass both the single-impurity Kondo mechanism and the RKKY indirect impurity-impurity exchange and gives us the possibility to study the interplay of these interactions. Note that in some works [84, 95] the two impurities of this model are connected to different baths, which results in the overall setup being similar in nature to the previously discussed bilayer geometry. This is not what we intend here. With the model Hamiltonian outlined in Eq. 4.2 we aim

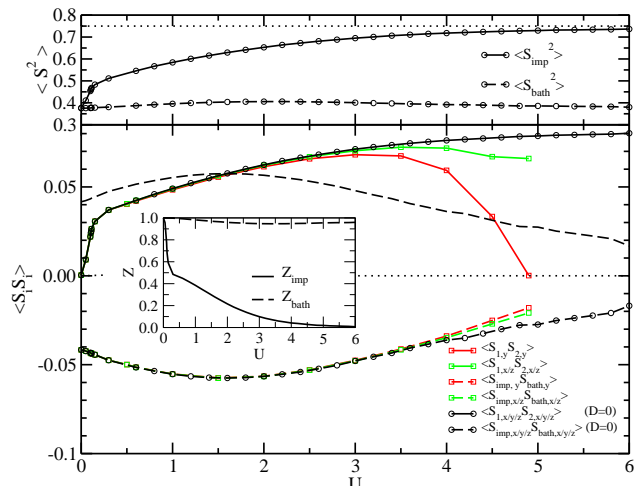


FIGURE 4.11: Spin correlation functions for the two-impurity Anderson model with  $t_{12} = 0$ . Top panel:  $\langle S^2 \rangle$  expectation values for  $D = 0$ . Curves for  $D \neq 0$  do not visibly differ. Bottom: Impurity-impurity and impurity-bath spin correlation functions, shown for  $D = 0$  (black, circles) and  $D = 0.05$  (color, squares). The dashed line in the top half of the bottom panel shows the  $\langle S_{imp} S_{bath} \rangle$  correlation function mirrored at the zero line, for the sake of comparison.

to fully incorporate the competition of the two aforementioned exchange mechanisms, additionally including the direct impurity-impurity exchange resulting from the explicit hopping  $t_{12}$  and, finally, the inter-impurity Dzyaloshinskii-Moriya interaction.

As can be seen from the Hamiltonian, the bath is treated explicitly within our model. We use a standard three-dimensional simple cubic dispersion with bandwidth  $W = 12t$  (setting  $t = 0.5$  in our calculations). For the direction of  $\mathbf{D}$  again the  $y$  axis is chosen. The impurity-bath hopping is set to  $V = -0.5$  for all calculations. The model is treated at half filling throughout the whole section.

Note that the model represents a system of finite size. As such, no long range magnetic order can be expected on general grounds and thus all discussions hereafter will deal exclusively with the paramagnetic state. However, due to the mean-field nature of the RISB formalism solutions with net local moments may still be stabilizable and thus these parameter regions must be handled with greater care.

To start our discussion with a comparatively simple setup, we begin by investigating the case where  $t_{12}$  is set to zero, i.e. there is no direct hopping between the individual impurities and all exchange mechanisms have to be mediated by the bath. Figure 4.11 shows the behaviour of the different spin-spin correlation functions, with and without Dzyaloshinskii-Moriya interaction active between the impurity sites. The top panel shows the evolution of the  $\langle S^2 \rangle = S(S + 1)$  expectation value with increasing interaction strength  $U$ . The fast increase in the  $\langle S_{imp}^2 \rangle$  signifies the quick formation of a local magnetic moment, driven by the onsite electronic correlations. At high interaction strength,  $\langle S_{imp}^2 \rangle$  saturates to  $\sim 0.75$ , which corresponds to the full  $S = 1/2$  limit. At the same

time the bath does not face local correlations by construction and thus  $\langle S_{bath}^2 \rangle$  remains mostly unperturbed.

This behaviour is largely mirrored by the individual quasiparticle weights  $Z$ , shown in the inset of the middle panel. The QP weight on the impurities drops sharply with the onset of a finite  $U$ , decreasing to almost zero at higher interaction strength. Additionally,  $Z_{bath}$  can also be seen to suffer a small decrease which is due to weak correlation effects being introduced by coupling to the strongly correlated impurities.

The spin-spin correlation functions themselves are shown in the middle panel. The correlation between a single impurity and the bath,  $\langle S_{imp} S_{bath} \rangle$  remains AFM in character throughout the whole  $U$  range, exhibiting a maximum at  $U_K \sim 1.6$ , a behaviour which can be readily explained by singlet-forming tendencies of the Kondo screening. On the other hand, the impurity-impurity spin correlations  $S_1 S_2$  are purely of FM kind and can be attributed to the local limit of the RKKY exchange between the impurities, mediated by the bath. The FM correlation strength rises quickly with the increase in  $U$ , exceeding the effect of the Kondo screening close to  $U_K$  (the dashed line in Fig. 4.11, representing the impurity-bath spin correlation function mirrored at the zero line, is shown for comparison). The system is then dominated by the FM RKKY interaction in the higher  $U$  region [90, 94, 95].

General understanding of this behaviour can be gained by considering a Schrieffer-Wolff [98] mapping for the Kondo coupling, which yields  $J_K = 8V^2/U$  for the exchange integral. If we treat the RKKY interaction as a second order process, i.e.  $J_{RKKY} \sim J_K^2$ , both exchange interactions become equivalent in strength for  $U = 2$  (remember that we use  $V = -0.5$  here), in line with the result obtained from our calculations. Accordingly, a higher impurity-bath hopping  $V$  causes the crossover region to shift to higher  $U$  values, since  $J_{RKKY}$  profits more strongly therefrom. Note that at the chosen parameter values ( $W = 6$ ) and in the considered interaction strength range our model is still far from the Kondo-Hamiltonian limit ( $U \gg W$ ) [92].

Introducing the inter-impurity Dzyaloshinskii-Moriya interaction with  $D = 0.05$  changes little at small interaction strengths  $U$ . In fact, the  $\langle S^2 \rangle$  expectation values, as shown in the top panel, remain nearly unperturbed over the entire scan region, as do the quasiparticle weights. For  $U \gtrsim 3$  however, the individual spin-spin correlation functions become significantly modified, with a particularly strong effect on the  $\langle S_{1,y} S_{2,y} \rangle$  inter-dimer component parallel to the direction of the Dzyaloshinskii-Moriya vector  $\mathbf{D}$ . As can be clearly seen, the reduction in ferromagnetic spin correlation strength due to local FM RKKY is extreme along the  $y$  direction, taking the correlation function down to approximately zero by  $U = 5$ . A similar, albeit much weaker reduction is visible in the other two inter-impurity spin correlation function components. At the same time, the antiferromagnetic impurity-bath correlations also become somewhat reduced, again with a stronger effect along the  $y$  direction.

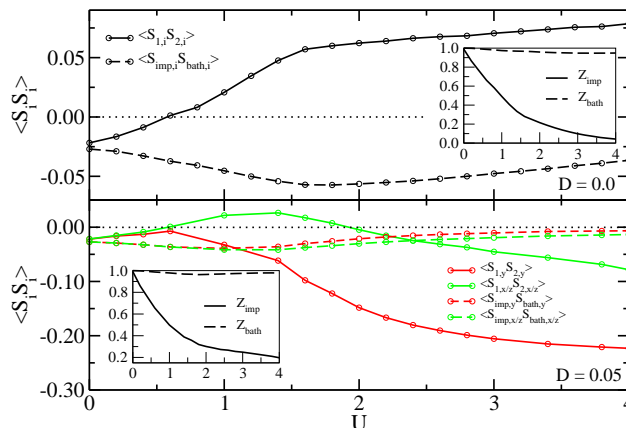


FIGURE 4.12: Spin-spin correlation functions for the two-impurity Anderson model with direct hopping  $t_{12} = 0.2$ , without (top) and with (bottom) DM interaction.

As such, a highly intriguing spin-spin interaction setup arises in presence of the Dzyaloshinskii-Moriya interaction in the large impurity  $U$  region, where the two local magnetic moments couple *ferromagnetically* along the  $x$  and  $z$  directions, yet exhibit a strong tendency towards *antiferromagnetic* coupling along the  $y$  axis. Note that we are still in the paramagnetic regime here.

Unfortunately, for  $U > 5$  and a nonzero DM interaction present in the model our mean-field based RISB approach encounters the very difficulty briefly described at the beginning of this section, namely that the paramagnetic solution is no longer stabilizable and net local moments start to appear on the impurity sites. As such, we cannot further investigate the  $U > 5$  region in this manner. A further study using a beyond-mean-field approach, as for example the numerical renormalization group [94], should prove highly interesting.

We complete our investigation of the two-impurity Anderson model by introducing an additional nonzero direct impurity-impurity hopping  $t_{12}$ . Figure 4.12 shows the spin-spin correlation functions and quasiparticle weights for  $t_{12} = 0.2$ , with and without DM interaction. The  $D = 0$  results are shown in the top panel. In presence of inter-impurity hopping the resulting direct exchange integral  $J_{dir} = 4t_{12}/U$  introduces additional antiferromagnetic correlations into the system. At  $U = 0$ , both  $\langle S_{imp} S_{bath} \rangle$  and  $\langle S_1 S_2 \rangle$  exhibit AFM coupling. With increasing  $U$  the correlation functions develop in a similar fashion as for the  $t_{12} = 0$  case, albeit with an overall reduction in magnitude at lower  $U$  values. The inter-impurity spin-spin correlation functions make the transition to FM coupling around  $U \sim 0.6$ .

The presence of direct exchange thus weakens both the impurity Kondo screening (due to stronger inter-impurity coupling) and the local FM RKKY interaction (as direct exchange favors AFM configurations). However, FM RKKY still dominates the system behaviour at sufficiently high  $U$  values, at least in the parameter region investigated

within this work. Note that the crossover into the RKKY-dominated regime still occurs at approximately the same point, despite the presence of direct exchange.

Finally, we introduce a finite Dzyaloshinskii-Moriya interaction with  $D = 0.05$ . At this point, *four* different exchange mechanisms (DM, RKKY, Kondo screening, direct exchange) compete within the model. The results are shown in the bottom panel of Fig. 4.12. Again, there is little modification of the correlation functions for low interaction strength. Already at around  $U \sim 0.6$  however the  $y$  component of the inter-impurity spin correlation function splits off, exhibiting strong antiferromagnetic tendencies at higher  $U$  values. This is mimicked by the  $\langle S_{1,x/z} S_{2,x/z} \rangle$  components, albeit to a lesser degree. Overall, the system behaviour in the strongly correlated region is severely changed by the presence of DM interaction. The previously established dominance of FM RKKY exchange is lost and the high  $U$  regime is instead ruled by antiferromagnetic spin correlations.

This so far concludes our discussion of the two-impurity Anderson model and the influence of the DM interaction therein.

## 4.5 Conclusions and outlook

We have conducted a thorough investigation on the effects of the Dzyaloshinskii-Moriya interaction in a strongly correlated metallic system. To this end, we investigated two canonical models, each aimed at capturing general characteristics of a class of materials where the DM interaction is thought to make an important contribution to the physical nature of the system. The Hubbard bilayer model is chosen to represent a bulk, layered environment, akin to the two-dimensional layered structure encountered e.g. in cuprate materials. The two-impurity Anderson model lends itself to a surface structure setup, where individual adatoms are additionally coupled to each other via indirect exchange through the substrate. Due to the particularly strongly reduced symmetry at the surface strong DM interactions may emerge which are believed to play an important role in the formation of complicated magnetic structures in adatom layers [68].

The Dzyaloshinskii-Moriya interaction is found to introduce strong modifications of system behaviour in both setups, in particular in the strongly correlated regime. The Hubbard bilayer system exhibits strong spin canting effects and modification of spin-spin correlation function behaviour. The noncollinearity in the local magnetic configurations introduced by the DM interaction becomes significantly *enhanced* by the strong electronic correlations. Additionally, the presence of Dzyaloshinskii-Moriya interaction hastens the onset of the Mott-insulating phase in thusly susceptible materials and effectively increases electronic correlation strength.

The hole-doped Hubbard bilayer with Dzyaloshinskii-Moriya interaction exhibits an intriguing spin-flop phase emerging at the boundary between the AFM and the PM phase away from half-filling. This novel phase is characterized by a strong spin canting, leading to local spin configurations with the angle between the individual spins being less than  $90^\circ$  and thus effectively producing a predominantly ferromagnetic spin ordering in an environment otherwise dominated by antiferromagnetic exchange. The SF phase extends into previously paramagnetic regions of the phase diagram, thus enabling long range order in parameter regions previously unsusceptible to it.

We expect these findings to be important for a variety of different materials. Strong out-of-axis spin components close to the Mott insulating regime can be expected to produce peculiar response patterns in applied magnetic field, which may be relevant for the behaviour of certain quasi-two-dimensional organic compounds [82]. On the other hand, hole-doped cuprate systems exhibit nonzero DM interactions brought about by minute structural distortions [76, 77, 78]. Some of these systems show intriguing magnetic spin-glass phases between the AFM phase and the superconducting region, which may be connected with the spin-flop behaviour brought about by the DM interaction in our model system [99].

Introducing the DM interaction into the two-impurity Anderson model heavily modifies the spin-spin correlations in the high  $U$  regime. The Dzyaloshinskii-Moriya interaction promotes singlet formation between the model impurities, working against the triplet-forming tendencies of FM RKKY in the local limit. This intriguing interplay may have profound influence on the behaviour of virtually any magnetic surface structure.

Incidentally, the discussion of the TIAM indicates the importance of eventually considering a beyond-mean-field approach which could improve upon the results discussed in this chapter. A proper treatment of the RKKY exchange beyond the local limit would also require the complete  $k$ -dependence of the impurity-bath coupling to be introduced into the model.

The models discussed in this work only strive to capture general aspects of the discussed realistic systems. Treatment of specific materials would generally require a more detailed approach, which is a possible avenue for future research. Also, more complicated realistic geometries may produce Dzyaloshinskii-Moriya configurations rather more involved than the relatively simple setup of the DM vector on each site pointing in the same direction. These, and also more involved magnetic orderings, i.e. spin spirals, would require larger local cluster setups and could consecutively lead to even more intriguing phenomenology.

In either case, the Dzyaloshinskii-Moriya interaction is found to emerge as an important player in the strongly correlated metallic regime. The DM-induced noncollinear behaviour becomes *heavily* enhanced in the high  $U$  regime, thus having the potential to make a significant impact in systems where it has been believed to be negligible before.

The findings discussed in this chapter have been published in [\[100\]](#).

## Chapter 5

# Adatoms on indium antimonide (110) surface

### 5.1 Motivation

The main motivation for the work presented in this chapter was the close collaboration between our group and A. A. Khajetoorians, J. Wiebe, B. Chilian and R. Wiesendanger, the results of which were ultimately published in [101]. The goal of our collaboration was to provide a method by which STM measurements of the magnetization of a single adatom on a semiconductor surface could be performed. To this end, a detailed understanding of the adatom system in question, namely Fe on InSb(110), had to be gained beforehand by means of DFT calculations, in particular with regard to geometry, density of states (related to the STM via the Tersoff-Hamann model [102]) and the behaviour of the local magnetic moment. To further understand the role of the magnetic impurity similar calculations were performed for Co and Ni adatoms on the same surface.

Magnetic impurities on semiconductor surfaces play a major role in the context of spintronic devices [103, 104, 105]. As such, these systems have already been subject to considerable attention in the past. Reconstruction behaviour of the clean surfaces has been studied extensively by Duke [106], while the role of point defects and vacancies in InP(110), InAs(110) and InSb(110) has been investigated by Höglund *et al.* [107] and Qian *et al.* [108]. Direct comparison between theory and STM results for the InAs(110) system has been done by Klijn [109], investigating the surface states and drawing connections to the measured STM topography via the Tersoff-Hamann model.

The same surface is found to exhibit a high spin polarization at the interface when covered with a monolayer of Fe, which at the same time nearly completely prevents any surface reconstruction [110]. The two-dimensional electron systems emerging at the

surface of such setups were studied by Masutomi [111] and Tsuji [112, 113] for InAs and InSb systems with a monolayer of Ag deposited on top. Concerning individual adatom structures, investigations of Fe adatoms and chains on InAs(110) were done by Matsui *et al.* [114], while substitutional Mn atoms in GaAs(110) were studied by Strandberg [115].

The research done in the past years underlines the necessity of a combined approach by theory and experiment alike to allow the individual techniques to compensate for each others' shortcomings and provide a comprehensive and thorough description of the system at hand.

As such, this chapter is organized as follows. In the first section, the methodology of our approach is briefly summarized and the surface relaxations, adatom positions and surface potentials are discussed. In the second part, bonding behaviour within the surface and the local adatom orbitals are treated. Finally, the last part of this chapter focuses on the vacuum density of states above the surface in the case of Fe/InSb(110). Save for the last part, all three (Fe,Co,Ni) /InSb(110) systems are treated on equal footing throughout this chapter.

## 5.2 Setup and geometry

For our initial investigation of magnetic adatoms on the InSb(110) surface we again rely on density functional theory, with the central goal to gain a proper understanding of system properties relevant in conjunction with the STM experimental approach. As such, the VASP [52] code was used exclusively for calculations featured in this chapter, with eventual additional many-body treatment relegated to further studies until a thorough understanding of the system behaviour on DFT level is achieved. Perspectives for such treatment and some relevant system properties will be discussed over the course of this work.

To appropriately model the InSb(110) surface we again resort to the slab geometry similar to the one already discussed in chapter 3. The utilized supercell is shown in Fig. 5.2, with the view onto the (110) surface from above (which would be, so to say, the 'STM perspective') shown on the left and the view parallel to the surface along the  $[1\bar{1}0]$  direction displayed on the right. The slab consists of five indium antimonide layers, with the bottom of the structure passivated by pseudohydrogen [116] to saturate dangling bonds. We use the GGA-PBE [7] exchange-correlation potential, with the Sb(5s,5p) and the In(4d,5s,5p) electrons treated as valence for the substrate. For all three individual adatoms (Fe, Co, Ni), the (3d,4s) potentials are used. These, and also the appropriate pseudohydrogen PAW potentials [117] for dealing with III-V semiconductor substrates are provided by the VASP potential library. All calculations were performed

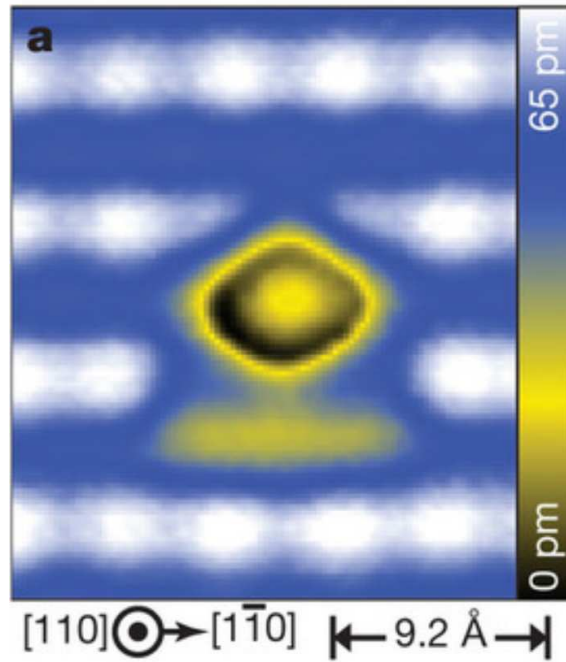


FIGURE 5.1: STM topograph image of a single Fe adatom on the InSb(110) surface. The light blue rows correspond to the Sb first layer atoms, with the Fe adatom highlighted in yellow. Image taken from Ref. [101].

on a  $7 \times 7 \times 1$  two-dimensional k-point mesh.

Fig. 5.2 visualizes the geometry of the surface, where a thorough relaxation procedure was performed for all atoms besides the lowest In/Sb layer. As already well known from both experiment [118, 119, 120, 121] and theory [122, 123, 124] the InSb(110) surface relaxes by moving the Sb atoms of the uppermost layer outwards while drawing the In atoms further inwards, while the lower-lying layers remain essentially bulk-like. When placed on the thus relaxed surface, all three adatom species come to rest inside the 'trench' formed by the (110) surface, with the two nearest neighbours along the  $[001]$  direction being In atoms. The other seemingly likely adatom position, with Sb nearest neighbours along  $[001]$ , can in principle be stabilized through careful relaxation, which indicates a local potential minimum there. Overall however, the first configuration is energetically more favorable for every adatom species, and especially so in the case of Fe where the energy difference amounts to  $\sim 2 \text{ eV}$  (while  $\Delta E \sim 0.3 \text{ eV}$  for both Co and Ni). This is in agreement with experimental findings by Khajetoorians *et al.* Though the lateral resolution of the STM topographic images is not fine enough to clearly determine the geometry, all individual Fe adatoms produce the same topography, strongly indicating that only one local configuration is actually assumed. The corresponding STM image of a single Fe adatom is shown in Fig 5.1.

The addition of the adatom onto the (110) surface introduces slight displacements of the neighbouring substrate atoms from their original positions, with a particularly

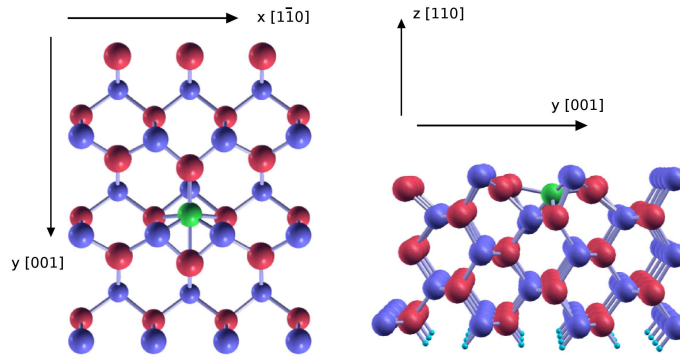


FIGURE 5.2: Geometry of the InSb(110) supercell- Left: Top view. Right: View along the  $[1\bar{1}0]$  direction. Sb atoms are shown in blue, In atoms in red, and pseudohydrogen in cyan. The adatom on top of the slab is displayed in light green.

Dist.[Å]:	y1	x2	y2	y3	z1	z2	z3	d1	d3
Fe	3.044	2.043	1.251	2.931	0.504	1.254	0.544	0.447	0.577
Co	2.631	2.01	0.925	3.942	0.3	1.423	0.476	0.409	0.06
Ni	2.669	2.067	0.992	4.03	0.414	1.373	0.434	0.407	0.094

TABLE 5.1: Certain characteristic distances of the different adatom setups on the InSb(110) surface. The nomenclature refers to Fig. 5.3.

prominent influence on the In nearest neighbours along  $[001]$ . The exact position of the adatom itself also varies depending on the adatom species. The corresponding values are shown in Table 5.1, with the numbering corresponding to the schematic representation of the surface layer displayed in Fig. 5.3. In direct comparison to the other two adatom species, the Fe adatom exhibits a much stronger influence on the In neighbour from the opposing In-Sb row, denoted as (3) in Fig. 5.3, with an equilibrium position much closer to it than the other two adatom species (compare the  $y1$  and  $y3$  values from Fig. 5.3). At the same time, the corresponding In surface atom is displaced further towards the Fe, while virtually no such influence is seen in case of the other two adatom species (see column d3). This is due to an additional bond forming between the In-(3) and the iron adatom, as will be discussed in the next section. This bond is not present in the other configurations.

To further corroborate these results and gain a somewhat more clear picture of the local potentials in which the respective adatoms are situated the energy cost of artificially displacing the adatom by  $0.3 \text{ \AA}$  along each inequivalent in-plane direction are shown in Tab. 5.2. The values are similar for all three adatom species, with the Co adatom seemingly situated in the steepest local potential minimum overall. The potential of the Fe

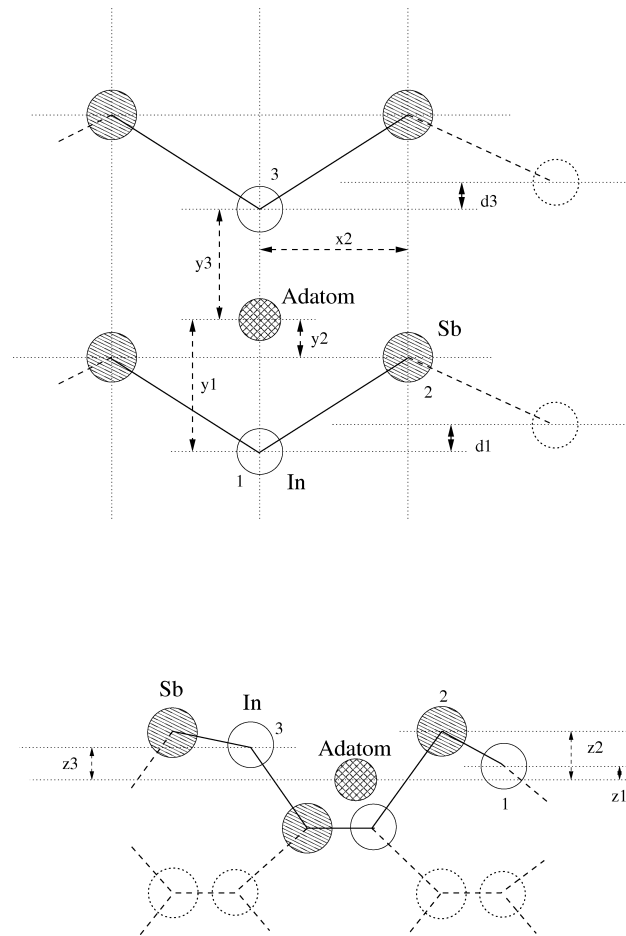


FIGURE 5.3: Schematic representation of the position of the (Fe,Co,Ni)-adatom and the displacements induced by its presence in the first layer of the InSb(110) substrate. Only the most prominent position changes are denoted, with the individual values listed in Tab. 5.1. Other neighbouring atoms are influenced to a lesser degree.

adatom system along the  $y$  direction is particularly flat, which is reasonable considering its position towards the middle of the surface 'trench' and the bonding towards both  $+$   $y$  and  $-y$  directions. Note that the displacement used here accounts for only about 10 percent of the nearest neighbour distance. If one wanted to use the data from Tab. 5.2 to estimate for example, vibrational energies, a harmonic approximation should still be valid.

### 5.3 Adatom orbitals and bonding behaviour.

As the different adatoms bring their respective number of valence electrons with them the local electronic configuration and the bonding of the adatom to the surface vary rather significantly. Regarding the local orbital occupation, it can be uniformly said that the adatom  $s$ -electrons become strongly delocalized due to the hybridization with

Dir. :	+ / - $x$	- $y$	+ $y$
Fe	+ 0.26 eV	+ 0.22 eV	+ 0.16 eV
Co	+ 0.33 eV	+ 0.31 eV	+ 0.34 eV
Ni	+ 0.21 eV	+ 0.26 eV	+ 0.24 eV

TABLE 5.2: Energy cost of displacing the individual adatoms along nonequivalent in-plane directions by 0.3 Å. The directions correspond to those in Fig. 5.2 (‘+ y’ points along the y direction marked therein, i.e. down).

the surface. On the other hand, the d-orbital accepts additional charge from the surface, the overall transfer amounting to roughly  $4s^x \rightarrow 4s^{x-2}$  and  $3d^x \rightarrow 3d^{x+2}$ . This is true for all three different adatom species and results in a net adatom magnetic moment for both Fe and Co, while the Ni system sports a full d-shell and thus is paramagnetic.

The density of states for all three system is shown in Figures 5.4 - 5.8. Fig. 5.4 displays the total density of states in comparison to the adatom d-shell density of states for the Fe adatom system. First of all, the above-mentioned local Fe moment is clearly visible in the two spin channels. For the spin-up component, local d orbitals lie nearly entirely below the Fermi level while the spin down orbitals are only partially occupied. The local magnetic moment of the Fe adatom, carried by the d-orbitals, amounts to approximately  $2.3\mu_B$ . This moment is partially compensated by small induced moments of opposite sign emerging on neighbouring substrate atoms, with the resulting total unit cell moment of  $2.0\mu_B$ , an effect which we will discuss in some more detail later.

From the bottom panel, the majority spin channel DOS around the Fermi level is mostly contributed by the d orbitals, with the difference in magnitude mostly originating from the orbital lobes reaching out of the nonoverlapping spheres within which the orbital contributions are calculated. The spin-up channel however, exhibits a set of unoccupied states just above the Fermi level which do not seem to stem from the local Fe-d states, nor can they be explicitly attributed to the local states of any of the neighbouring atoms. These states play an important role with regard to the STM measurements and will be discussed at the end of this chapter.

Figure 5.5 shows the angular momentum resolved DOS for the Fe d-states for the spin-down channel in terms of cubic harmonics. Since the d-states of the other spin channel are fully occupied we may thus check which of the five d orbitals carry the local moment. Evidently, the  $d_{yz}$ ,  $d_{x^2-y^2}$  and  $d_{xz}$  states are, for the most part occupied, leaving the  $d_{xy}$  and the  $d_{z^2}$  states responsible for the magnetic behaviour. This may be further checked by plotting the onsite density matrix for the d-states, shown in Tab. 5.3. The spin down states can be seen to sport an overall somewhat smaller occupation compared to their spin up counterparts, with the majority of the moment carried by the two previously

Fe ( $\uparrow$ ):	$d_{xy}$	$d_{yz}$	$d_{z^2}$	$d_{xz}$	$d_{x^2-y^2}$
$d_1$	0.8994	0.0000	0.0000	-0.0135	0.0000
$d_2$	0.0000	0.8317	-0.0196	0.0000	0.0000
$d_3$	0.0000	-0.0196	0.8975	0.0000	0.0106
$d_4$	-0.0135	0.0000	0.0000	0.8373	0.0000
$d_5$	0.0000	0.0000	0.0106	0.0000	0.8435
Fe ( $\downarrow$ ):	$d_{xy}$	$d_{yz}$	$d_{z^2}$	$d_{xz}$	$d_{x^2-y^2}$
$d_1$	0.1277	0.0000	0.0000	-0.0207	0.0000
$d_2$	0.0000	0.5704	0.0915	0.0000	-0.0358
$d_3$	0.0000	0.0915	0.0980	0.0000	-0.0332
$d_4$	-0.0207	0.0000	0.0000	0.6637	0.0000
$d_5$	0.0000	-0.0358	-0.0332	0.0000	0.5617

TABLE 5.3: Onsite density matrix of the Fe d states for the Fe/InSb(110) system, in terms of cubic harmonics. The  $d_{xy}$  and  $d_{z^2}$  states carry the local moment.

mentioned orbitals. Additionally, the onsite density matrix is in fact reasonably close to diagonal, meaning that the actual local system orbitals still well resemble the original cubic harmonics. This will be further visualized in the next section.

Similarly, the orbital resolved density of states and the local density matrix of the Co/InSb(110) system are shown in Figs. 5.6, 5.7 and Tab. 5.4, respectively. Again, the density of states plot shows the d orbitals of one spin channel (down) to be completely occupied, while some of the d-orbital related spin up states lie above the Fermi level. These are shown in Fig. 5.7 to nearly exclusively stem from the  $d_{xy}$  orbital, a result again underlined by the orbital density matrix values. The matrix is again found to be close to diagonal, however with somewhat larger off-diagonal elements when compared to the Fe case, especially between the  $d_{xy}$  and the  $d_{xz}$  orbitals.

Finally, the respective results for the Ni adatom system are shown in Fig. 5.8 and Tab. 5.5. For this adatom setup all Ni d orbitals lie below the Fermi level, again with a fairly diagonal orbital density matrix of the d states. This configuration results in no local magnetic moment at all; the system is paramagnetic.

The orbitals carrying the local moments for the two magnetic systems are of importance for the lateral distribution of the spin density. The  $d_{xy}$  orbital lies in the surface plane, thus contributing to a spread along the surface, while the  $d_{z^2}$  orbital reaches further outwards. We would thus expect the spin polarization along the z-direction to be more prominent in the Fe adatom system, which can be found visualized in the next

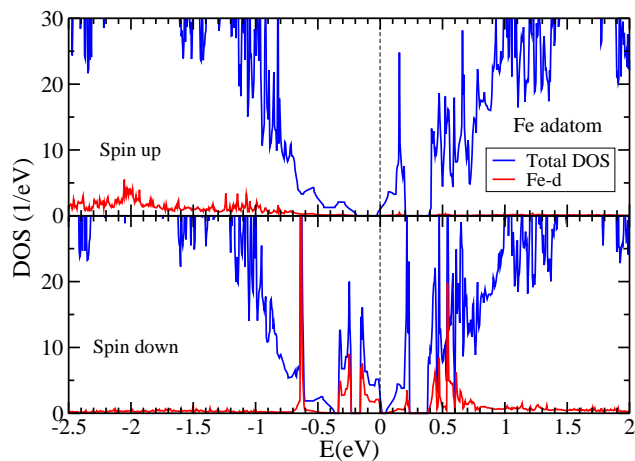


FIGURE 5.4: Total density of states (blue) and d-orbital density of states (red) for the Fe/InSb(110) system, shown for both spin channels.

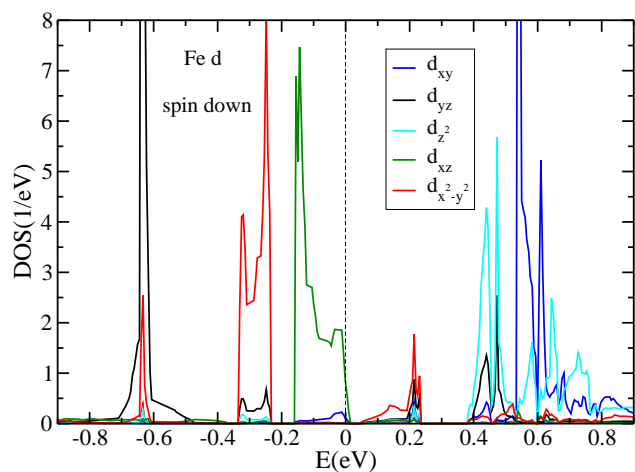


FIGURE 5.5: Angular momentum resolved density of states for the Fe-d orbitals, spin-down channel.

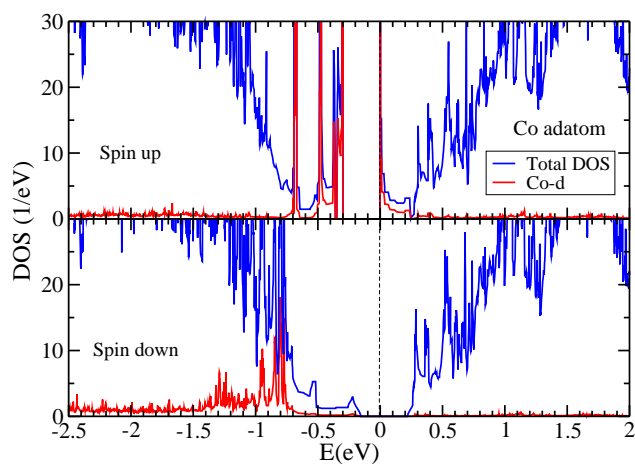


FIGURE 5.6: Total density of states (blue) and d-orbital density of states (red) for the Co/InSb(110) system. Compare Fig. 5.4.

Co ( $\uparrow$ ):	$d_{xy}$	$d_{yz}$	$d_{z^2}$	$d_{xz}$	$d_{x^2-y^2}$
$d_1$	0.3387	0.0000	0.0000	-0.0879	0.0000
$d_2$	0.0000	0.7146	-0.0082	0.0000	-0.0025
$d_3$	0.0000	-0.0082	0.7633	0.0000	0.0049
$d_4$	-0.0879	0.0000	0.0000	0.7110	0.0000
$d_5$	0.0000	-0.0025	0.0049	0.0000	0.7545
Co ( $\downarrow$ ):	$d_{xy}$	$d_{yz}$	$d_{z^2}$	$d_{xz}$	$d_{x^2-y^2}$
$d_1$	0.9099	0.0000	0.0000	-0.0071	0.0000
$d_2$	0.0000	0.8266	-0.0014	0.0000	0.0025
$d_3$	0.0000	-0.0014	0.8530	0.0000	-0.0037
$d_4$	-0.0071	0.0000	0.0000	0.7973	0.0000
$d_5$	0.0000	0.0025	-0.0037	0.0000	0.8176

TABLE 5.4: Onsite density matrix of the Co d states for the Co/InSb(110) system, in terms of cubic harmonics. The local moment originates from the  $d_{xy}$  orbital.

Ni :	$d_{xy}$	$d_{yz}$	$d_{z^2}$	$d_{xz}$	$d_{x^2-y^2}$
$d_1$	0.9016	0.0000	0.0000	-0.0181	0.0000
$d_2$	0.0000	0.8519	0.0012	0.0000	0.0106
$d_3$	0.0000	0.0012	0.8778	0.0000	-0.0030
$d_4$	-0.0181	0.0000	0.0000	0.8242	0.0000
$d_5$	0.0000	0.0106	-0.0030	0.0000	0.8170

TABLE 5.5: Onsite density matrix of the Co d states for the Ni/InSb(110) system, in terms of cubic harmonics. The system is paramagnetic.

section.

Finally, to make a connection with the local geometry discussions in the first part of this chapter and also to adopt a viewpoint with a closer relation to the STM experiments, we would like to gain an understanding of the charge distributions governing the behaviour of the surface. To this end, the bonding charge density, i.e. the total charge density minus the atomic charge density (summed over the spin channels), is shown in Figs. 5.9, 5.10 and 5.11 for all three adatom systems. Regions of positive charge density (red) indicate the formation of bonds between neighbouring atoms, while regions of negative density (blue) indicate charge loss, compared to the atomic distribution.

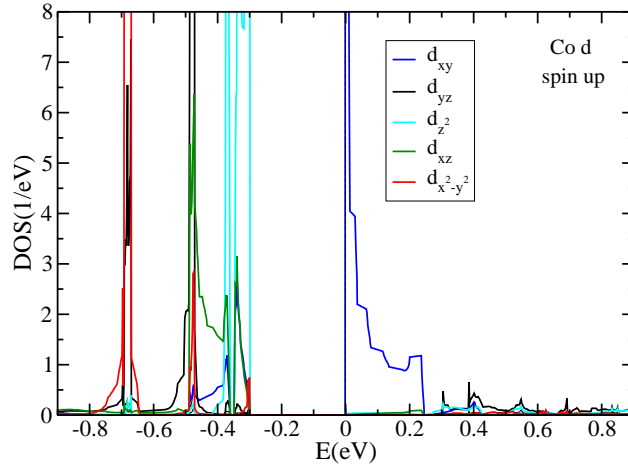


FIGURE 5.7: Same as Fig. 5.5, now for the Co/InSb(110) system, spin-up channel.

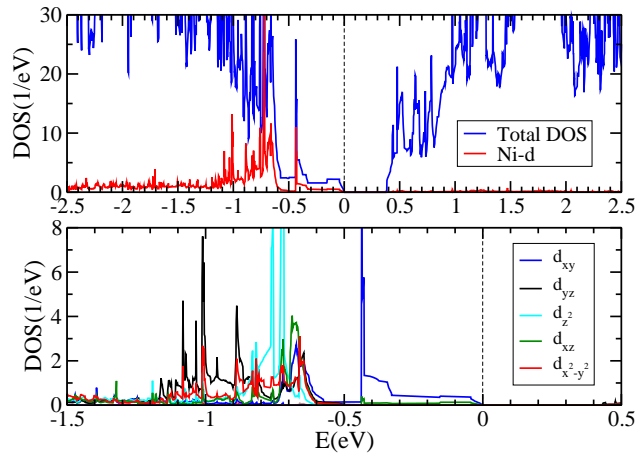


FIGURE 5.8: Top panel: Comparison between the total and the Ni-d density of states for the Ni/InSb(110) system. Bottom panel: Angular resolved plot of the Ni-d states. The system is paramagnetic.

The cut through the unit cell is made parallel to the (110) surface, approximately at the height of the uppermost In layer, i.e. *slightly above* the adatom position. The bonding charge density of the Fe/InSb(110) system is shown in Fig. 5.9. First of all, the bonds between the individual atoms of the surface feature as regions of increased charge density, situated between neighbouring atoms of both first and second layer (compare Fig. 5.2), while the adatom structure is featured in the middle. From the investigation of the local density of states, we already know that the  $d_{xy}$  and  $d_{z^2}$  orbitals of the Fe adatom are not fully occupied. This fact is now effectively visualized by the local bonding charge distribution. Compared to the spherical distribution of the individual atom, both above-mentioned orbitals are less occupied, and thus are indicated by regions of negative density. The lobes of the in-plane  $d_{xy}$  orbital, pointing along the diagonals, are clearly visible in the plot. Additionally, since the plane of the density plot lies above the

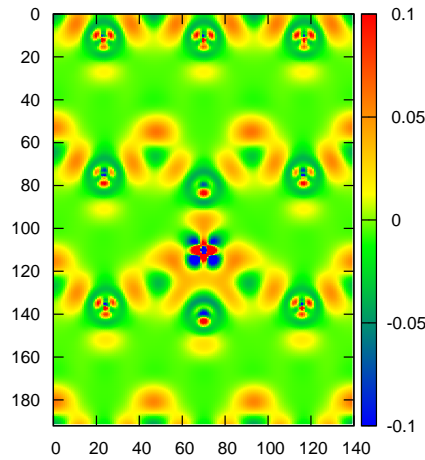


FIGURE 5.9: Bonding (total) charge density of the Fe/InSb(110) surface, in units of  $e/\text{\AA}^{-3}$ . The cut is made at the height of the uppermost In layer, i.e. slightly above the adatom. The four lobes of the in-plane Fe  $d_{xy}$  orbital are clearly visible in blue. The blue dot in the middle corresponds to a cross section of the upwards-pointing lobe of the  $d_{z^2}$  orbital.

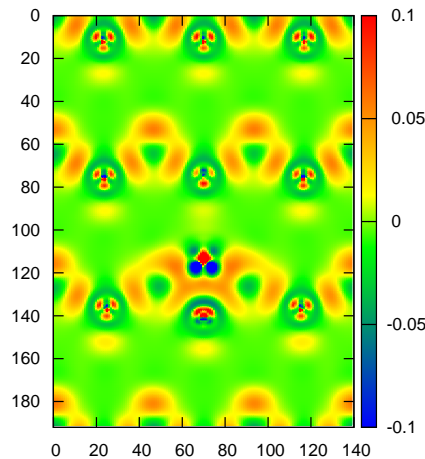


FIGURE 5.10: Same as Fig. 5.9, now for the Co/InSb(110) system. The  $d_{xy}$  orbital is still visible (somewhat canted along the  $y$  direction), though the  $d_{z^2}$  orbital no longer appears in blue due to additional filling. The cut is made at the same height as in Fig. 5.9, although the adatom lies lower than in the Fe case.

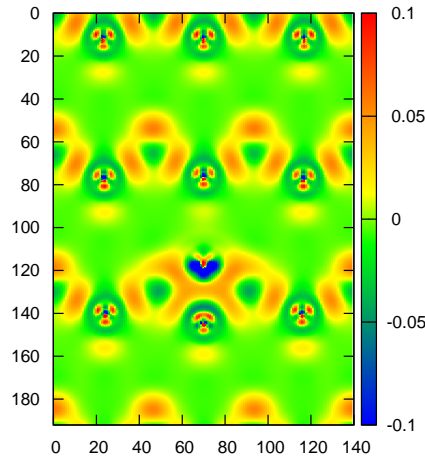


FIGURE 5.11: Same as Fig. 5.10, here for the Ni adatom system. The individual d orbitals are no longer well distinguishable.

adatom, the cross section of the  $d_{z^2}$  upwards-pointing lobe is also featured as a small region of negative charge density right in the middle of the adatom feature. Fig. 5.9 thus provides a rather nice visualization of the results from the local DOS discussion above.

Another feature of the Fe adatom system is the additional bond between the Fe atom and the In atom situated directly above it along the [001] direction. This bond, as will be seen below, is not present in the other adatom configurations and provides an explanation for the rather strong displacements of both the Fe and the In atoms along this direction, as already discussed at the beginning of this chapter.

Similar bonding charge density plots for the Co and Ni adatom systems are shown in Figs. 5.10 and 5.11, respectively. In the case of the Co adatom, the overall picture exhibits a few distinct differences. Since the  $d_{z^2}$  orbital sports a higher occupation in this setup its cross section is no longer visible as a region of negative density in the cut. Further, the  $d_{xy}$  orbital appears slightly canted towards the +y direction, which is readily visible from the slightly different intensities of the lobes and stems from the minute off-diagonal elements in the onsite density matrix. The additional adatom-In bond discussed above for the Fe adatom is no longer present here. Note that due to the different bonding character the adatom is situated somewhat lower inside the surface for this setup (compare Tab. 5.1).

Ni adatom system bonding charge density also does not exhibit the additional adatom-In bond. Further, due to the rather uniform occupation of the d-shell individual orbitals

Direction :	$[1\bar{1}0]$	$[001]$	$[110]$
Fe	preferred	+ 1.8 meV	+ 0.4 meV
Co	preferred	+ 0.5 meV	+ 0.2 meV

TABLE 5.6: Magnetic anisotropies of the Fe and Co adatom systems on InSb(110). The energy differences are given relative to the energy of the preferred orientation of the magnetic moment along the  $[1\bar{1}0]$  direction.

can no longer be distinguished here.

## 5.4 Magnetic anisotropies

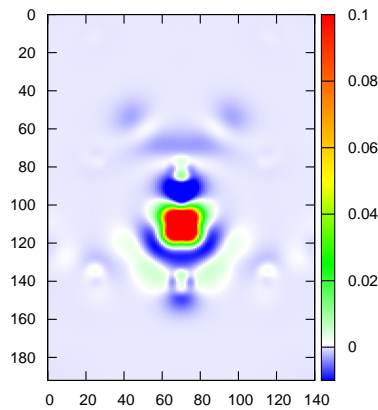


FIGURE 5.12: Spin density distribution in the Fe/InSb(110) system surface, in units of  $e/\text{\AA}^{-3}$ . The image plane lies at the level of the outmost In layer, approximately  $0.5 \text{\AA}$  above the adatom. The  $d_{xy}$  orbital carrying the local moment is readily visible.

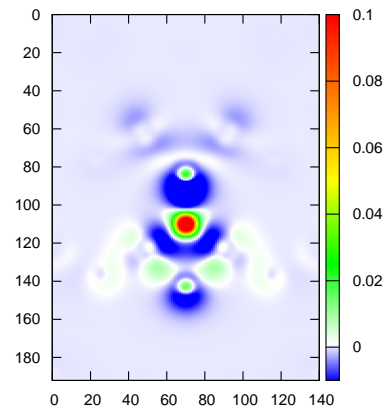


FIGURE 5.13: Same as left, now the image plane lies  $\sim 1 \text{\AA}$  above the adatom, directly above the outmost Sb layer. The  $d_{xy}$  orbital is now mostly below the image plane. The feature in the middle is a cut through the lobe of the  $d_{z^2}$  orbital.

Having already briefly touched the topic of magnetism in the previous sections, a somewhat more in depth discussion of the adatom magnetic behaviour seems in order. The lateral spin density distribution of the two magnetic systems is shown in Figs. 5.12 - 5.15, respectively, in units of  $e/\text{\AA}^{-3}$ . From the previous discussion, we know that the local magnetic moment of the Fe adatom is mostly carried by the in-plane  $d_{xy}$  and the vertical  $d_{z^2}$  orbitals. The image plane of Fig. 5.12 lies about  $0.5 \text{\AA}$  above the adatom,

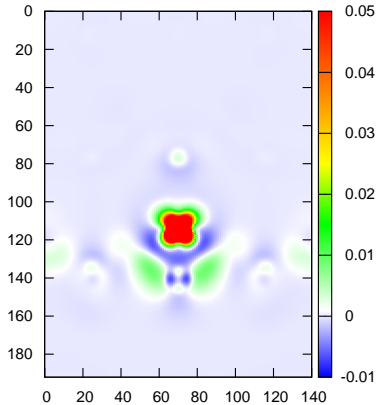


FIGURE 5.14: Same as Fig. 5.12, now for the Co adatom system. Note that significantly less compensating spin density is present when compared to the Fe adatom system.

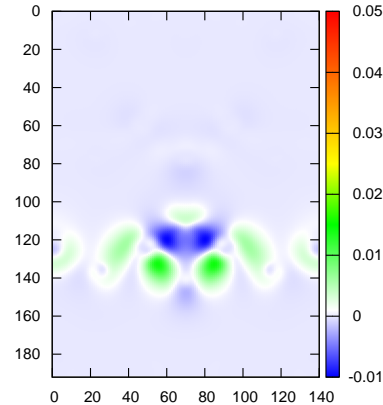


FIGURE 5.15: Co adatom system, approximately 1 Å above the adatom. Since the  $d_{z^2}$  carries no moment the spin density does not reach as far into the vacuum region.

close enough to provide a cut through the in-plane orbital. Fig. 5.13 shows the same setup  $\sim 1$  Å above the Fe atom: the characteristic lobes of the  $d_{xy}$  orbital are no longer visible and the  $d_{z^2}$  lobe is featured prominently instead, having a quite significant reach perpendicular to the surface.

It can be readily seen that most of the local moment is indeed concentrated on the orbitals in question. At the same time however, a substantial opposite spin density is induced in the surrounding volume, mostly in the regions between the adatom and the neighbouring In atoms along the [001] direction. This spin density partially compensates the local Fe moment: while the Fe d-orbitals carry a total magnetic moment of  $\sim 2.3\mu_B$  the total moment of the cell amounts to  $2\mu_B$  only, meaning that  $\sim 0.3\mu_B$  worth of opposite spin density is distributed in close proximity around the adatom.

Figures 5.14 and 5.15 show the Co adatom system in the same manner. While the cut 0.5 Å above the adatom appears similar to the Fe setup the spin density does not spread far into the vacuum region: already at the vertical distance of 1 Å no strong features appear. Additionally, significantly less spin the opposing sign is induced in this setup in comparison to the Fe adatom system. The local moment of the Co d orbitals amounts to  $\sim 0.92 \mu_B$  with a total unit cell moment of  $1 \mu_B$ , i.e. the net additional contributions from the surrounding atoms enhance the local moment instead of weakening it as in the case of Fe.

Finally, we performed calculations with included spin-orbit coupling to determine the anisotropies of the two magnetic systems. The results are summarized in Tab. 5.6,

where the energy differences are given with respect to the preferred magnetic configuration. For both systems the magnetization preferably points along the  $[1\bar{1}0]$  direction, i.e. in the surface plane, along the 'trench' direction. The direction perpendicular to the 'trenches' is energetically most unfavorable for both systems. These findings are of major importance in conjunction with the work published in [101].

## 5.5 Vacuum density of states

Finally, to further relate to the STM experiments for such surface systems, we would like to investigate the behaviour of the density of states in the vacuum region above the adatom. In this section, we concentrate on the Fe/InSb(110) system as the one more relevant to the research topics featured in [101].

From the theory of the scanning tunneling microscope, as brought forward by Tersoff and Hamann [102], it follows that the tunneling current  $I$  between the tip and the surface is proportional to the density of states at the position  $\vec{r}_0$  of the STM tip apex taken at the Fermi energy  $E_F$  (plus/minus eventual bias voltage offset).

$$I \sim \sum_{\nu} |\psi_{\nu}(\vec{r}_0)|^2 \delta(E_{\nu} - E_F) \quad (5.1)$$

While more sophisticated models for tunneling through a surface adatom exist [125], even the relatively simple Tersoff-Hamann model warrants a closer look at the vacuum states behaviour.

The density of states in the vacuum region above the Fe adatom at various distances from the surface is shown in Fig. 5.16. To account for the tip apex we integrate the density of states around the Fermi level in a (cubic) volume with a side length of  $\sim 3 \text{ \AA}$ , which is intended as an approximation to the volume of the tungsten tip atom (with the atomic radius  $r_W \sim 1.45 \text{ \AA}$ ). The density of states is calculated in the energy region from  $-0.15 \text{ eV}$  to  $+0.3 \text{ eV}$ , to account for typical bias voltage values. The calculations were performed at four different distances (given relative to the top Sb layer position) up to  $6 \text{ \AA}$  above the surface, which would more or less correspond to the typical surface-tip distance during a topography measurement.

Quite expectedly, the density of states decreases quickly with distance, dropping to  $1/10$  of the initial value just  $2 \text{ \AA}$  above the surface. More interestingly, the relative contribution of the different spin channels changes rather significantly over the distance range. Directly above the surface the spin-down channel dominates the density of states at the Fermi level. The dominance however is lost already  $2 \text{ \AA}$  above the surface, with the spin-up channel providing higher contributions at larger distances, with an even

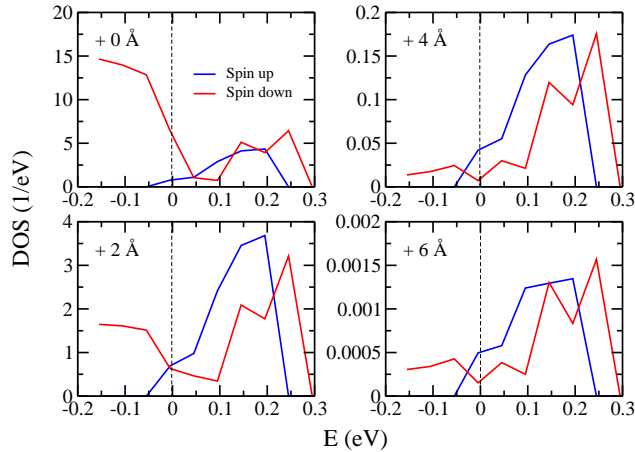


FIGURE 5.16: Vacuum density of states at various distances above the surface for the Fe adatom system, for both spin channels. The distance is given with respect to the vertical position of the outmost Sb layer.

more pronounced effect at energies above the Fermi level.

At last, and as an additional point as to why the inclusion of the vacuum density of states in a thorough discussion of a surface system is important, we briefly return to the total density of states treated at the beginning of this chapter. The corresponding plot is shown in Fig. 5.17. Through an analysis of the local DOS contributions from the different surface adatoms, the origin of the feature directly above the Fermi level, in particular in the spin-up channel, could not be clarified. Comparison of the previously calculated vacuum states with the total density elucidate the nature of these unoccupied states: they are situated in the vacuum region directly above the adatom and thus can never be accounted for by simply investigating the local atomic density of states in the surface atoms.

With this, we conclude our discussion.

## 5.6 Conclusions and outlook

Within this chapter, we have treated the (Fe/Co/Ni) adatom on InSb(110) systems by the means of density functional theory. This work was primarily motivated by the close collaboration with A. A. Khajetoorians, J. Wiebe, B. Chilian and R. Wiesendanger in a common effort to further the understanding of the physics governing the behaviour of the Fe on InSb(110) system and develop a method for measuring the magnetization of *individual* adatoms on semiconductor surfaces. That part of this work was published in [101]. The additional data presented here, not featured in the above-mentioned publication, was accumulated during the efforts to understand the Fe/InSb(110) system. Additionally, the (Co,Ni) adatom systems were treated as an extension of the project to

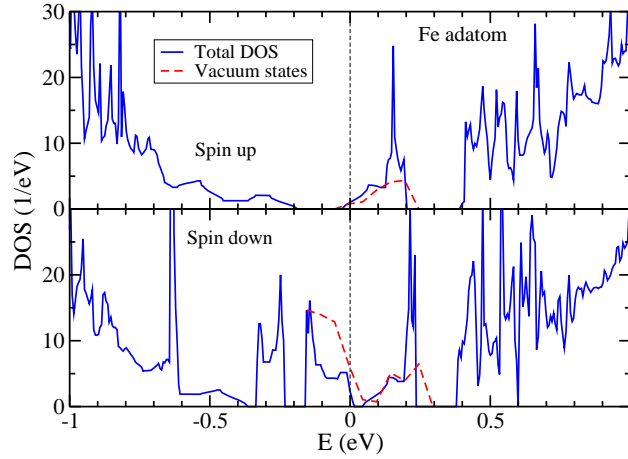


FIGURE 5.17: Comparison between the vacuum density of states shown in Fig. 5.16 and the total density of states. Through this the origin of the peak situated directly above the Fermi level becomes clear (see discussion at the beginning of this section).

further analyze the role of magnetic impurities on the InSb surface.

The Fe and Co adatom systems were found to exhibit local magnetic moments situated on the adatom d-shells, with the respective values of  $2.3 \mu_B$  and  $0.92 \mu_B$ . The Fe system moment is carried by the  $d_{xy}$  and  $d_{z^2}$  orbitals, of which the latter has a significant reach perpendicular to the surface. For the Co system, on the other hand, the local moment originates from the  $d_{xy}$  orbital only, and as such the spin polarization is more localized within the surface plane. Both systems exhibit induced magnetization of the neighbouring surface atoms. In the case of the Fe adatom, it serves to partially compensate the local Fe moment, leading to an overall unit cell moment of  $2 \mu_B$ . In the case of Co, the surrounding moments enhance the original and the total cell moment adds up to  $\sim 1 \mu_B$ . Including the spin-orbit coupling in our calculations, we find that the preferred magnetization orientation for both magnetic systems is along the  $[1\bar{1}0]$  direction, a fact of major importance for the development of the STM methodology discussed in [101]. The Ni/InSb(110) system is found to be nonmagnetic.

Further concentrating on the Fe adatom system as the one of the most importance at the time of completion of this work, we find that unoccupied states directly above the Fermi level may be attributed to the vacuum region situated directly above the Fe adatom. These states have a significant reach perpendicular to the surface and thus contribute much to the tunneling channels defining the STM functionality. Peculiarly enough, the vacuum density of states at the Fermi level switches its character from being majority-spin-channel dominated directly above the surface to being of primarily minority-spin character  $6 \text{ \AA}$  above, where the STM tip is expected to reside during the measurement. Careful analysis of the vacuum DOS behaviour should prove important in conjunction with the more sophisticated STM models [125].

The system behaviour has been shown to be governed by the well localized d-orbitals

which carry both the magnetic and contribute to the bonding properties of the setup. As such, an explicit many-body treatment of these surface systems would be an interesting next step. The influence of the spin-orbit coupling on the magnetisation direction, in conjunction with the low symmetry surface environment and the findings presented in chapter 4, should provide for an intricate interplay between electronic correlation effects and magnetic degrees of freedom, worthy of further investigation in the future.

## Chapter 6

# Summary and conclusions

Within this work, we have investigated several different realistic material and model setups, with the overarching goal to improve our understanding of the interplay between low dimensionality, spin-orbit coupling, electronic correlations and magnetism in realistic surface systems.

The Sn/Si(111) and Sn/Ge(111) systems have been known to differ in their properties despite the similarity of their constituents. From initial DFT calculations, we have constructed single-site and triangular-cluster models for both systems and investigated the influence of the substrate and local geometrical 2D-1U distortions, present in the Sn/Ge(111) system. Both systems were found to undergo a Mott transition at  $U$  values of 0.5 - 0.6 eV, with slightly higher  $U_C$  for the distorted Sn/Ge(111), which was verified by both DMFT and RISB calculations. The Sn/Si(111) system was found to exhibit a peculiar noncollinear  $120^\circ$ -like magnetic order by DFT calculations, a result corroborated by RISB. In Sn/Ge(111) no such order is present, albeit a nontrivial behaviour of nearest-neighbour spin-spin correlation functions is found close to the Mott transition.

In the second part of this work, the Hubbard bilayer model and the two-impurity Anderson model with added Dzyaloshinskii-Moriya interactions were investigated in the strongly correlated metallic regime using the RISB technique. For the Hubbard bilayer at half-filling the DM interaction is found to significantly increase in strength in presence of electronic correlations. In the hole-doped strongly correlated regime, a novel noncollinear spin-flop phase is found which is brought about by the presence of the DM interaction and through which long-range magnetic order is enabled in previously paramagnetic regions of the phase diagram.

Lastly, we have investigated the behaviour of magnetic impurities on the InSb(110) surface. The different magnetic adatom species (Fe, Co, Ni) are found to exhibit overall similar bonding properties, adsorbing in a 'trench' of the (110) surface. The Ni adatom

system is found to be paramagnetic. The other two adatom systems exhibit local magnetic moments of  $2.3 \mu_B$  and  $0.92 \mu_B$ , respectively. The spin density has a substantial reach perpendicular to the surface for the Fe/InSb(110) system while being contained to the surface in the case of the Co adatom. Analysis of the vacuum density of states above the adatom shows that the dominating spin character changes with increasing distance from the surface. This should prove important for more sophisticated STM models which explicitly include the adatom states.

The results on the Sn/Si(111) and Sn/Ge(111) surface systems were published in [63], the results on DM interaction in strongly correlated systems in [100]. Data presented in chapter 5 has been used for the preparation of and has been partially published in [101].

## 6.1 Deutsche Zusammenfassung

In dieser Arbeit wurden mehrere verschiedene realistische Materialsysteme und Modelle in Hinblick darauf untersucht, unser Verständnis des Zwischenspiels zwischen niedriger Dimension, Spin-Orbit-Kopplung, elektronischen Korrelationen und Magnetismus in realistischen Oberflächensystemen zu verbessern.

Die beiden Systeme Sn/Si(111) und Sn/Ge(111) sind schon seit geraumer Zeit dafür bekannt, sich trotz der Ähnlichkeit ihrer Konstituenten in ihren physikalischen Eigenschaften zu unterscheiden. Wir haben, ausgehend von DFT-Rechnungen, Einzel-Gitterplatz und Dreieckscluster-Modelle für beide Systeme konstruiert und konnten den Einfluss des Substrats sowie der im Sn/Ge(111) auftretenden 2D-1U Versetzung untersuchen. Beide Systeme erfahren einen Mott-Übergang bei Korrelationsstärken  $U$  von etwa 0.5 - 0.6 eV, wobei der kritische Wert  $U_C$  für die versetzte Sn/Ge(111)-Struktur etwas höher liegt. Dies wurde sowohl mit Hilfe von DMFT als auch mit Hilfe von RISB verifiziert. DFT-Rechnungen ergeben für das Sn/Si(111) System eine nicht-kollineare  $120^\circ$  magnetische Ordnung als Grundzustand, was von RISB bestätigt wurde. In dem Sn/Ge(111)-System existiert diese Ordnung nicht, dafür findet man in der Nähe des Mott-Übergangs ein nichttriviales Verhalten der Spin-Spin Korrelationsfunktionen zwischen den benachbarten Gitterplätzen.

Im zweiten Abschnitt dieser Arbeit wurden sowohl das Hubbard-Bilayer Modell als auch das Two-Impurity Anderson Modell mit zusätzlicher Dzyaloshinskii-Moriya Wechselwirkung mit Hilfe von RISB im stark korrelierten metallischen Bereich untersucht. Für das Hubbard-Modell bei halber Füllung findet man eine signifikante Verstärkung der DM-Wechselwirkung durch elektronische Korrelationen. Im Doping-Bereich unterhalb von halber Füllung entsteht durch die DM-Wechselwirkung und starke Korrelationen eine neue nicht-kollineare Phase (Spin-Flop-Phase). Dadurch wird eine langreichweitige magnetische Ordnung in Bereichen des Phasendiagramms möglich die zuvor paramagnetisch waren.

Schließlich wurde im letzten Abschnitt der Arbeit das Verhalten magnetischer Adatome auf der InSb(110)-Oberfläche untersucht. Die verschiedenen Atome (Fe, Co, Ni) haben ein ähnliches Bindungsverhalten und werden in einem der auf der (110)-Oberfläche auftretenden 'Gräben' adsorbiert. Das Ni-Adatom auf dieser Oberfläche erweist sich als paramagnetisch. Die anderen beiden Systeme zeigen lokale magnetische Momente von  $2.3\mu_B$  (Fe) und  $0.92\mu_B$  (Ni). Das Fe/InSb(110) besitzt eine beträchtliche räumliche Ausdehnung der Spindichte senkrecht zu der Oberfläche, während das magnetische Moment im Falle des Co-Adatoms auf die Oberfläche beschränkt bleibt. Die Analyse der Vakuum-Zustandsdichte oberhalb des Adatoms zeigt, dass sich der dominante Spinanteil mit der wachsenden Entfernung zur Oberfläche ändert. Dieses Verhalten sollte eine

wichtige Rolle im Rahmen komplexerer STM-Modelle spielen, bei denen die Adatom-Zustände explizit berücksichtigt werden.

Die Ergebnisse der Untersuchung der Sn/Si(111) und Sn/Ge(111) Oberflächensysteme wurden in [63] veröffentlicht, die Ergebnisse aus dem Kapitel über die DM-Wechselwirkung in [100]. Die in Kapitel 5 gezeigten Resultate wurden im Rahmen der Vorbereitungen für [101] produziert und anschliessend zum Teil darin veröffentlicht.

# Bibliography

- [1] T. Hickel, B. Grabowski, F. Körmann, and J. Neugebauer, *Journal of Physics: Condensed Matter* **24**, 053202 (2012)
- [2] S. Mandal, M. Gross, D. Raabe, and F. Vasnik, *Phys. Rev. Lett.* **108**, 098301 (2012)
- [3] A. A. Khajetoorians, J. Wiebe, B. Chilian, and R. Wiesendanger, *Science* **332**, 1062 (2011)
- [4] P. Hohenberg and W. Kohn, *Phys. Rev.* **136** (1964)
- [5] W. Kohn and L. J. Sham, *Phys. Rev.* **140**, A1133 (1965)
- [6] D. M. Ceperley and B. J. Alder, *Phys. Rev. Lett.* **45**, 566 (1980)
- [7] J. P. Perdew, K. Burke, and M. Ernzerhof, *Phys. Rev. Lett.* **77**, 3865 (1996)
- [8] F. Lechermann, A. Georges, A. Poteryaev, S. Biermann, M. Posternak, A. Yamasaki, and O. Andersen, *Phys. Rev. B* **74**, 125120 (2006)
- [9] N. Marzari and D. Vanderbilt, *Phys. Rev. B* **56**, 12847 (1997)
- [10] I. Souza, N. Marzari, and D. Vanderbilt, *Phys. Rev. B* **65**, 035109 (2001)
- [11] R. Martin, “Electronic structure: Basic theory and practical methods,” (University Press, Cambridge, 2004)
- [12] “The lda+dmft approach to strongly correlated materials,” (Forschungszentrum Juelich, Institute for Advanced Simulations, 2011)
- [13] F. Lechermann, A. Georges, G. Kotliar, and O. Parcollet, *Phys. Rev. B* **76**, 155102 (2007)
- [14] W. Metzner and D. Vollhardt, *Phys. Rev. E* **62**, 324 (1989)
- [15] J. E. Hirsch and R. M. Fye, *Phys. Rev. Lett.* **56**, 2521 (1986)

- 
- [16] A. N. Rubtsov, V. V. Savkin, and A. I. Lichtenstein, *Phys. Rev. B* **72**, 035122 (2005)
- [17] P. Werner, A. Comanac, L. de Medici, M. Troyer, and A. J. Millis, *Phys. Rev. Lett.* **97**, 076405 (2006)
- [18] P. Werner and A. J. Millis, *Phys. Rev. B* **74**, 155107 (2006)
- [19] E. Gull, P. Werner, O. Parcollet, and M. Troyer, *Europhys. Lett.* **82**, 57003 (2008)
- [20] J. E. Gubernatis, M. Jarrell, R. N. Silver, and D. S. Sivia, *Phys. Rev. B* **44**, 6011 (1991)
- [21] M. Jarrell and J. E. Gubernatis, *Phys. Rep.* **269**, 134 (1996)
- [22] A. Georges, G. Kotliar, W. Krauth, and M. J. Rozenberg, *Rev. Mod. Phys.* **68**, 13 (1996)
- [23] A. Georges, *Lectures on the Physics of Highly Correlated Electron Systems VIII*, AIP Conference Proceedings **715** (2004)
- [24] R. E. Schlier and H. E. Farnsworth, *J. Chem. Phys.* **30**, 917 (1959)
- [25] J. M. Carpinelli, H. H. Weitering, E. W. Plummer, and R. Stumpf, *Nature* **381**, 398 (1996)
- [26] H. H. Weitering, X. Shi, P. D. Johnson, J. Chen, N. J. DiNardo, and K. Kempa, *Phys. Rev. Lett.* **78**, 1331 (1997)
- [27] S. Modesti, L. Petaccia, G. Ceballos, I. Vobornik, G. Panaccione, G. Rossi, L. Ottaviano, R. Larciprete, S. Lizzit, and A. Goldoni, *Phys. Rev. Lett.* **98**, 126401 (2007)
- [28] G. Profeta and E. Tosatti, *Phys. Rev. Lett.* **98**, 086401 (2007)
- [29] A. Charrier, R. Pérez, F. Thibaudau, J.-M. Debever, J. Ortega, F. Flores, and J.-M. Themlin, *Phys. Rev. B* **64**, 115407 (2001)
- [30] H. Morikawa, I. Matsuda, and S. Hasegawa, *Phys. Rev. B* **65**, 201308 (2002)
- [31] F. Flores, J. Ortega, R. Pérez, A. Charrier, F. Thibaudau, J.-M. Debever, and J.-M. Themlin, *Prog. Surf. Sci* **67**, 299 (2001)
- [32] G. Profeta, A. Continenza, L. Ottaviano, W. Mannstadt, and A. J. Freeman, *Phys. Rev. B* **62**, 1556 (2000)
- [33] J. Avila, A. Mascaraque, E. G. Michel, M. C. Asensio, G. L. Lay, J. Ortega, R. Pérez, and F. Flores, *Phys. Rev. Lett.* **82**, 442 (1999)

- 
- [34] O. Pulci, M. Marsili, P. Gori, M. Palumbo, A. Cricenti, F. Bechstedt, and R. del Sole, *Appl. Phys. A* **85**, 361 (2006)
- [35] R. Cortés, A. Tejada, J. Lobo, C. Didiot, B. Kierren, D. Malterre, G. Michel, and A. Mascaraque, *Phys. Rev. Lett.* **96**, 126103 (2006)
- [36] S. Colonna, F. Ronci, A. Cricenti, and G. L. Lay, *Phys. Rev. Lett.* **101**, 186102 (2008)
- [37] H. Morikawa, S. Jeong, and H. W. Yeom, *Phys. Rev. B* **78**, 245307 (2008)
- [38] S. D. Gironcoli, S. Scandolo, G. Ballabio, G. Santoro, and E. Tosatti, *Surf. Sci.* **454**, 172 (2000)
- [39] J. P. Perdew and K. Schmidt, “Density functional theory and its application to materials,” (AIP, Melville, NY, 2001)
- [40] V. I. Anisimov, A. I. Poteryaev, M. A. Korotin, A. O. Anokhin, and G. Kotliar, *J. Phys.: Condens. Matter* **9**, 7359 (1997)
- [41] A. I. Lichtenstein and M. I. Katsnelson, *Phys. Rev. B* **57**, 6884 (1998)
- [42] J. Bünemann, F. Gebhard, T. Ohm, R. Umstätter, S. Weiser, W. Weber, R. Claessen, D. Ehm, A. Harasawa, A. Kakizaki, A. Kimura, G. Nicolay, S. Shin, and V. N. Strovov, *Europhys. Lett.* **61**, 667 (2003)
- [43] X. Y. Deng, X. Dai, and Z. Fang, *Europhys. Lett.* **83**, 37008 (2008)
- [44] F. Lechermann, *Phys. Rev. Lett.* **102**, 046403 (2009)
- [45] T. Li, P. Wölfle, and P. J. Hirschfeld, *Phys. Rev. B* **40**, 6817 (1989)
- [46] J. Bünemann, W. Weber, and F. Gebhard, *Phys. Rev. B* **57**, 6896 (1998)
- [47] M. Fabrizio, unpublished(2007)
- [48] B. Meyer, C. Elsässer, F. Lechermann, and M. Fähnle, *FORTRAN 90 Program for Mixed-Basis-Pseudopotential Calculations for Crystals*, Max-Planck-Institut für Metallforschung, Stuttgart (unpublished)
- [49] S. G. Louie, K. M. Ho, and M. L. Cohen, *Phys. Rev. B* **19**, 1774 (1979)
- [50] D. Vanderbilt, *Phys. Rev. B* **32**, 8412 (1985)
- [51] P. E. Blöchl, *Phys. Rev. B* **50**, 17953 (1994)
- [52] G. Kresse and J. Hafner, *J. Phys.: Condens. Matter* **6**, 8245 (1994)

- 
- [53] G. B. Bachelet and N. E. Christensen, Phys. Rev. B **31**, 879 (1985)
- [54] D. Glötzel, B. Segall, and O. K. Andersen, Solid State Comm. **36**, 403 (1980)
- [55] T. Yoshikawa and M. Ogata, Phys. Rev. B **79**, 144429 (2009)
- [56] T. Zhang and *et al.*, Nat. Phys. **6**, 104 (2010)
- [57] A. Mielke, J. Phys. A **24** (1991)
- [58] H. Tasaki, Phys. Rev. Lett. **69**, 1608 (1992)
- [59] R. I. G. Uhrberg, H. M. Zhang, T. Balasubramanian, S. T. Jemander, N. Lin, and G. V. Hansson, Phys. Rev. B **62**, 8082 (2000)
- [60] A. Lichtenstein, M. Katsnelson, and G. Kotliar, “Electron correlations and materials properties 2,” (Kluwer Academic, New York, 2003)
- [61] G. Biroli, O. Parcollet, and G. Kotliar, Phys. Rev. B **69**, 205108 (2004)
- [62] T. Maier, M. Jarrell, T. Pruschke, and M. H. Hettler, Rev. Mod. Phys. **77**, 1027 (2005)
- [63] S. Schuwalow, D. Grieger, and F. Lechermann, Phys. Rev. B **82**, 035116 (2010)
- [64] G. Santoro, S. Scandolo, and E. Tosatti, Phys. Rev. B **59**, 1891 (1999)
- [65] G. Li, M. Laubach, A. Fleszar, and W. Hanke, Phys. Rev. B **83**, 041104 (2011)
- [66] C. Ederer and N. A. Spaldin, Phys. Rev. B **71**, 060401(R) (2005)
- [67] D. Khomskii, Physics **2**, 20 (2009)
- [68] M. Bode, M. Heide, K. von Bergmann, P. Ferriani, S. Heinze, G. Bihlmayer, A. Kubetzka, O. Pietzsch, S. Blügel, and R. Wiesendanger, Nature **447**, 190 (2007)
- [69] J.-J. Zhu, D.-X. Yao, S.-C. Zhang, and K. Chang, Phys. Rev. Lett. **106**, 097201 (2011)
- [70] I. Dzyaloshinskii, J. Phys. Chem. Solids **4**, 241 (1958)
- [71] T. Moriya, Phys. Rev. **120**, 91 (1960)
- [72] L. Néel and R. Pauthenet, C. R. Acad. Sci., Paris **234**, 2172 (1952)
- [73] P. W. Anderson, Phys. Rev. **115**, 2 (1959)
- [74] J. Jensen, Phys. Rev. B **84**, 104405 (2011)

- 
- [75] S. Miyahara, J.-B. Fouet, S. R. Manmana, R. M. Noack, H. Mayaffre, I. Sheikin, C. Berthier, and F. Mila, *Phys. Rev. B* **75**, 184402 (2007)
- [76] T. Thio, T. R. Thurston, N. W. Preyer, P. J. Picone, M. A. Kastner, H. P. Jenssen, D. R. Gabbe, C. Y. Chen, R. J. Birgeneau, and A. Aharony, *Phys. Rev. B* **38**, 905(R) (1988)
- [77] D. Coffey, T. M. Rice, and F. C. Zhang, *Phys. Rev. B* **44**, 10112 (1991)
- [78] V. Juricic, M. B. S. Neto, and C. M. Smith, *Phys. Rev. Lett.* **96**, 077004 (2006)
- [79] K. Hirota, Y. Moritomo, H. Fujioka, M. Kubota, H. Yoshizawa, and Y. Endoh, *J. Phys. Soc. Jpn.* **67**, 3380 (1998)
- [80] J. F. Mitchell, D. N. Argyriou, A. Berger, K. E. Gray, R. Osborn, and U. Welp, *J. Phys. Chem B* **105**, 10731 (2001)
- [81] I. V. Solovyev, A. I. Lichtenstein, and K. Terakura, *Phys. Rev. Lett.* **80**, 5758 (1998)
- [82] F. Kagawa, Y. Kurosaki, K. Miyagawa, and K. Kanoda, *Phys. Rev. B* **78**, 184402 (2008)
- [83] W. Ziegler, P. Dieterich, A. Muramatsu, and W. Hanke, *Phys. Rev. B* **53**, 1231 (1996)
- [84] G. Moeller, V. Dobrosavljević, and A. E. Ruckenstein, *Phys. Rev. B* **59**, 6846 (1999)
- [85] A. Fuhrmann, D. Heilmann, and H. Monien, *Phys. Rev. B* **73**, 245118 (2006)
- [86] S. S. Kancharla and S. Okamoto, *Phys. Rev. B* **75**, 193103 (2007)
- [87] K. Bouadim, G. G. Batrouni, F. Hébert, and R. T. Scalettar, *Phys. Rev. B* **77**, 144527 (2008)
- [88] H. Hafermann, M. I. Katsnelson, and A. I. Lichtenstein, *Europhys. Lett.* **85**, 37006 (2009)
- [89] C. Jayaprakash, H. R. Krishna-murthy, and J. Wilkins, *J. Appl. Phys.* **53**, 2142 (1982)
- [90] R. M. Fye, J. E. Hirsch, and D. J. Scalapino, *Phys. Rev. B* **35**, 4901 (1987)
- [91] R. O. Jones and O. Gunnarsson, *Rev. Mod. Phys.* **61**, 689 (1989)
- [92] R. M. Fye and J. E. Hirsch, *Phys. Rev. B* **40**, 4780 (1989)

- 
- [93] A. Schiller and V. Zevin, *Ann. Physik* **5**, 363 (1996)
- [94] S. Nishimoto, T. Pruschke, and R. M. Noack, *J. Phys.: Condens. Matter* **18**, 981 (2006)
- [95] M. Ferrero, P. S. Cornaglia, L. D. Leo, O. Parcollet, G. Kotliar, and A. Georges, *Europhys. Lett.* **85**, 57009 (2009)
- [96] L. Zhou, J. Wiebe, S. Lounis, E. Vedmedenko, F. Meier, S. Blügel, P. H. Dederichs, and R. Wiesendanger, *Nature Physics* **6**, 187 (2010)
- [97] M. Behrmann, C. Piefke, and F. Lechermann, arXiv:1203.3148(2012)
- [98] J. R. Schrieffer and P. A. Wolff, *Phys. Rev.* **149**, 491 (1966)
- [99] C. Niedermayer, C. Bernhard, T. Blasius, A. Golnik, A. Moodenbaugh, and J. I. Budnick, *Phys. Rev. Lett.* **80**, 3843 (1998)
- [100] S. Schuwalow, C. Piefke, and F. Lechermann, *Phys. Rev. B* **85**, 205132 (2012)
- [101] A. A. Khajetoorians, B. Chilian, J. Wiebe, S. Schuwalow, F. Lechermann, and R. Wiesendanger, *Nature* **467**, 1084 (2010)
- [102] J. Tersoff and D. R. Hamann, *Phys. Rev. B* **31**, 805 (1984)
- [103] J. M. Tang, J. Levy, and M. E. Flatté, *Phys. Rev. Lett.* **97**, 106803 (2006)
- [104] R. Hanson and D. D. Awschalom, *Nature* **453**, 1043 (2008)
- [105] C. L. Gall, L. Besombes, H. Boukari, R. Kolodka, J. Cobert, and H. Mariette, *Phys. Rev. Lett.* **102**, 127402 (2009)
- [106] C. B. Duke, *Applied Surface Science* **65**, 543 (1993)
- [107] A. Höglund, C. W. M. Castleton, M. Göthelid, B. Johansson, and S. Mirbt, *Phys. Rev. B* **74**, 075332 (2006)
- [108] M. C. Qian, M. Göthelid, B. Johansson, and S. Mirbt, *Phys. Rev. B* **66**, 155326 (2002)
- [109] J. Klijn, L. Sacharow, C. Meyer, S. Blügel, M. Morgenstern, and R. Wiesendanger, *Phys. Rev. B* **68**, 205327 (2003)
- [110] L. Sacharow, M. Morgenstern, G. Bihlmayer, and S. Blügel, *Phys. Rev. B* **69**, 085317 (2004)
- [111] R. Masutomi, M. Hio, T. Mochizuki, and T. Okamoto, *Appl. Phys. Lett.* **90**, 202104 (2007)

- 
- [112] Y. Tsuji, T. Mochizuki, and T. Okamoto, *Appl. Phys. Lett.* **87**, 062103 (2005)
- [113] Y. Tsuji, T. Mochizuki, and T. Okamoto, *Physica E* **34**, 156 (2006)
- [114] T. Matsui, C. Meyer, L. Sacharow, J. Wiebe, and R. Wiesendanger, *Phys. Rev. B* **75**, 165405 (2007)
- [115] T. O. Strandberg, C. M. Canali, and A. H. MacDonald, *Phys. Rev. B* **80**, 024425 (2009)
- [116] K. Shiraishi, *J. Phys. Soc. Jpn.* **59**, 3455 (1990)
- [117] G. Kresse and D. Joubert, *Phys. Rev. B* **59**, 1758 (1999)
- [118] C. Mailhot, C. B. Duke, and D. J. Chadi, *Surf. Sci.* **149**, 366 (1985)
- [119] C. Mailhot, C. B. Duke, and D. J. Chadi, *Phys. Rev. Lett.* **53**, 2114 (1984)
- [120] A. Kahn, *Surf. Sci. Rep.* **3**, 193 (1983)
- [121] F. Bechstedt and R. Enderlein, "Semiconductor surfaces and interfaces," (Akademie Verlag, Berlin, 1988)
- [122] D. J. Chadi, *Phys. Rev. B* **19**, 2074 (1979)
- [123] A. C. Ferraz and G. P. Srivastava, *Surf. Sci.* **182**, 161 (1987)
- [124] B. Engels, P. Richard, K. Schroeder, S. Blügel, P. Ebert, and K. Urban, *Phys. Rev. B* **58**, 7799 (1998)
- [125] N. Lorente and J.-P. Gauyacq, *Phys. Rev. Lett.* **103**, 176601 (2009)

# *Acknowledgements*

I would like to sincerely thank...

- my supervisor JProf. Dr. Frank Lechermann for making this possible, for his support and patience in questions both scientific and not, but also for the gentle pushes in the right direction in times when things were going slow.
- Prof. Alexander Lichtenstein for his help and wise advice in all possible things.
- people from my group: Lewin Boehnke for the interesting and thought-provoking discussions on both many-body physics and everyday matters, Christoph Piefke for his unwavering support with the RISB code and for always striving to maintain equilibrium both within himself and around him, Daniel Grieger for the DFT-related discussions, help with numerical and computational matters and for periodically accompanying me to various food-related places around the campus, Malte Behrmann for being an overall nice guy and always speaking his mind and Oleg Peil for his humor and scientific support on several important occasions.
- Daniel Grieger again for proofreading this whole thing several times.
- Tim Wehling for providing me with some insights mostly related to the VASP code.
- Alexander A. Khajetoorians, Jens Wiebe and Bruno Chilian for the very fun and interesting collaboration which allowed me to gain some insight into the STM method.
- Lars Ehrlich for always providing an unorthodox view of things and generally being the best friend ever.
- Swantje Heers for being an inspiration.
- and finally my parents and my brother for being there for me. This work would not have been possible without your support.